



January 2021

Estimating Analysis Temperature And Humidity Biases Due To Assimilation Of Aerosol & Cloud Contaminated Hyperspectral Infrared Radiances

Jared Wayne Marquis

Follow this and additional works at: <https://commons.und.edu/theses>

Recommended Citation

Marquis, Jared Wayne, "Estimating Analysis Temperature And Humidity Biases Due To Assimilation Of Aerosol & Cloud Contaminated Hyperspectral Infrared Radiances" (2021). *Theses and Dissertations*. 4087.

<https://commons.und.edu/theses/4087>

This Dissertation is brought to you for free and open access by the Theses, Dissertations, and Senior Projects at UND Scholarly Commons. It has been accepted for inclusion in Theses and Dissertations by an authorized administrator of UND Scholarly Commons. For more information, please contact und.common@library.und.edu.

ESTIMATING ANALYSIS TEMPERATURE AND HUMIDITY
BIASES DUE TO ASSIMILATION OF AEROSOL & CLOUD
CONTAMINATED HYPERSPECTRAL INFRARED RADIANCES

by

Jared W. Marquis

Bachelor of Science, University of Louisiana at Monroe, 2014

Master of Science, University of North Dakota, 2016

A Dissertation

Submitted to the Graduate Faculty

of the

University of North Dakota

in partial fulfillment of the requirements

for the degree of

Doctor of Philosophy

Grand Forks, North Dakota

August

2021

Copyright 2021 Jared W. Marquis

Name: Jared Marquis
Degree: Doctor of Philosophy


This document, submitted in partial fulfillment of the requirements for the degree from the University of North Dakota, has been read by the Faculty Advisory Committee under whom the work has been done and is hereby approved.


DocuSigned by:


2787AED1C19A41B...
Jianglong Zhang

DocuSigned by:

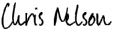
776518977B79460...
Aaron Kennedy

DocuSigned by:

718912E93F428D2...
James Campbell

DocuSigned by:

49620E78897C465...
Anne Garnier

DocuSigned by:

3F7DA3282EB4406...
Taufique Mahmood

This document is being submitted by the appointed advisory committee as having met all the requirements of the School of Graduate Studies at the University of North Dakota and is hereby approved.

DocuSigned by:

2E0AF088C733403...
Chris Nelson
Dean of the School of Graduate Studies
7/1/2021
Date

PERMISSION

Title Estimating Analysis Temperature and Humidity Biases
 due to Assimilation of Aerosol & Cloud Contaminated
 Hyperspectral Infrared Radiances

Department Atmospheric Sciences

Degree Doctor of Philosophy

In presenting this dissertation in partial fulfillment of the requirements for a graduate degree from the University of North Dakota, I agree that the library of this University shall make it freely available for inspection. I further agree that permission for extensive copying for scholarly purposes may be granted by the professor who supervised my thesis work or, in his absence, by the Chairperson of the department or the dean of the School of Graduate Studies. It is understood that any copying or publication or other use of this thesis or part thereof for financial gain shall not be allowed without my written permission. It is also understood that due recognition shall be given to me and to the University of North Dakota in any scholarly use which may be made of any material in my thesis.

Jared Marquis

Jared W. Marquis
Friday 2nd July, 2021

TABLE OF CONTENTS

LIST OF FIGURES	viii
LIST OF TABLES	xiii
ACKNOWLEDGMENTS	xiv
ABSTRACT	xv
CHAPTER	
1 INTRODUCTION	1
1.1 Radiance Assimilation	10
1.2 Cloud & Aerosol Impacts in Other Satellite Products	11
1.3 Residual Cloud and Aerosol	12
2 AEROSOL INDUCED ANALYSIS BIAS	17
2.1 Introduction	17
2.1.1 Rationale	17
2.1.2 Background	17
2.2 Datasets & Models	20
2.2.1 RTTOV	20
2.2.2 1DVar System	22
2.2.3 Error Covariances	25
2.2.4 Tenerife, Canary Islands, Spain	26
2.2.5 Meteorological Profiles	28
2.2.6 Aerosol Observations from AERONET	29
2.2.7 Aerosol Observations from MPLNET	30
2.2.8 OPAC	30
2.3 Methodology	31
2.3.1 Meteorological Profiles	31
2.3.2 Aerosol Extinction Profiles	33
2.3.3 Aerosol Number Profiles	37
2.3.4 Synthetic Hyperspectral Observations	38
2.3.5 Determining Analysis Bias	39

2.3.6	MERRA-2 Experiment	39
2.4	Results	40
2.4.1	Dust Induced Radiance Biases	40
2.4.2	Impact on Analyzed Temperature	41
2.4.3	Impact on Analyzed Dewpoint Temperature	43
2.4.4	Bias at Other Aerosol Loadings	44
2.4.5	Impact With Imperfect Background Atmosphere	48
2.5	Discussion	49
3	CLOUD INDUCED ANALYSIS BIAS	51
3.1	Introduction	51
3.1.1	Rationale	51
3.1.2	Background	51
3.2	Datasets & Models	55
3.2.1	RTTOV	55
3.2.2	1DVAR & Error Variances	55
3.2.3	Meteorological Profile	57
3.2.4	Simulated Cirrus Clouds	57
3.2.5	8-Column Aggregate Ice	59
3.3	Methodology	60
3.3.1	Ice Optical Properties	60
3.3.2	Synthetic Hyperspectral Observations	71
3.3.3	Radiance Impacts	73
3.3.4	Determining Radiance and Analysis Bias	73
3.4	Results	74
3.4.1	Cirrus Induced Radiance Biases	74
3.4.2	Jacobian Impacts	76
3.4.3	Cirrus Impact on Analyzed Temperature & Moisture	79
3.5	Discussion	83
4	AEROSOL INFRARED RADIATIVE CLOSURE	84
4.1	Introduction	84
4.1.1	Rationale	84
4.1.2	Background	85
4.1.3	08 August 2013	87
4.2	Datasets & Models	91
4.2.1	Fu-Liou-Gu Radiative Transfer Model	91
4.2.2	GEOS-5 Meteorological & Aerosol Profiles	93
4.2.3	Surface Reflectance	93
4.2.4	Broadband Radiometers	95
4.2.5	DIAL-HSRL	95
4.2.6	PINeph	96
4.2.7	CPL	97

4.2.8	Aerosol Models	98
4.3	Methodology	99
4.3.1	Verifying Fu-Liou-Gu	99
4.3.2	Determining Study Window	102
4.3.3	Interpolation	102
4.3.4	Aerosol Extinction Profiles	104
4.3.5	Comparing PiNeph Measurements	106
4.4	Results	108
4.4.1	Optical Property Comparison	108
4.4.2	Aerosol Extinction Profiles	111
4.4.3	Flux Comparison	112
4.4.4	Heating Rate Comparison	115
4.5	Discussion	117
5	SUMMARY AND CONCLUSIONS	119
	APPENDIX A LIST OF ABBREVIATIONS	124
	REFERENCES	128

LIST OF FIGURES

Figure	Page	
1	Temperature Jacobian for at three different infrared wavelengths in a tropical standard atmosphere from McClatchey et al. (1972). The temperature Jacobians show the sensitivity of the top-of-atmosphere measured radiance to the atmospheric temperature at each wavelength.	5
2	Temperature Jacobian for every tenth CrIS wavelength band at normal spectral resolution. Thus, 130 Jacobians are shown of the 1305 bands. . .	7
3	The 24 hour forecast error norm ($J\ kg^{-1}$) for NAVGEM for 30 days of radiance assimilation ending on 1 Jun 2017 with current HIS instruments highlighted in red. Total number of assimilated observations for each sensor reported on the right. Adapted from Marquis et al. (2021)	8
4	Histograms of aerosol optical depth of assimilated aerosol-contaminated HIS radiances from (a) CrIS channel 713 and (b) IASI channel 379 from July 2018. Adapted from Marquis et al. (2021).	13
5	Histograms of cirrus cloud contamination in assimilated observations from (a & b) AIRS band 122 ($13.85\ \mu m$) and (c & d) AIRS band 136 ($13.49\ \mu m$) as a function of visible cloud optical depth (a & c) and cloud top temperature (b & d).	15
6	Flowchart indicating the process used in the 1DVar system to determine the analysis atmosphere. Adapted from Havemann (2020)	23
7	Location of observation sites used in Tenerife, Canary Islands, Spain with the Sahara Desert shaded. Created with QGIS V3.16.6.	27
8	Locations of all sites with at least one radiosonde launch in 2020 or 2021. Created using Python v3.8.5 and Cartopy v0.18.0.	28

9	(A) Mean temperature (red) and dew point (blue) profiles from merged radiosonde-standard atmosphere (solid) and MERRA-2 reanalysis bilinearly interpolated to the radiosonde launch location (dashed). Also indicated is (B) all obs profiles and (C) corresponding MERRA-2 profiles passing quality checks.	32
10	(a) Mean 550nm aerosol extinction profile with ± 1 standard deviation, and distribution of cases by (b) 550nm AOD, (c) fine mode fraction, and (d) 550nm-extinction-to-523nm-backscatter in steradians. Adapted from Marquis et al. (2021).	37
11	Mean brightness temperature bias as a function of wavelength for the 97 dust cases. Adapted from Marquis et al. (2021).	40
12	Vertical profile of the mean (± 1 standard deviation indicated by horizontal bounds) of the analyzed temperature bias for the 97 dust cases. Adapted from Marquis et al. (2021).	42
13	Vertical profile of the mean (± 1 standard deviation indicated by horizontal bounds) of the analyzed dew point temperature bias for the 97 dust cases. Adapted from Marquis et al. (2021).	44
14	Scatter plot of the maximum brightness temperature bias as a function of column AOD for each of the 97 cases along with the best fit linear regression line. Adapted from Marquis et al. (2021).	45
15	Scatter plot of the maximum tropospheric temperature bias as a function of AOD and brightness temperature bias for each of the 97 dust cases. Adapted from Marquis et al. (2021).	46
16	Scatter plot of the maximum tropospheric dew point temperature bias as a function of AOD and brightness temperature bias for each of the 97 dust cases. Adapted from Marquis et al. (2021).	47
17	Temperature and dew point error after assimilation with aerosol optical properties included (red) and not included (green) compared to the background atmosphere from MERRA-2 (black) for the 97 dust cases. Adapted from Marquis et al. (2021).	49
18	Frequency of optically thin cirrus clouds (visible optical depth below 0.30) from CALIOP based on 2006 - 2018.	53

19	Temperature and humidity profiles for the McClatchey et al. (1972) tropical standard atmosphere interpolated to the study grid. Indicated by horizontal dashed lines are the first altitude below 233 K (at 236 hPa) and the tropopause (at 97 hPa) between which cirrus clouds are simulated.	58
20	Impression of the 8-column aggregated ice crystals. Adapted from Yang et al. (2013) Fig. 3 and Platnick et al. (2017) Fig. 3.	59
21	Relative percentage of particles of different sizes for effective radii of (dotted) 5.0, (solid) 10.0, and (dashed) 20 μm	61
22	Normalized root mean squared error (RMSE) of the phase function by number of Legendre expansion coefficients.	66
23	Absorption efficiency (given by 1-SSA) for MODIS band (a) 2.13 μm and (b) 3.7 μm as a function of effective radius. Also shown in (c-d) is the absorption efficiency derived here for the same bands. The curve in (c-d) corresponds to the (blue) <i>Aggregated Columns</i> curve in (a-b). (a-b) is adapted from Platnick et al. (2017).	68
24	Phase function for MODIS band (a) 0.87 μm and (b) 1.63 μm for (red) 10 μm and (blue) 40 μm effective radii. Also shown in (c-d) is the phase function derived here for the same bands and effective radii. The curves in (c-d) corresponds to the (dashed) <i>Collection 6</i> curve in (a-b). (a-b) is adapted from Platnick et al. (2017).	69
25	(A) Heymsfield et al. (2014) ice crystal effective radius versus temperature parameterization and (B) the ice crystal effective radius as a function of pressure altitude for the standard tropical atmosphere used here.	72
26	(A) CrIS clear-sky brightness temperature curve for the standard tropical atmosphere and (B) brightness temperature bias for a cloud with cloud top temperature of 210 K and (dotted) COD of 0.10, (dashed) COD of 0.30, and (dot-dashed) COD of 1.00. Also, (C) the brightness temperature bias of a cloud of COD 0.30 with (dotted) cloud top temperature of 228 K, (dashed) 210 K, and (dot-dashed) 195 K.	74
27	(A) Absorption efficiency, (B) scattering efficiency, and (C) extinction efficiency for the CrIS wavelengths for effective radii of (dot-dashed) 10 μm , (dashed) 40 μm , and (dotted) 75 μm . Created using the 8CASM optical model from Yang et al. (2013).	75

28	Temperature Jacobians as a function of 532 nm cloud optical depth (A & C) for a cloud with cloud top temperature of 210 K and (B & D) as a function of cloud top temperature for an optical depth of 0.30 for CrIS bands (A-B) 745 corresponding to 8.0 μm and (C-D) 293 corresponding to 12.0 μm	77
29	Temperature Jacobians when background and analysis contain no cloud as a function of 532 nm cloud optical depth (A & C) for a cloud with cloud top temperature of 210 K and (B & D) as a function of cloud top temperature for an optical depth of 0.30 for CrIS bands (A-B) 745 corresponding to 8.0 μm and (C-D) 293 corresponding to 12.0 μm	78
30	Maximum analyzed (A) temperature and (B) dew point bias in the tropopause associated with assimilation of cloud contaminated radiances when assuming clear-sky observations as a function of cloud top temperature and optical depth. Black areas indicate that the assimilation system failed to converge to a solution when assuming clear-sky. Super-imposed in white is the contamination percentage of that cloud type as determined by collocation with lidar observations.	80
31	As in Figure 30 except for tropospheric root mean squared error.	82
32	Aircraft ground tracks for the relocation flight from Palmdale Regional Airport to Ellington Field Joint Reserve Base on 08 August 2013. (Red) ER-2 flight track and (Blue) DC-8 flight track.	88
33	CPL measured backscatter from on-board the ER-2 during the first transect of the aerosol plume with features identified.	89
34	Aircraft ground tracks and altitudes for the three transects of the dust plume on 08 August 2013. (Cyan) ER-2 flight track and (Magenta) DC-8 flight track.	90
35	Average broadband solar albedo over the northern Gulf of Mexico from CERES aboard the NASA TERRA and AQUA satellites for August 2013.	94
36	TERRA-MODIS true color image from 07 March 2009 with the Bermuda AERONET site indicated by the red point.	100
37	(Black) Measured and (red) simulated downwelling solar flux at the Bermuda AERONET site for 07 March 2009 along with (green) the percent difference between the two measurements.	101

38	(Bottom) Upward looking DIAL-HSRL and co-located (top) downward looking CPL backscatter curtains from the first transect of the dust plume in the northern Gulf of Mexico with the chosen study window indicated by vertical black lines. The altitudes of the aircraft are approximately 0.5 km for the DC-8 and 18 - 20 km for the ER-2 (see Fig. 34)	103
39	Both upward and downward pointed DIAL-HSRL extinction-to-backscatter ratio during the third transect. The averaging window for the lidar ratio within 1 km of the study window and within the aerosol layer is indicated by the black box. During this transect, the DC-8 was at an altitude of approximately 6.5 km.	105
40	(Black) PINeph measured optical properties of broadband (A) extinction efficiency, (B) single scattering albedo, and (C) asymmetry parameter compared to the (blue) OPAC and (red) Tegen and Lacis (1996) dust optical models.	109
41	Dust extinction profiles from (black) CPL, (red) GEOS-5 using the OPAC optical model, and (blue) GEOS-5 using the Tegen and Lacis (1996) optical model for the study window.	110
42	(A) Downwelling, (B) upwelling shortwave flux and (c) downwelling and (d) upwelling IR flux as a function of altitude calculated using FLG with the CPL extinction profile for (red) each of the Tegen and Lacis (1996) and (blue) OPAC dust optical models. Also shown are fluxes for the (green) GEOS-5 aerosol analyses for each of the optical models and (black) aerosol-free fluxes. The BBR flux measurements are shown at the aircraft altitude as a black star.	113
43	As in Fig. 42, but for (A) shortwave heating rate, (B) IR heating rate, and (C) total heating rate.	115

LIST OF TABLES

Table		Page
1	Spectral bands used in radiative transfer simulations by the Fu-Liou-Gu radiative transfer model.	92
2	Default 532 nm lidar ratios used in unconstrained aerosol extinction retrievals using CPL.	97
3	List of Abbreviations	124

ACKNOWLEDGMENTS

I wish to express my gratitude to my advisor, Dr. Jianglong Zhang, for his support, guidance, and patience throughout the course of my doctoral program. He has provided me with every opportunity for success and never showed anything but support for non-research tasks I took on. Because of his support, I was able to flourish as an independent researcher. I wish to thank my mentor Dr. James Campbell who always went out of his way to ensure my success and provide guidance in challenging times. I also thank the other members of my doctoral committee, Drs. Aaron Kennedy, Anne Garnier, and Taufique Mahmood for their support in improving my work.

I want to thank those in Dr. Zhang's research group at the University of North Dakota, those in Dr. Campbell's research group at the Naval Research Laboratory, Dr. Olga Kalashnikova, and the countless others who provided constructive feedback and assistance throughout the course my doctoral program. Additionally, I'd like to thank all of my friends and graduate students in the Atmospheric Science Department for making my graduate school experience memorable and turning Grand Forks into my home.

Finally, I want to express my sincere gratitude to my family and my wife who supported and encouraged me throughout my schooling for which I am forever grateful.

ABSTRACT

Observations from hyperspectral infrared sounder (HIS) instruments aboard earth-observing satellites have become a cornerstone of numerical weather prediction assimilation efforts – providing the largest decrease in forecast error of any assimilated satellite observations. The assimilation of infrared (IR) radiances is predicated on the assumption of clear-sky observations. Thus, any signal imparted upon the HIS radiances due to cloud or aerosol will likely result in unexpected and uncharacterized biases in analyzed temperature and humidity fields. Forecasts based upon these biased fields may have large inherent inaccuracies. The process of cloud and aerosol screening of passive satellite products and radiances is imperfect. Residual aerosol and cirrus clouds are found to contaminate HIS radiances assimilated from presumed clear-sky scenes at concerning rates (approximately 30% and 8% for the Naval Research Laboratory Variational Data Assimilation System, respectively). As such, the presence of an uncharacterized bias exists within model analyses.

To determine the biases a modified one-dimensional variational (1DVar) assimilation system is used for two studies: one for aerosol, one for cloud. For the aerosol study, observations of dust from the Island of Tenerife, Spain are used to create synthetic dust contaminated HIS observations. For the cloud study, a series of clouds of varying optical depth and cloud top altitude are simulated. Analysis biases greater than expected forecast uncertainties are found for both studies. Aerosol biases are smaller, likely due to lower thermal contrast with the lower atmosphere. For instance, at an average aerosol optical depth of 0.30 a peak temperature bias of 0.5 K and dew

point bias of 1.0 K is found. Meanwhile, for cloud optical depths as small as 0.1, maximum temperature and dew point biases of 3 K and 10 K are shown.

Finally, a third study in similar vein to the first two simplifies the impact of aerosols on numerical weather prediction by examining the impact of aerosol optical model on broadband radiative properties. Observations above and within a dust aerosol plume collected during the Studies of Emissions and Atmospheric Composition, Clouds and Climate Coupling by Regional Surveys (SEAC⁴RS) field campaign are used to attempt radiative closure. Large variability for different commonly used aerosol optical models is shown for shortwave fluxes and heating rates of up to 50% and 400%, respectively. In the IR, variability is still relatively smaller, but still very large at 3% for flux and 25-50% for heating rates. Finally, it is determined that aerosol analyses from models are not sufficiently accurate to provide accurate fluxes or heating rates.

CHAPTER 1

INTRODUCTION

Before numerical weather prediction (NWP) models can perform a forecast, an initial atmospheric state must be provided to the model. This initial atmospheric state includes three-dimension temperature, moisture, and pressure fields among other variables. Importantly, this initial atmospheric state is defined at the model forecast points - typically on a three-dimensional Cartesian-like grid. The importance of the accuracy of the initial atmospheric state - also known as the initial conditions - cannot be understated. Model forecasts are based upon the forward integration of the initial conditions, and, because the atmosphere is very chaotic, very small differences in initial conditions can quickly result in large forecast differences (Lorenz, 1982). Thus, any information being used to create the initial conditions needs to be as accurate as possible to provide a reasonable forecast.

Lorenz (1982) examined impact of small initial condition perturbations on model forecasts using the European Centre for Medium Range Weather Forecasts (ECMWF) NWP model. For that study, several ECMWF model forecasts were initialized using similar initial conditions. By using the same NWP model, the forward-integrating equations are identical between the different forecasts and differences between the model forecasts can be solely attributed to the different initial conditions. By examining the forecast differences, Lorenz (1982) estimated the doubling time for small errors is approximately 2.5 days. That is, small errors present in initialization will grow rather rapidly with forecast time. Further, Ehrendorfer (1997) reported that

as NWP models become more complex (e.g., higher resolution, more realistic parameterizations for radiation, land surface, microphysics, etc.), the error doubling time shortens, amplifying the impact of small errors in initial conditions. As such, the error doubling time experienced today is much less than the two and half days reported by Lorenz (1982). While methods such as ensembling have been implemented to combat the impact of quickly growing forecast error (e.g., Lewis 2005), minimizing initial condition errors is still vital to successful NWP.

The initial atmospheric state can be determined either via subjective or objective analysis. In subjective analysis the initial conditions are drawn subjectively and this subjective analysis is used as the initial state upon which a forecast is based. In objective analysis, however, the subjectivity is removed and the analysis is created in an automated technique. An early technique of objective analysis is presented by Panofsky (1949). In that study, a third-degree polynomial is used to determine wind and pressure fields. This method was shown to provide results similar to subjective analysis, albeit with limitations such as only being applicable at relatively small areas (i.e., not valid globally). That said, such objective analysis could be automated with no human intervention required. Over the next few decades several more robust methods of objective analysis were developed (e.g., Bergthórsson and Döös 1955, Eddy 1967). While some methods of objective analysis were developed to be based entirely on observations (e.g., Panofsky 1949), other methods worked to merge observations with a background atmospheric state from a previous model forecast. For example, Gilchrist and Cressman (1954) presented an objective analysis method that used previous model forecasts to provide additional data in regions with little observational data. This method was developed further by Bergthórsson and Döös (1955) where the analysis field is constructed using both observations and a previous model forecast, even in regions with many observations. The entire process of quality controlling

data, performing objective analysis, creating a physically-balanced initial atmospheric state, and performing a short forecast to create a background atmosphere from which new observations are included is typically referred to as the data assimilation cycle, or simply, *data assimilation* (Daley, 1991).

Data assimilation is performed at all major NWP centers including ECMWF, the Japan Meteorological Agency (JMA), the National Centers for Environmental Prediction (NCEP), Météo-France, the United Kingdom Met Office, and the German Wether Service (Deutscher Wetterdienst; DWD), among others (Greer et al., 2018). For instance, NCEP uses the Global Data Assimilation System (GDAS) to create the initial conditions for the Global Forecast System (GFS) NWP model forecasts. The GDAS system assimilates observations from surface weather stations, balloon sounding systems, wind profiles, aircraft, buoys, radars, and satellites. For the assimilation of satellite observations for NWP forecasts, observations can either be provided pre-processed into a specific atmosphere variable, or provided as raw measured energy. For example, wind information derived from satellite data (i.e., processed satellite data) has been assimilated into U.S. Navy’s Coupled Ocean-Atmosphere Mesoscale Prediction System (COAMPS) using the Naval Research Laboratory Atmospheric Variational Data Assimilation System (NAVDAS; Zhao et al., 2013). Likewise, raw observations of energy (i.e., radiances) measured by satellite sensors can often be assimilated providing information about one or more atmosphere variables in a process known as radiance assimilation (Eyre et al., 1993).

Radiance assimilation is usually performed in the infrared (IR) where this method works because the opacity of the atmosphere differs at different altitudes for different wavelengths (e.g., see discussion associated with Fig. 1 below). For example, some wavelength bands have different water vapor absorption. For wavelengths with no atmospheric absorption, the atmosphere can be entirely transparent and any satellite

observing at that wavelength would measure radiant-energy - or radiation - from the Earth's surface. For instance, assume a satellite sensor measures IR radiance from a hypothetical atmosphere with no water vapor except at a layer between 1 and 2 km above the surface. If radiance is observed by the satellite sensor at a wavelength with strong water vapor absorption, the sensor would observe radiation being emitted from near the top of this water vapor layer. This is because all the energy emitted from beneath the water vapor layer would have been absorbed, and thus unable to be measured directly by the satellite sensor. Instead, the radiance measured would be emitted by the atmosphere, not the surface. Planck's law shows the amount of radiation emitted by a object at a specific wavelength is a function of the temperature of that object. Or, more specifically:

$$I_{\lambda}(T) = \frac{2hc^2}{\lambda^5(e^{\frac{hc}{K\lambda T}} - 1)}, \quad (1.1)$$

where $I_{\lambda}(T)$ is the radiance emitted at wavelength λ and temperature T , h is the Planck constant, c is the velocity of light, and K is the Boltzmann constant (Liou, 2002). Thus, in this hypothetical case, the approximate temperature of the atmosphere at 2 km altitude can be determined by the radiance measured at first band, whereas the temperature closer to 1 km can be determined by the second band's measured radiance. In reality, water vapor is distributed throughout the troposphere (the lowest layer of the atmosphere) at varying concentrations. Thus, if a satellite sensor measures energy at several wavelengths with differing water vapor absorption, a temperature and water vapor profile consistent with the observed radiances can be determined. Note, currently radiance assimilation is largely limited to the IR and microwave radiation spectrum. In the visible spectrum, scattering of light becomes non-negligible such that the measured radiance is not necessarily a function of tem-

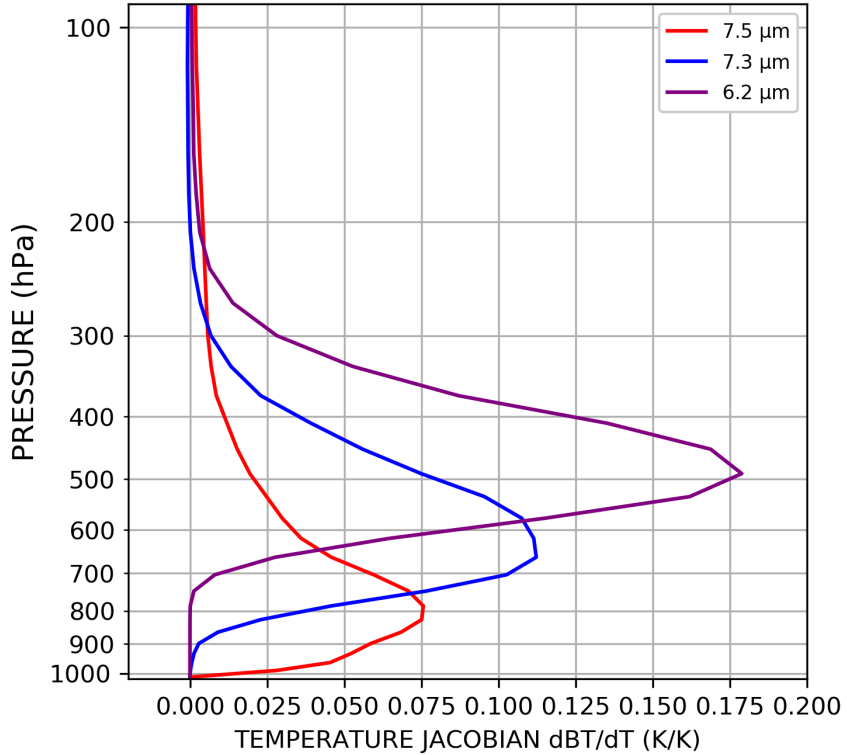


Figure 1: Temperature Jacobian for at three different infrared wavelengths in a tropical standard atmosphere from McClatchey et al. (1972). The temperature Jacobians show the sensitivity of the top-of-atmosphere measured radiance to the atmospheric temperature at each wavelength.

perature. Wien’s Displacement Law shows the wavelength of maximum emission of an object is inversely proportional to the temperature, or specifically:

$$\lambda_m = \frac{2.897 \times 10^{-3} mK}{T}, \quad (1.2)$$

where T is the temperature of the object and λ_m is the wavelength of maximum emission (Liou, 2002). For the range of temperatures measured in troposphere of 160 K to 330 K, this corresponds to wavelengths of 8.8 to 18.1 μm - well within the IR spectrum. Note, while Wien’s Displacement Law assumes objects are emitting perfectly (i.e., a blackbody), it is still a relatively good approximation.

Figure 1 shows the temperature Jacobians for three different infrared wavelengths in a standard tropical atmosphere from McClatchey et al. (1972). Temperature Jacobians indicate how much an atmospheric layer contributes to measured radiance at the specified wavelength and are sometimes referred to as vertical weighting functions (Eyre, 1991). While, the discussion thus far has been limited to water vapor opacity, some wavelengths are sensitive to the concentrations of other gases such as carbon dioxide. It is important to note that because the signal at each wavelength is dependent upon absorbing gas concentrations and temperature, there are several different atmospheres that can provide the same observed radiances. To constrain the solution, a first-guess atmosphere is provided upon which the atmospheric profile can be corrected to better match the radiance measurements. In the the assimilation cycle, the first-guess atmosphere is from a previous model forecast.

While temperature and humidity products retrieved from satellite sensors have been assimilated into model initial conditions since the 1980s, the satellite sensors had only a few relatively wide wavelength bands, and thus, very coarse vertical resolution (e.g., Tzvi et al. 1986, Menzel et al. 2018). In 2002, the first hyperspectral IR sounder (HIS) with thousands of bands, the Atmospheric Infrared Sounder (AIRS; Aumann and Pagano 1994), was launched aboard NASA’s AQUA satellite. Because HIS sensors observe radiances at up to thousands of wavelengths with bands that are often only a few nanometers wide, a large amount of data about the atmospheric composition is available. For example, the Cross-track Infrared Sounder (CrIS; Bloom 2001) instrument has 1305 spectral channels in normal spectral resolution and 2211 channels in full spectral resolution with wavelengths from 3.92 to 15.38 μm . Similar to Fig. 1, the temperature Jacobians for the CrIS sensor for every tenth band at normal spectral resolution observing the standard tropical atmosphere from McClatchey et al. (1972) is shown in Fig. 2. Obviously, even with only showing 10% of the bands

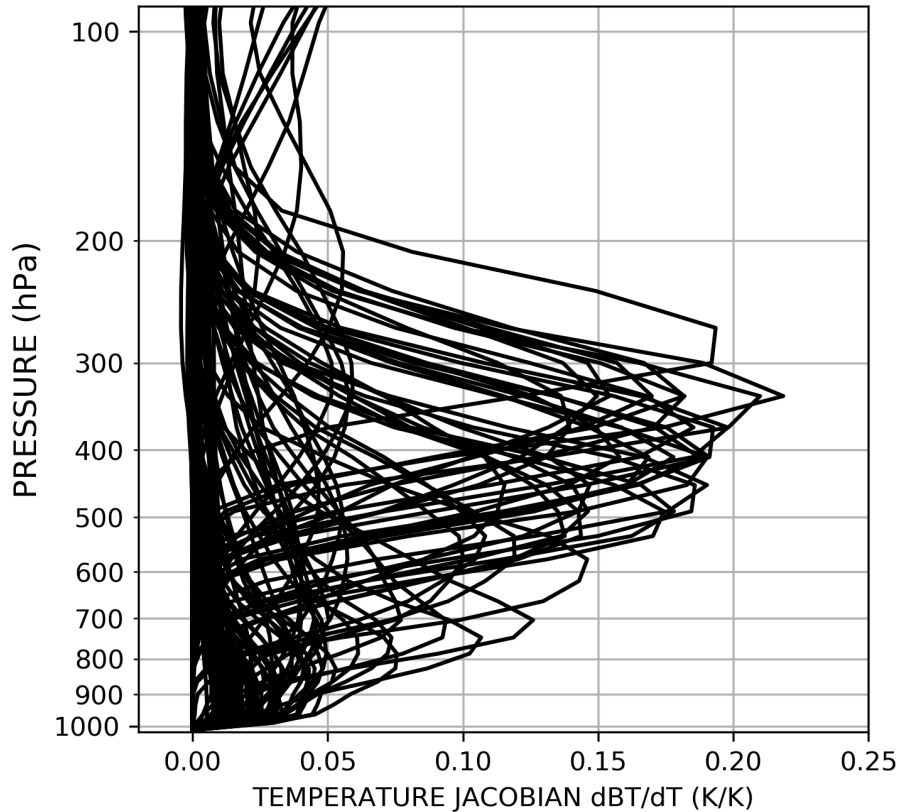


Figure 2: Temperature Jacobian for every tenth CrIS wavelength band at normal spectral resolution. Thus, 130 Jacobians are shown of the 1305 bands.

of the normal spectral resolution there is much more information available than for the 3 wavelengths shown in Fig. 1. This abundance of information has been highly beneficial to NWP efforts.

Radiance assimilation is particularly important for numerical weather prediction because it can provide observational-based initial conditions in regions that do not typically have observations. Conventionally, vertical profiles of temperature and moisture are observed via balloon sounding systems usually launched from airports. With about 70% of the Earth's surface covered by ocean, vertical observations of temperature and moisture are greatly biased to continental regions with many locations in remote oceans having no balloon-borne observations within thousands of miles. While

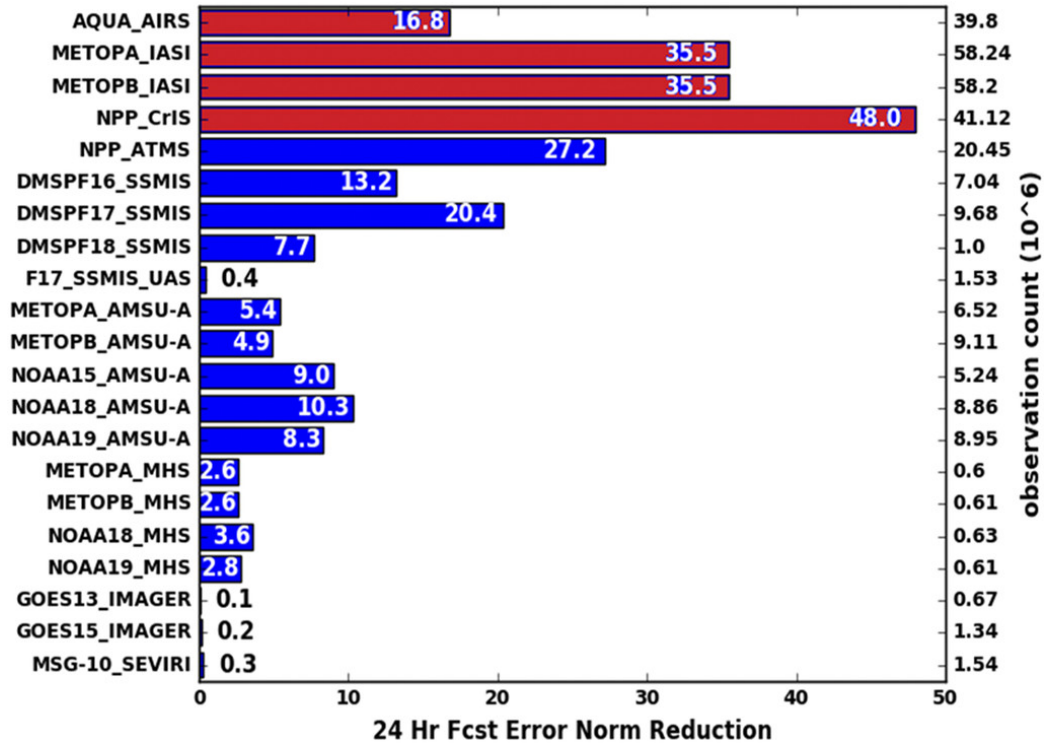


Figure 3: The 24 hour forecast error norm ($J\ kg^{-1}$) for NAVGEM for 30 days of radiance assimilation ending on 1 Jun 2017 with current HIS instruments highlighted in red. Total number of assimilated observations for each sensor reported on the right. Adapted from Marquis et al. (2021)

these locations are by definition remote, uncertainties in the analysis atmosphere in these locations can impact populated areas during typical NWP forecast periods. As such, radiance assimilation provides invaluable information about the atmospheric composition in these remote regions. For example, Honda et al. (2018) reported that assimilating IR radiances from the Japanese geostationary satellite Himawari-8 increased tropical cyclone forecast accuracy.

Assimilation of HIS radiances results in the largest decrease of forecast error of all other satellite products. For instance, Fig. 3 shows the decrease in forecast error of different satellite sensors using reduction in 24 hour forecast error norm reduction for the U.S. Navy Global Environmental Model (NAVGEM) as reported

by Marquis et al. (2021) with HIS sensors indicated in red. The 4 HIS sensors that are assimilated account for the first, second, third, and sixth sensors that result in the largest forecast error reduction while also accounting for the four sensors that provide the most observations that are assimilated. The large positive impact of HIS radiance assimilation is not limited to NAVGEM. For example, as of August 2017, HIS radiance assimilation was being performed for temperature, humidity, or temperature and humidity assimilation at ECMWF, JMA, NCEP, the Met Office, Météo-France and for the global NWP model implemented at DWD (Greer et al., 2018).

There are several operational HIS sensors currently in orbit: the AIRS sensor currently aboard the NASA-AQUA satellite, the Infrared Atmospheric Sounding Interferometer (IASI; Siméoni et al. 1997) currently aboard the Meteorological Operational (MetOp) -A, -B, and -C satellites, and the CrIS sensor currently aboard the Suomi National Polar-orbiting Partnership (Suomi-NPP) and the U.S. National Oceanic and Atmospheric Administration's (NOAA) NOAA-20 satellites. All of the above sensors are currently aboard sun-synchronous, polar-orbiting satellites. That is, the satellites orbit the Earth roughly from pole to pole as the Earth rotates beneath them. The satellites are sun-synchronous because they cross the equator at similar locations at approximately the same time every day. Thus, each satellite has a daytime overpass and a nighttime overpass. As such, each of the sensors above can sample an area roughly twice per day (once during the day, once at night).

In contrast to HIS sensors aboard polar orbiting satellites, the Chinese Geostationary Interferometric Infrared Sounder (GIIRS) is in geostationary orbit onboard the Fengyun-4 satellite (Yang et al., 2017). As such, the sensor orbits the earth once per day, such that is always directly above a specific point on the equator. Unlike the HIS sensors on polar orbiting satellites, those on geostationary satellites can measure radiances from an entire hemisphere regularly - usually at sub-hourly intervals. Due

to their demonstrated impact on NWP forecasts, many meteorological agencies are looking at launching geostationary satellites with HIS sensors. For example, the European Organisation for the Exploitation of Meteorological Satellites (EUMETSAT) will include the Infrared Sounder (IRS) on the Meteosat Third Generation (MTG) satellite (Stuhlmann et al., 2009). Further, the World Meteorological Organization (WMO) in their *Vision for the WMO Integrated Global Observing System in 2040* has recommended the placement of at least 5 geostationary satellites with HIS sensors positioned such that they provide regular full global coverage for NWP efforts (WMO, 2019).

1.1 Radiance Assimilation

Radiance assimilation is often performed by finding a meteorological analysis (i.e., initial atmosphere) that minimizes error with respect to both the background atmosphere (usually from a previous model forecast) and the observation system (Eyre et al., 1993). One way to perform this minimization is to find a solution that results in the minimization of the cost function where the cost function is given by:

$$J(x) = \frac{1}{2}(x - x_b)^T B^{-1}(x - x_b) + \frac{1}{2}[H(x) - y_o]^T R^{-1}[H(x) - y_o], \quad (1.3)$$

where x represents the analyzed atmosphere (i.e., the atmosphere that minimizes error), x_b is the background atmosphere, B is the observational error covariance matrix which describes the uncertainty of the background, $H(\cdot)$ is the forward model that converts the analysis, x , to the units of the measured properties (i.e., simulates satellite measured radiances given atmosphere x), y_o are the observations (i.e., HIS measured radiances), and R is the observational error covariance matrix which describes the uncertainty in the observations (Eyre et al., 1993). The minimum value of

the cost function $J(x)$ is associated with analyzed atmosphere x that minimizes the uncertainty in both the background atmosphere and the assimilated observations.

It is important to note NWP centers currently only assimilate HIS radiances in clear-sky atmospheres (Greer et al., 2018). In other words, the background atmosphere and the atmosphere from which the radiances are measured must contain no cloud or aerosol. If the observed radiances are observed from an atmosphere containing cloud or aerosol, the radiance innovations (given by $[H(x) - y_o]$) will not only be due to temperature and moisture, but the presence of the cloud or aerosol. Thus the minimization of the cost function will result in a solution that likely has not minimized temperature and humidity uncertainty. HIS radiances must be strictly screened for aerosol and cloud contamination, accordingly.

1.2 Cloud & Aerosol Impacts in Other Satellite Products

Despite attempts at screening, residual clouds and aerosols have been found in many satellite derived products. For example, Marquis et al. (2017) found residual cirrus clouds in approximately 25% of all assimilation-quality, IR-retrieved sea surface temperatures (SST) in the tropics. For those SST retrievals, cloud screening was performed using threshold and spatial homogeneity tests that examine both the retrieved SST as well as additional information from the sensor making the retrieval (e.g., visible wavelength observations). Additionally, SST retrievals that are far from the climatological SST for that region are rejected (Brown et al., 1999). Despite the strict cloud-screening, SST retrievals in regions such as Southeast Asia were found to have residual cirrus cloud in over 80% of all retrievals. Globally, Marquis et al. (2017) found the average contaminating cloud caused biases of 0.33° to 0.55°C . Similar to Marquis et al. (2017), Ruescas et al. (2011) found dust aerosols also contaminated IR-retrieved SSTs.

Clouds and aerosols that pass screening are overwhelmingly semi-transparent (e.g., Ruescas et al. 2011, Marquis et al. 2017). Semi-transparent clouds and aerosols are opaque enough to change atmospheric opacity and emit radiance, but transparent enough that lower layers of the atmosphere and the surface features are still "visible" to the satellite sensors. While aerosol layers are often semi-transparent, the stereotypical view of a cloud is fully opaque. Cirrus clouds, however, are not only largely semi-transparent, but very common. Specifically, using active remote sensing methods that can identify very thin cirrus clouds, these clouds are detected over 40-60% of the globe at any time (Mace et al., 2009), with the overwhelming majority of these cirrus clouds being very transparent - exhibiting visible optical depths below 0.30 (i.e., approximately 75% transmissive; Campbell et al., 2015). As such, cloud and aerosol contamination is not unexpected and is present in nearly all passive-based observations.

1.3 Residual Cloud and Aerosol

Due to contamination in other satellite products, it is likely there is residual cloud and aerosol in assimilated HIS products. To screen clouds and aerosols, the NAVDAS system imparts checks on the observed radiances to be assimilated before assimilation can occur. These checks include innovation threshold tests and radiance discontinuity tests. Specifically, the NAVDAS system rejects observations with background innovations (given by $[H(x_b) - y_o]$) that are above 3 times the observational error, corresponding to approximately 3 K. For discontinuity tests, the system examines the observed radiance at bands with different altitude peaks. If a spike, or discontinuity, is present in the observed radiance that is measured by all bands with lower altitude peaks, it is assumed that cloud or aerosol is contaminating the observed radiances. In NAVDAS, this discontinuity threshold is approximately 0.5 K (Marquis et al., 2021).

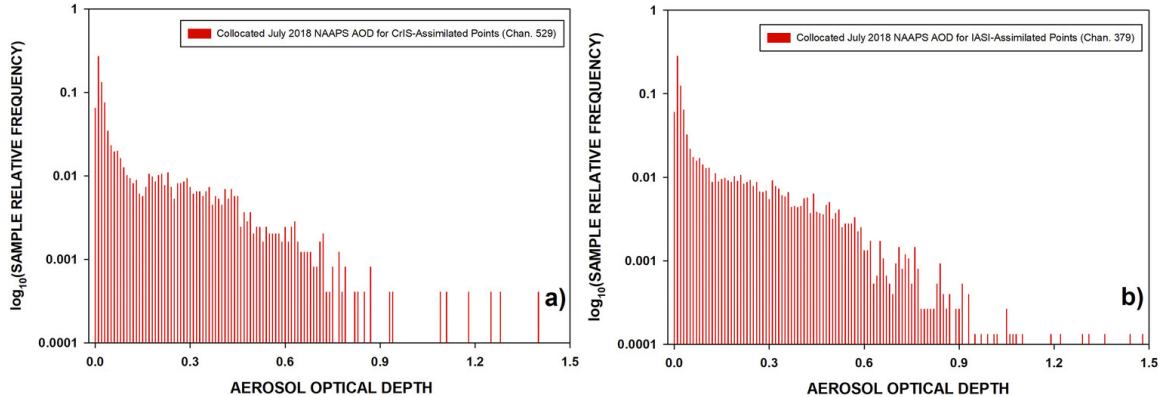


Figure 4: Histograms of aerosol optical depth of assimilated aerosol-contaminated HIS radiances from (a) CrIS channel 713 and (b) IASI channel 379 from July 2018. Adapted from Marquis et al. (2021).

Since cirrus clouds and aerosol layers can be largely transparent, these thresholds may not be met allowing contaminated observations to be assimilated. Thus, it is important to determine if, and how much, aerosol and cloud pass these screening methods.

To determine the frequency of aerosol contamination in HIS radiances assimilated by NAVDAS, all observations from CrIS channel 529 (10.2 μm) and IASI channel 379 (13.5 μm) for July 2018 are examined. These bands indicate tropospheric peaking wavelengths that should be contaminated by the presence of aerosol in the troposphere. Specifically, the CrIS channel peaks near 950 hPa (about 0.5 km above mean sea level; AMSL) and the IASI channel peaks around 600 hPa (about 4.5 km AMSL), though both bands are impacted by the atmosphere both above and below these peaks.

By co-locating - in space and time - the assimilated observations with aerosol analysis fields from the Navy Aerosol Analysis and Prediction System (NAAPS), contamination statistics can be estimated. Analyses from NAAPS have been shown to correlate well with observations (correlations of 0.7-0.8; e.g., Zhang et al., 2008;

Lynch et al., 2016). The contamination results are shown in Fig. 4. Overall, 93.1% of all CrIS assimilated observations from and 94.0% of all IASI assimilated observations that were identified as clear-sky by NAVDAS contain aerosol contamination at visible (532nm) optical depths above 0.01. Aerosol optical depth (AOD) is a column-integrated measure of how much light at a certain wavelength is extinguished by aerosols, either through absorption or scattering/reflection and is proportional to the total aerosol mass loading above a location. This high rate of contamination is not-unexpected at these very low AODs since the average AOD in even remote oceans is approximately 0.06 (Kaufman et al. 2001, Smirnov et al. 2011). Thus, it is better to examine the frequencies of contamination at higher AODs. For assimilated CrIS observations, 32.1% are contaminated by aerosols with optical depths above 0.1, while IASI has similar, albeit slightly higher, contamination rate at 34.9%. Likewise, 15.6% and 16.4% of assimilated observations from CrIS and IASI, respectively, are contaminated by aerosols with optical depths above 0.3. While screening seems less effective for IASI, this may be due to the higher altitude peak for that band not being as sensitive to lower aerosol layers. That said, it is important to reiterate that the IASI band can still be impacted by aerosol layers closer to the surface as the temperature Jacobians can extend below their peak altitude.

Similar to aerosol contamination, cloud contamination of NAVDAS assimilated HIS observations can be determined. In this case, however, assimilated AIRS observations at channels 122 (13.85 μm) and 136 (13.49 μm) are co-located with lidar cloud profiles retrieved from the Cloud-Aerosol Lidar with Orthogonal Polarization (CALIOP; Winker et al. 2010) aboard NASA's Cloud-Aerosol Lidar and Infrared Pathfinder Satellite Observation (CALIPSO) satellite. Unlike passive-based observations, the CALIOP sensor is a lidar that uses active remote sensing where a pulse of light from a laser is shot down towards the Earth with the light reflected being mea-

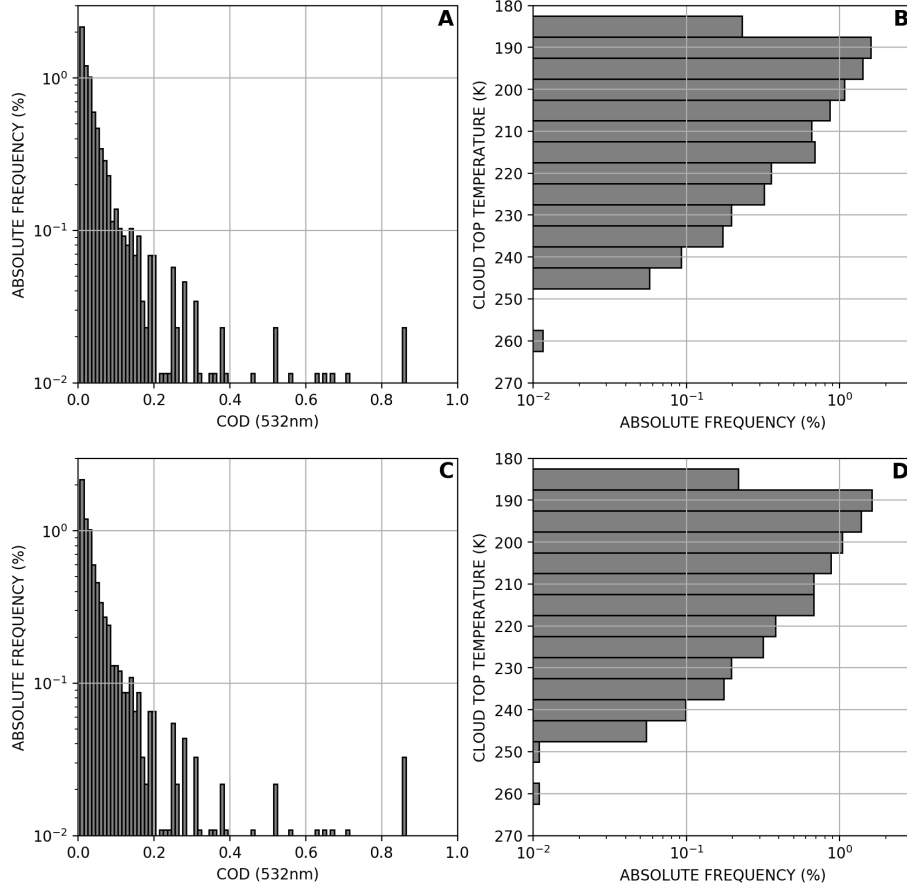


Figure 5: Histograms of cirrus cloud contamination in assimilated observations from (a & b) AIRS band 122 ($13.85 \mu\text{m}$) and (c & d) AIRS band 136 ($13.49 \mu\text{m}$) as a function of visible cloud optical depth (a & c) and cloud top temperature (b & d).

sured. This allows the CALIOP lidar to determine cloud layers that passive sensors cannot (Winker et al., 2010). As such, co-location using CALIOP has been used to determine cloud contamination in other passive-based satellite retrievals (e.g., Toth et al., 2013; Marquis et al., 2017). The histograms of cirrus cloud contamination in the two AIRS bands are shown as a function of visible (532 nm) cloud optical depth (COD) and cloud top temperature in Fig. 5. Note, cloud top temperature is used as a proxy for cloud top altitude since the microphysical and thus optical properties of clouds are highly dependent upon temperature (e.g., Heymsfield et al. 2014).

Overall, 7.7% of all assimilated observations from either of the two AIRS bands are contaminated by cirrus clouds, with most contaminating clouds exhibiting CODs below 0.1. While this contamination rate is much less than that exhibited by aerosol contamination, this is not necessarily unexpected. Since aerosols are usually much lower in altitude than cirrus clouds, aerosols are unlikely to impact as many spectral bands. Further, because aerosol layers are lower in altitude, aerosol layers often exhibit temperatures closer to the lower atmosphere and surface than high altitude cirrus clouds do. Thus, while aerosol plumes may impart relatively less significant bias because it is emitting similar radiation to the lower atmosphere, a cirrus cloud of the same optical depth will have a much stronger impact due to its much colder temperature. These two factors likely lead to better cloud screening. That said, with other passive radiometric-based observations exhibiting much higher contamination rates (e.g., approximately 25% for IR-SST retrievals; Marquis et al. 2017), this may indicate overly strict screening causing clear-sky observations to be rejected.

As the above figures show, assimilated HIS observations are contaminated by clouds and aerosols. The impact of this contamination has yet to be examined. Below, three studies are presented that examine the impact of clouds and aerosols on NWP. Specifically, Chapter 2 examines the impact of assimilating aerosol-contaminated HIS observations on analyzed temperature and humidity profiles. In Chapter 3, estimates of analyzed temperature and humidity profile biases due to assimilating cirrus-contaminated HIS radiances are presented. Chapter 4 presents a study determining the importance of aerosol optical models for NWP. The overall results and conclusions of this dissertation are presented in Chapter 5.

CHAPTER 2

AEROSOL INDUCED ANALYSIS BIAS

2.1 Introduction

2.1.1 Rationale

As shown in section 1.3, a large number of assimilated HIS observations are contaminated by aerosols, presumably causing errors in the analyzed initial atmosphere. Since these errors are likely to amplify over short forecasts, a proper understanding of these errors is of great importance. Examination of the cost function (Eq. 1.3) shows that aerosol-induced HIS observation bias can lead to analysis error, but the magnitude of error is dependent upon the background atmosphere, the background error covariance matrix, the observation error matrix, and the magnitude of aerosol-induced bias on observations. In this chapter, an experiment estimating analysis error using aerosol biased HIS observations is presented.

2.1.2 Background

Aerosols are suspended solid particles or liquid droplets in the air that originate from the condensation of gases or the mechanical weathering of the Earth's surface. Aerosols are typically classified into three categories based upon their size and formation mechanism. The smallest aerosols form when gas molecules cluster together and nucleate into a *nucleation-mode* aerosol. Nucleation-mode aerosols are very small ($< 10^{-8}$ m in diameter). As gas molecules condense upon nucleation-mode aerosols and individual aerosols collide and coagulate, the nucleation-mode aerosols can grow

to *accumulation-mode* aerosols. These accumulation-mode aerosols ($10^{-8} - 10^{-6}$ m) are still small enough to remain suspended and are often removed via precipitation processes. Conversely, aerosols that form via wind erosion are much larger ($10^{-6} - 10^{-5}$ m) and called *coarse-mode* aerosols. While these coarse aerosols can be removed via precipitation processes, they often settle due to their larger mass preventing continuous suspension. Aerosols are classified using both their type and size. For example, soot refers to organic aerosols emitted during the combustion process or forming from gases formed during combustion. Soot would further be classified by size to accumulating- and nucleating-mode aerosols (Jacob, 1999).

When light interacts with aerosols, it can either be absorbed or scattered away in different angles. Different aerosols will have different absorption and scattering characteristics - known optical properties. For example, in the IR, soot aerosols are largely transparent whereas dust aerosols absorb, but have negligible scattering (Hess et al., 1998). Thus, because aerosol-induced analysis biases will only be present if the assimilated radiances are biased, it is important to only focus on aerosols that are likely to bias IR radiances. To ensure "IR-active" aerosols are examined, this study focuses specifically on mineral dust. Note, while other aerosols may be active in the IR (e.g., volcanic ash), dust is more widely present and the study can be limited to regions most likely to be primarily under the impacts of mineral dust.

Dust aerosols are primarily generated from agricultural land and, more important to this study, deserts. As such, large dust AODs are more likely in certain regions. For example, Voss and Evan (2020) showed mean dust visible AOD in the Tropical Atlantic off the coast of Saharan Africa of over 0.4 and 0.5 in the Boreal spring and summer, respectively. Similarly, the mean AOD over the Arabian Sea in the summer was found to be over 0.8. Additionally, AODs over 0.1 are present in Bay of Bengal,

the Caribbean Sea, and the North Pacific during the Boreal Summer. As such, all of these regions are likely to exhibit dust-induced analysis error.

Concerningly, several of these regions with relatively high dust AOD present important zones for tropical cyclone development. For instance, tropical cyclones form in the summer in the Tropical Atlantic, the Caribbean Sea, the Bay of Bengal, and the Arabian Sea. Since tropical cyclone formation occurs over the open ocean, traditional observations of vertical temperature and moisture profiles are typically unavailable. Thus, NWP analyses are highly dependent upon HIS radiance assimilation in regions that are likely to experience dust contamination and high-impact weather events.

As for specific impacts of dust to HIS radiances, Pierangelo et al. (2004) showed the impact of dust on HIS radiances while examining methods of retrieving dust optical depth and altitude using HIS sensors. Because determining bias was not the goal of Pierangelo et al. (2004), the study was rather idealized and did not examine impacts of assimilating dust biased observations. Pierangelo et al. (2004) used a radiative transfer model (RTM) to simulate measured radiances from the AIRS sensor. RTMs numerically solve the radiative transfer equation to provide simulations of radiative transfer in the atmosphere. Thus, they can be used to determine the radiative effects of clouds and aerosols (e.g., Campbell et al. 2021) or simulate satellite observations, as is done here. By performing clear-sky simulations and simulations varying dust altitude, optical depth, and aerosol model, the impact on measured brightness temperature was estimated. Brightness temperature is the temperature in Eq. 1.1 that provides the measured radiance and is related to an object's actual temperature via that object's emissivity at the measured wavelength. Pierangelo et al. (2004) found that for an aerosol layer at 2400 m altitude, brightness temperatures were cooled by up to 5 K at 10 μm wavelength for a visible AOD of 0.75 and over 10 K for an AOD of 2.5. They also found that for a visible AOD of 1.5, brightness temperatures at

10 μm were cooled by <4 K for dust aerosol at 800 m and 13 K for dust at 4100 m. Finally, when comparing different dust aerosol types from the Optical Properties of Clouds and Aerosols (OPAC; Hess et al. 1998) database, they found negligible differences between transported-mode mineral dust and coarse-mode mineral dust at 10 μm wavelength, but larger differences of about 40% at 13 and 4 μm wavelengths, respectively.

As shown in Fig. 4, a significant percentage of assimilated HIS observations are contaminated by aerosol. Since dust aerosols are active in the IR, present in large AODs in many regions and periods important for tropical cyclone development and forecasting, and able to impart large cold biases on HIS observations, it is highly important to examine what impacts dust has on analyzed temperature and humidity profiles. In this chapter, a study estimating this impact by assimilating synthetic over-ocean HIS radiances created using observations of dust retrieved off the Atlantic coast of Saharan Africa is presented. In section 2.2, the datasets and models used for the experiment are examined, in section 2.3, the methodology used to estimate the dust-induced analysis bias is explained, in section 2.4 the findings are reported, and in section 2.5 the impact of the findings are discussed.

2.2 Datasets & Models

2.2.1 RTTOV

For radiative transfer, the Radiative Transfer for TOVS (RTTOV) version 11.2 is implemented (Hocking et al., 2013; Saunders et al., 2013). RTTOV is a fast radiative transfer model originally developed in the early 1990s for the TIROS Operational Vertical Sounder (TOVS) which had a total of 20 IR bands peaking in the troposphere, 3 IR bands peaking in the stratosphere, and 4 microwave bands (Eyre, 1991).

RTTOV allows both forward and gradient radiative transfer calculations. In forward radiative transfer, simulated radiances are calculated from a user provided atmospheric profile. In the gradient radiative transfer calculations, however, the impact of the change in some state variable on radiances can be calculated. The RTTOV state variables are temperature, variable gas concentrations, cloud properties, and surface properties. In other words, it can calculate the temperature Jacobians like those shown in Figs. 1 and 2 as well as Jacobians for other variables (e.g., moisture). This makes RTTOV valuable for radiance assimilation.

To perform forward and gradient radiative transfer, an atmospheric profile must be provided to RTTOV. Users must provide an atmospheric profile at any vertical pressure levels of temperature, water vapor gas concentration, cloud properties (if applicable), and surface properties. Additionally, users can also provide profiles of ozone, carbon dioxide, nitrous oxide, methane, and carbon monoxide gas concentrations. To decrease computational load, RTTOV implements coefficient files which provide optical depth calculations for a range of different temperature and water vapor concentrations for several different satellite sensors. For this study, the 54-vertical-level coefficient files for the CrIS sensor on Suomi-NPP are used.

The output of the RTTOV forward model is the simulated radiances for the specified wavelengths. The range of wavelengths upon which RTTOV simulations can be performed is dependent upon the range in the available coefficient files and is approximately 0.4 - 50 μm in the visible/infrared and 10 - 200 GHz in the microwave. When the gradient radiative transfer code is run, the system outputs the Jacobian matrix for the specified state variables. That is, for each wavelength, for each variable, that wavelength's sensitivity to variable changes at each altitude is returned.

2.2.2 1DVar System

For assimilation experiments, a modified version of the EUMETSAT Numerical Weather Prediction Satellite Applications Facility (NWP SAF) one-dimensional variational (1DVar) version 1.1 assimilation system is used (Smith, 2017). The 1DVar system is an assimilation system that allows for the retrieval of atmospheric profiles for nadir-viewing passive sounding instruments. The system minimizes the cost function shown in Eq. 1.3 either through Newtonian or Marquardt-Levenberg minimization methods. In the univariate case, the Newtonian minimization method solves for the minimum in an iterative process by approximating the univariate function by a quadratic. The next iteration is then focused on location of the minimum of the quadratic found in the previous example. In the multidimensional case, the method fits a multidimensional parabolic function to the shape of the multidimensional cost function for some atmosphere using Jacobian matrices (Doicu et al., 2002). The Marquardt-Levenberg minimization method interpolates between the Newtonian method and a method known as gradient descent where the minimum is found by just moving down the slope at a point. As such, the Marquardt-Levenberg minimization method is a bit more robust than the Newtonian method and will be more likely to find a minimum even if the first guess is far from the minimum (Levenberg, 1944). A flowchart showing the process to determine the analysis atmosphere is shown in Fig. 6.

For the study presented here, the 1DVar system has been built with the RTTOV RTM for innovation and Jacobian calculations. The minimization method used is the Newtonian method with a maximum of 10 iterations. Cost function minimization is achieved when the change in cost function is less than 1%. To perform assimilation, the 1DVar system requires a background temperature and water vapor profile defined at vertical pressure levels, observed radiances, a background error covariance matrix,

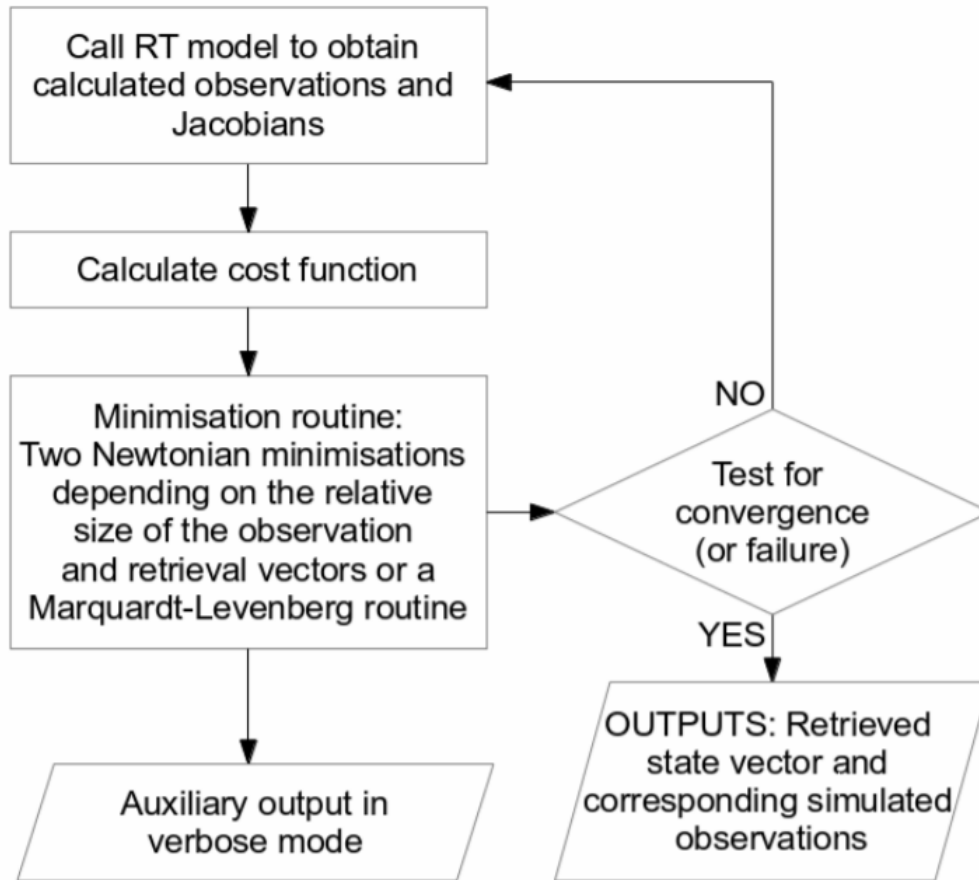


Figure 6: Flowchart indicating the process used in the 1DVar system to determine the analysis atmosphere. Adapted from Havemann (2020)

and an observation error covariance matrix all in ASCII text files. Additionally, all observations for the CrIS normal spectral resolution bands are assimilated.

The 1DVar system has been modified to allow user input of aerosol number concentration profiles for the aerosol types defined in OPAC (discussed in section 2.2.8). To achieve this, a new subroutine has been added to the 1DVar source code to read in aerosol number concentrations from a single ASCII text file containing number concentrations for each of the 10 OPAC aerosol types at each vertical pressure level defined in the provided background atmosphere. As such, users can provide either a

single aerosol type or any mixture of aerosols. The 1DVar system then enables aerosol calculations and provides the aerosol number concentrations to the RTTOV forward model - the model calculating the innovations (i.e, $[H(x) - y_o]$ in Eq. 1.3). Aerosol calculations are also enabled in the RTTOV gradient model. This is the model that calculates the Jacobian matrices. For the Jacobian calculations, the aerosol is provided as a constant. That is, the aerosol is allowed to change the temperature and moisture Jacobians, but there are no aerosol Jacobians as aerosol is not allowed to change between background and analysis.

The 1DVar system is modified to attempt to decouple the impact of the aerosol during radiance assimilation. By adding constant aerosol profiles in the forward model, the background atmosphere, and the analysis atmosphere each term in the cost function (Eq. 1.3) has like aerosol impacts. Specifically, aerosol is constant between the background atmosphere and the analysis atmosphere, thus the difference in aerosol fields in the analysis increment (given by $[x - x_b]$) is zero. Likewise, by including aerosols in the forward model, it is ensured that for a perfect observation (i.e., no error) and a perfect background, the innovation term (given by $[H(x) - y_o]$) must be zero. These modifications can be effectively disabled by providing an aerosol number concentration file containing just 0's. To ensure this is the case, runs with zero aerosol are compared to those from an unmodified version of the 1DVar system and both systems provided identical output.

The 1DVar system can output up to 9 ASCII text files. When run without enhanced diagnostics, the system outputs *Retrieved_BTs.dat* and *Retrieved_Profiles.dat*. The first file contains the provided observed radiances, the radiances simulated from the background atmosphere ($H[x_b]$), and the radiances simulated from the analysis atmosphere ($H[x]$). The second file includes the provided background atmosphere and the analysis increment ($x - x_b$) for each of the retrieved variables (temperature

and humidity in this case). The analysis atmosphere, x , can easily be found using the background atmosphere.

2.2.3 Error Covariances

To minimize the cost function shown in Eq. 1.3, background and observation error covariance matrices are needed. Specifically, the background error covariance matrix provides information on a probability distribution function of background errors. In operational data assimilation where the background atmosphere is from a previous model forecast, these background errors are forecast errors. The background error covariance matrix includes information on how errors in a variable correlate with errors in that same variable at a different location (i.e., altitude in this case) known as autocovariances. Additionally, the correlation in error from one variable to another are included and known as the multivariate covariances. The background error covariance can be constructed using model ensembles with slightly different initial conditions, by analyzing innovations, or by examining differences in a forecast with different forecast length (Bannister, 2008). In this study, the sample 54-level background error covariance matrix included in the 1DVar source package is used (Weston et al., 2014).

The observation error covariance contains information on the probability distribution function of the random noise present in observations from a sensor and the error from the forward RTM. Specifically, the error from the forward RTM is due to errors implicit in the RTM, representativeness errors associated with using a background atmosphere defined at specific levels, and pre-processing errors. The errors between the forward model and observations are assumed to be uncorrelated. Further, it can usually be assumed that the random noise in observations is uncorrelated between channels, though this is not always the case and is dependent upon sensor design

(Weston et al., 2014). When correlations between channels are assumed zero, the observation error covariance matrix can be simplified to an observation error variance vector. In other words, the combined uncertainties at each channel can be described by a single value equal to the standard deviation of the error. In the case of sensors with correlated error, an error variance may be used with each term inflated to account for the unknown correlations (Weston et al., 2014). The observation error can be determined using the background and analysis innovations (Desroziers et al., 2005) or by directly comparing to observations with higher accuracy. For this study, the observation error variance for the CrIS sensor aboard the Suomi-NPP satellite provided in the 1DVar source package is used.

2.2.4 Tenerife, Canary Islands, Spain

Observations used in this study are from the island of Tenerife, Spain in the Canary Islands approximately 300 km to the northwest of the region of Western Sahara on the African continent. All observations required for this study are taken on the island. Additionally, due to the island’s location with respect to the Saharan Desert of North Africa, Tenerife experiences dust aerosol events during easterly flow (Baldasano et al., 2013). Viana et al. (2002) reports that the air masses reaching the Canary Islands and Tenerife are from the African continent 25% of the time. They also report that during the summer, often times transport from the African continent happens above the oceanic boundary layer (e.g., 2500 m AMSL). The location of Tenerife and the observation sites used in relation to the African continent and the Sahara Desert is shown in Fig. 7. Note, the Canary Islands (and Tenerife) lie on the northern edge of the region with the highest AODs as reported by Alfaro-Contreras et al. (2017). Specifically, the mean AOD in this region is approximately 0.2, whereas regions further south, around 10°N, experience a mean AOD of near 0.4. Thus, while

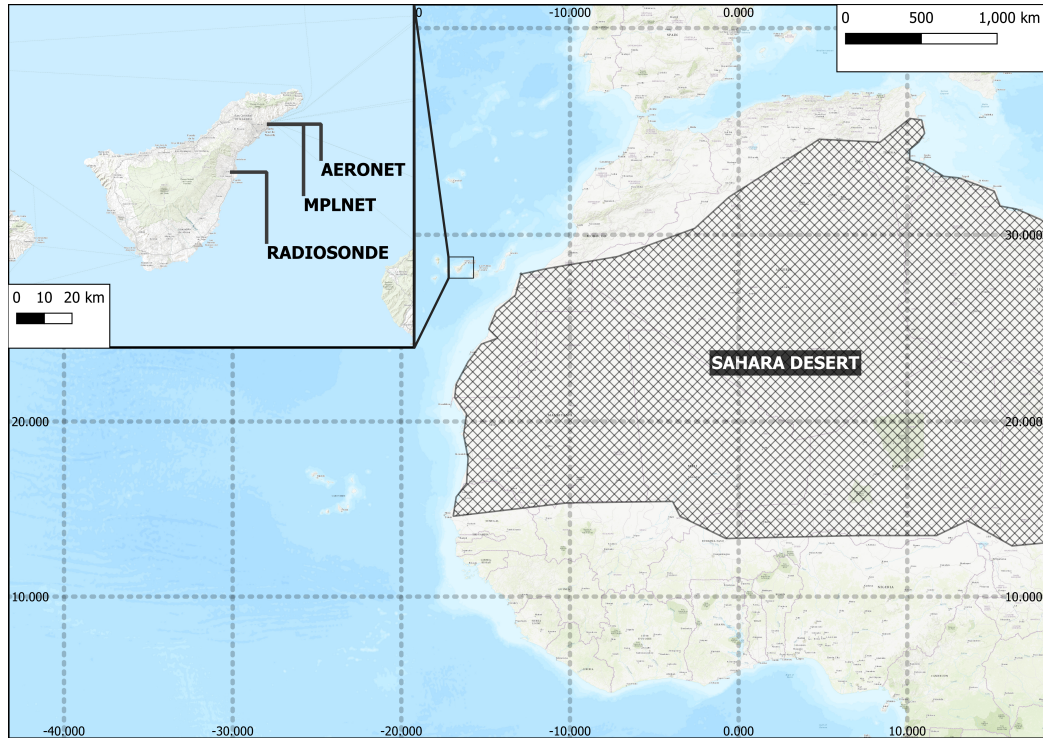


Figure 7: Location of observation sites used in Tenerife, Canary Islands, Spain with the Sahara Desert shaded. Created with QGIS V3.16.6.

a study region further south may be more appropriate, the Tenerife sites are the closest to that region while still having all required observations. That said, as shown by Viana et al. (2002), the dust is elevated at Tenerife, possibly impacting HIS observed radiances more due to increased thermal contrast with the lower atmosphere and surface. Such an elevated dust layer also allows estimation of the impact of elevated dust on bands that may peak in the mid-to-upper troposphere. To further ensure presence of dust, the study is limited to the June - November period consistent with the furthest north extent of the African easterly jet and dust transport to the Canary Islands (Grist, 2002).

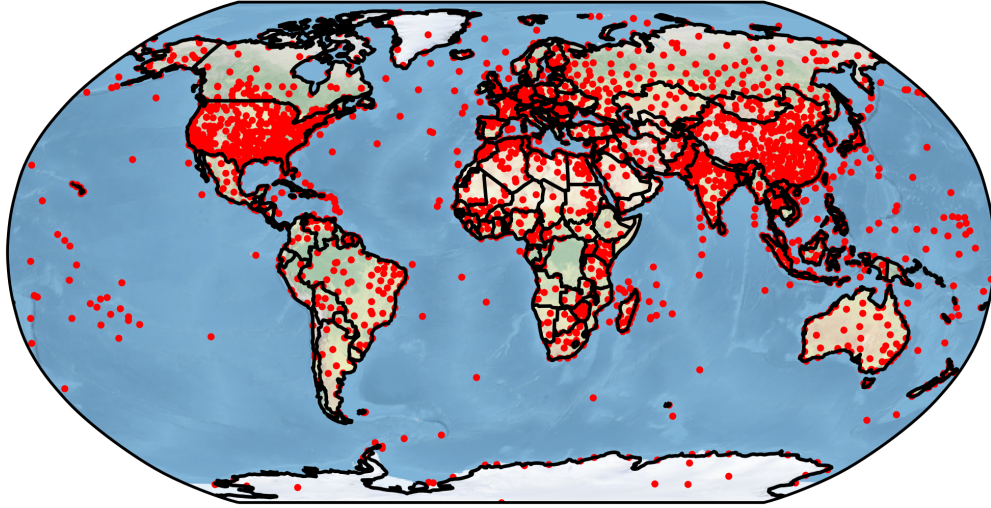


Figure 8: Locations of all sites with at least one radiosonde launch in 2020 or 2021. Created using Python v3.8.5 and Cartopy v0.18.0.

2.2.5 Meteorological Profiles

The meteorological profiles used in this study are retrieved from radiosonde observations. Radiosondes are balloon-borne instrument packages that measure temperature, humidity, and pressure, providing vertical profiles of these variables. Radiosondes are launched once or twice-daily at stations around the globe and are able to take measurements during their ascent up to the stratosphere. Radiosondes are usually launched around 0000 UTC and 1200 UTC with special soundings coming at other times. The locations of all sounding sites active in 2020 or 2021 is shown in Fig. 8.

For this study, all radiosondes launched from Güímar, Santa Cruz de Tenerife, Spain (28.3183°N , 16.3822°W , 105.0 m AMSL) between 2008-2014 are used. Radiosonde launches here are performed regularly at 0000 UTC and 1200 UTC (12:00 AM and 12:00 PM local time; 1:00 AM and 1:00 PM local time during summer daylight savings). The radiosonde launch location in Güímar on the island of Tenerife is shown in Fig. 7. Radiosonde profiles are retrieved in ASCII text files from the

University of Wyoming Atmospheric Sounding website¹. Soundings without data at altitude above 100 hPa are rejected. To supplement the atmospheric soundings from Güímar, a standard tropical atmosphere from McClatchey et al. (1972) is used. Additionally, atmospheric profiles from NASA Global Modeling and Assimilation Office (GMAO) Modern-Era Retrospective analysis for Research and Applications, Version 2 (MERRA-2) are used (Gelaro et al., 2017).

2.2.6 Aerosol Observations from AERONET

The AErosol RObotic NETwork (AERONET) is an observational network of visible sun photometers (Holben et al., 1998). AERONET measures AOD at several wavelengths during daytime using observations of attenuated sunlight to determine optical depth following the Beer-Lambert law:

$$I(\lambda) = I_0(\lambda)e^{-\tau_\lambda}, \quad (2.1)$$

where $I(\lambda)$ is the measured radiance at wavelength λ , $I_0(\lambda)$ is the top-of-atmosphere (i.e., unattenuated) radiance at wavelength λ , and τ_λ is the optical depth at wavelength λ . The AERONET AOD measurement uncertainty is approximately 0.01 - 0.015 (Holben et al., 1998).

For this study, the Spectral Deconvolution Algorithm (SDA) version 4.1 with version 2 direct-sun AOD inputs level 2.0 AERONET AOD observations from Santa Cruz de Tenerife (28.4728°N, 16.2469°W; 52.0 m AMSL) are used. The location of the AERONET site is shown in Fig. 7. While the observations of AERONET include fine-mode and coarse-mode AOD at several wavelengths, only AODs at a wavelength

¹<http://weather.uwyo.edu/upperair/sounding.html>

of 550 nm are used here. During the study period of 2008 - 2014, AOD observations are recorded during >96% of days.

2.2.7 Aerosol Observations from MPLNET

The NASA Micro-Pulse Lidar Network (MPLNET) is a network of Micro-Pulse Lidar (MPL) systems designed to retrieve information on the vertical structure of aerosols and clouds (Welton et al., 2001; Campbell et al., 2002). MPL systems are ground-based lidars that, similar to CALIOP, send pulses of light into the atmosphere and measure the amount of light that has been scattered back towards the sensor. As such, the vertical distribution of clouds and aerosols can be detected. Similarly, due to the use of active remote sensing methods, thin clouds and aerosol layers that are not reliably detectable via traditional passive remote sensing methods can be identified using MPL measurements.

The MPL at Santa Cruz de Tenerife (28.4720°N, 16.2470°W; 52.0 m AMSL) is within 10 m of the AERONET location (indicated on Fig. 7). The Santa Cruz de Tenerife MPL has a data record going back to 2005 though the system was offline during 2010. During the study period of 2008 - 2014 data is available during >90% of days (excluding 2010). For this study, Version 3 MPLNET Level 1.0 Normalized Relative Backscatter (NRB) at 523 nm is used (Campbell et al., 2002). Note, at the time of this study, aerosol extinction profiles from MPL were not available for the Santa Cruz de Tenerife site.

2.2.8 OPAC

The RTTOV RTM is built with aerosol optical properties from the Optical Properties of Aerosols and Clouds (OPAC; Hess et al., 1998) software package. This package provides microphysical and optical properties of 9 clouds and 10 aerosol types. OPAC

can provide 18 different optical parameters including optical properties of extinction coefficient, scattering coefficient, absorption coefficient, single-scattering albedo, asymmetry factor, and optical depth. Optical properties are defined at 61 wavelengths between 0.25 - 40 μm and 8 relative humidity values and are interpolated to the requested wavelength and relative humidity.

2.3 Methodology

As mentioned in section 2.2.2 to perform assimilation and determine analysis bias, a background atmosphere and observed radiances are required. For this study, synthetic radiances simulated using RTTOV are used. The process of developing the background atmosphere and synthetic HIS observations is described in this section.

2.3.1 Meteorological Profiles

For consistency, all radiosonde observations of temperature and dew point are interpolated to the vertical pressure levels defined in the background error covariance matrix. Interpolation of temperature and dew point are performed linearly with the natural logarithm of pressure as described in Section 3.2.3.1 in Askelson (2002). Note, all radiosonde observations without temperature and/or humidity reported at altitudes up to 100 hPa are rejected.

The background error covariance matrix to which the meteorological profiles are interpolated has pressure levels from 1050.000 - 0.005 hPa while the balloons used for radiosonde observation often burst at pressure altitudes of 13 - 9 hPa (Cullis et al., 2017). This corresponds to an altitude of 30 - 35 km whereas the top of the background error covariance matrix is approximately 75 km in altitude. Further complicating matters, due to very low temperatures, humidity measurements at high altitudes exhibit high uncertainties (Miloshevich et al., 2001). To rectify these issues,

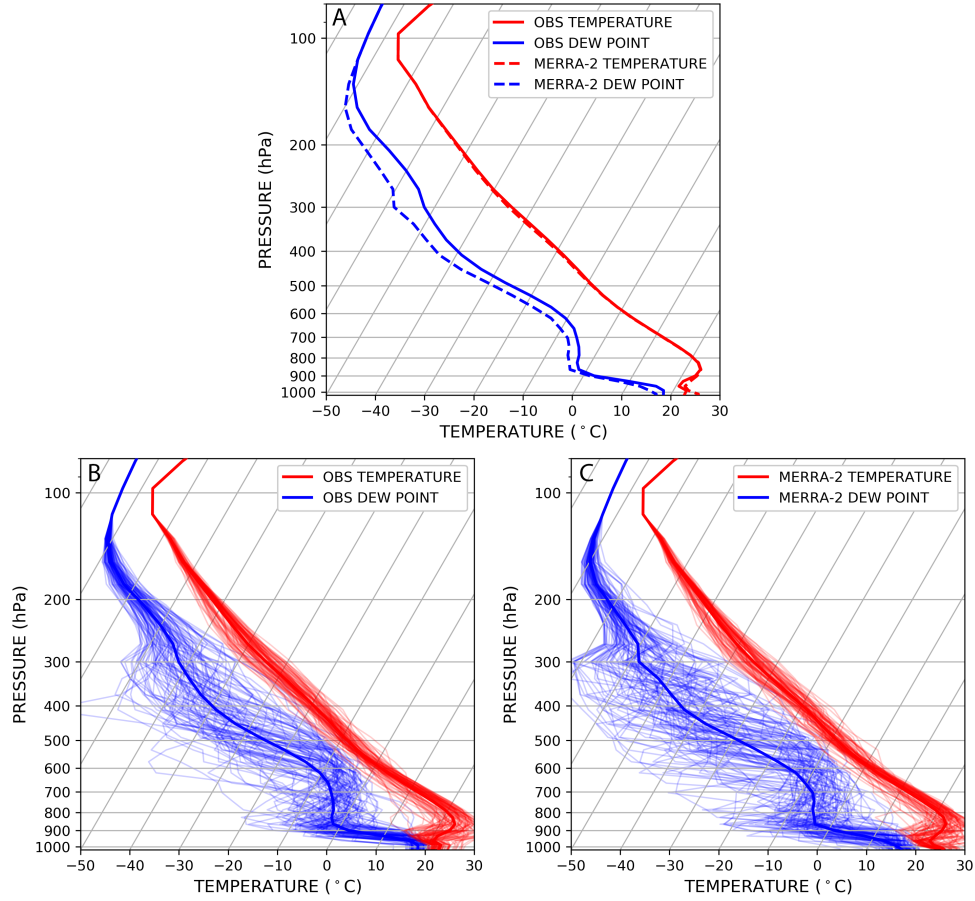


Figure 9: (A) Mean temperature (red) and dew point (blue) profiles from merged radiosonde-standard atmosphere (solid) and MERRA-2 reanalysis bilinearly interpolated to the radiosonde launch location (dashed). Also indicated is (B) all obs profiles and (C) corresponding MERRA-2 profiles passing quality checks.

the observed temperature and humidity profiles are merged with the McClatchey et al. (1972) standard tropical atmosphere. This merging is performed such that at altitudes below 300 hPa, only the observed temperature and humidity is used. At altitudes above 100 hPa, only the standard tropical atmosphere is used. Between 300 hPa and 100 hPa, the observed profile is linearly merged with the standard atmosphere with pressure altitude. The mean of all merged atmospheric profiles used in this study is shown in Fig. 9 along with each of the observed profiles used.

An additional experiment using a non-perfect background (discussed in detail in section 2.3.6) makes use of MERRA-2 reanalysis temperature and humidity profiles for the background atmosphere. The MERRA-2 6 hourly instantaneous analysis temperature and moisture fields at $5/8^\circ$ -by- $1/2^\circ$ resolution are bilinearly interpolated to the location of the radiosonde launch site in Güümar. The mean MERRA-2 temperature and dew point profile is also given in Fig. 9A as dashed lines and each of the 97 MERRA-2 profiles used here are shown in 9C.

2.3.2 Aerosol Extinction Profiles

Aerosol extinction profiles are not directly retrieved from MPL. Thus, to determine aerosol extinction vertical profiles from the NRB from MPL, a constraining AOD must be known. Thus, aerosol extinction profiles are only calculated when there are temporally coincident observations from MPL, AERONET, and radiosonde observations. Since AERONET observations are limited to daytime observations, data from all three observations is only available once per day at 1200 UTC (and any daytime special radiosonde launches). Thus, only AERONET and MPL observations within ± 10 minutes of the reported radiosonde observation are considered. Since MPL observations are provided at 60 s resolution, a possible 20 NRB observations can be considered for each radiosonde observation.

MPL observations with clouds must be removed from consideration to ensure only aerosol impacts are investigated. Cloud layers in each NRB profile are determined using a gradient threshold method similar to that described in Clothiaux et al. (1998). Specifically, compared to aerosol layers, clouds typically have more well defined edges. As such, measured lidar backscatter should spike near the cloud edge. Thus, the gradient in NRB with altitude is calculated and if that gradient is above a threshold determined via experimentation, the profile is assumed to contain cloud. Note, while

the co-located AERONET observations should be cloud-free, it is possible that the MPL observation contains transient cloud. For instance, Chew et al. (2011) showed thin cirrus cloud contamination in AERONET AOD retrievals. Thus, in this case, any residual cirrus in the AERONET observation will be screened using MPL NRB profiles. All verified cloud-free profiles are averaged. If there are less than 8 cloud-free profiles for a given radiosonde observation, the observation is rejected.

Extinction profiles can only be calculated for aerosol layers identified in the averaged NRB. These aerosol layers are identified as several consecutive vertical NRB observations with backscatter above that expected from scattering by air molecules plus some level of noise. The expected air molecule backscatter (referred to as Rayleigh or molecular backscatter) can be determined from the atmospheric temperature and pressure. Specifically, using the ideal gas law, the air molecule number density can be determined via:

$$N(z) = \frac{n}{V(z)} = \frac{P(z)}{R^* \cdot T(z)} \cdot A_v, \quad (2.2)$$

where $N(z)$ is the air molecule number concentration at altitude z in molecules-per-cubic-meter, n is the number of air molecules, $V(z)$ is the air volume at altitude z , R^* is the universal gas constant given as $8.314 (J \cdot K^{-1} \cdot mol^{-1})$, $P(z)$ is the air pressure at altitude z in Pascals, $T(z)$ is the air temperature at altitude z in Kelvin, and A_v is the Avogadro constant of $6.022 \times 10^{23} (mol^{-1})$. Finally, the molecular backscatter is given by Measures (1984):

$$\beta_{\pi}^R(\lambda, z) = N(z) \cdot \sigma_{\pi}^R(\lambda), \quad (2.3)$$

where $\beta_{\pi}^R(\lambda, z)$ is the molecular backscatter at wavelength λ and altitude z in units of per-meter, and $\sigma_{\pi}^R(\lambda)$ is the air extinction cross-section at wavelength λ . The air

extinction cross-section in meters-squared is also given by Measures (1984):

$$\sigma_{\pi}^R(\lambda) = \left[\frac{550 \text{ nm}}{\lambda(\text{nm})} \right] \times 5.45 \times 10^{-32} \text{ m}^2 \text{ sr}^{-1}. \quad (2.4)$$

Using the temperature and pressure from the radiosonde observations, the molecular backscatter can be determined and removed from the NRB. Finally, the noise estimate in the averaged NRB is determined by examining the standard deviation of clear-air NRB in the layer from 8 to 10 km (Campbell et al., 2008). The presence of several consecutive bins with NRB greater than the sum of the molecular backscatter and the noise estimate are considered aerosol layers. Note, it is possible that there are multiple aerosol layers detected in a single averaged profile.

Aerosol extinction profiles are retrieved from all cloud-free, averaged NRB profiles with at least one identified aerosol layer using the Fernald (1984) inversion. The Fernald (1984) inversion determines aerosol extinction iterative from a top-down approach. The first step in the inversion is to chose a first-guess extinction-to-backscatter ratio, also known as a lidar ratio. For this study, a value of 1.0 *sr* is used. Then, starting from the top of the aerosol layer, the layer aerosol backscatter coefficient at each layer is solved using the following iterative process from Fernald (1984) equation 6:

$$\beta_a(I-1) = \frac{X(I-1)A}{\frac{X(I)}{\beta_a(I)+\beta_m(I)} + S_a[(X(I) + X(I-1))A]\Delta_z} - \beta_m(I-1), \quad (2.5)$$

where $\beta_a(I)$, $\beta_a(I-1)$, $\beta_m(I)$, and $\beta_m(I-1)$ are the layer aerosol and molecular backscatter coefficient in per-meter at level I and $I-1$, respectively. $X(I-1)$ and $X(I)$ is the NRB at level I and $I-1$, respectively, S_a is the aerosol lidar ratio in

steradians, Δz is the layer depth in meters, and A is given by:

$$A = \exp\{[S_a - S_m][\beta_m(I - 1) + \beta_m(I)]\Delta Z\}, \quad (2.6)$$

where S_m is the molecular lidar ratio (given by $\frac{8\pi}{3}$ sr). Once the inversion has been performed over all layers, a new lidar ratio can be determined. The lidar ratio in steradians is given by:

$$S_a = \frac{\tau}{\sum \beta_a \cdot \Delta z}, \quad (2.7)$$

where τ is the unitless AOD measured by AERONET. The inversion process is iterated until the lidar ratio converges. If no convergence is found within 120 iterations, the profile is rejected. Similarly, if the lidar ratio is over 120, the profile is also rejected. Note, the lidar ratio is assumed constant with altitude. Finally, the aerosol extinction profile is found by multiplying the NRB within the aerosol layer with the molecular backscatter removed by the lidar ratio. Because NRB is given in 523 nm and the AOD from AERONET is at 550 nm, the resulting lidar ratio is a 550nm-extinction-to-523nm-backscatter ratio.

Once the aerosol extinction profile is found, the fine-mode and coarse-mode aerosol extinction profiles are determined by multiplying the aerosol extinction profile by the ratio of the fine-mode and coarse-mode AOD reported by AERONET. Each profile is then visually examined to remove unrealistic profiles (e.g., with cloud that passed the gradient-thresholding). The statistics of the 97 aerosol profiles passing quality checks are shown in Fig. 10. The mean AOD of the 97 cases was 0.30 with only 10 cases (10.9%) with AOD at or above 0.5. Overall, the aerosol profiles are dominated by coarse-mode particles as would be expected for wind-generated dust (Jacob, 1999), with only 6 (6.5%) of profiles exhibiting fine mode fractions at or above 0.5. Further,

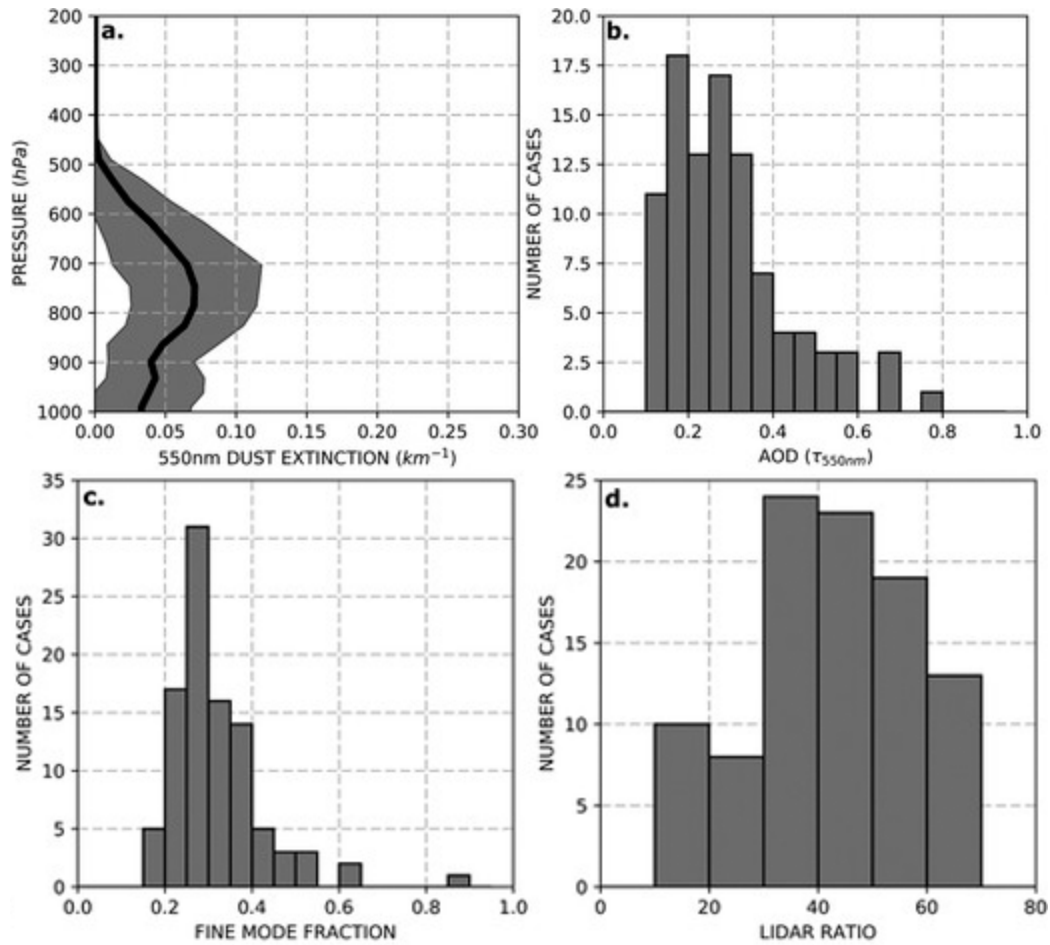


Figure 10: (a) Mean 550nm aerosol extinction profile with ± 1 standard deviation, and distribution of cases by (b) 550nm AOD, (c) fine mode fraction, and (d) 550nm-extinction-to-523nm-backscatter in steradians. Adapted from Marquis et al. (2021).

the majority of profiles exhibit lidar ratios between 30 and 60 sr, which is consistent, albeit not exclusively, with observations of dust (Müller et al., 2007).

2.3.3 Aerosol Number Profiles

RTTOV and the modified 1DVar system require aerosol to be provided in number concentration profiles. Using OPAC, the ratio of aerosol number to extinction coefficient was determined. Note, OPAC contains four mineral dust aerosol types: transported-mode, nucleating-mode, accumulating-mode, and coarse-mode. Since

the transported-mode aerosol is only used in the OPAC Antarctic aerosol type, it is assumed it represents aerosol that has been transported much further from its source region than Tenerife. As such, only the nucleating-mode, accumulating-mode, and coarse-mode mineral dust aerosol types are used here. Further, it is assumed all coarse-mode AOD is due to coarse-mode mineral dust, whereas fine-mode AOD is due to a mixture of nucleating- and accumulating-mode mineral dust. While other aerosols may also be present, for simplicity, only dust is assumed present. That said, given the lidar ratios, region, and season, the aerosol profiles should be at the very least dominated by dust. The number ratio between these two fine modes is set to that defined in the OPAC desert-type aerosol (269.5 cm^{-3} nucleating-mode to 30.5 cm^{-3} accumulating-mode; Hess et al., 1998). Using OPAC, the following 550 nm extinction to number concentration relationships were derived:

$$n_{nuc} = \beta_{ext,f} \times 14005.55 \text{ km cm}^{-3}, \quad (2.8)$$

$$n_{acc} = \beta_{ext,f} \times 320.41 \text{ km cm}^{-3}, \quad (2.9)$$

$$n_{coa} = \beta_{ext,c} \times 12.82 \text{ km cm}^{-3}, \quad (2.10)$$

where n_{nuc} , n_{acc} , and n_{coa} are the nucleating-mode, accumulating-mode, and coarse-mode number concentrations, respectively, and $\beta_{ext,f}$ and $\beta_{ext,c}$ are the fine-mode and coarse-mode aerosol extinction.

2.3.4 Synthetic Hyperspectral Observations

Due to uncertainties in observations associated with noise and representativeness, synthetic HIS observations are created such that the true atmospheric temperature and humidity profile is known. These observations are created for each of the 97

cases using the merged radiosonde-standard atmosphere temperature and moisture, an ozone profile from the standard tropical atmosphere, and the derived aerosol number concentration profile using RTTOV. RTTOV is run twice, once with no aerosol number concentrations, and once with the observed aerosol number concentration. The difference between the two provide an estimate of aerosol-induced bias on HIS radiances. Note, RTTOV is run using the same configuration as is used during the forward model calls in the 1DVar system for consistency.

2.3.5 Determining Analysis Bias

To determine analysis bias, instead of taking the difference between the dust-biased analysis temperature and humidity and the true temperature and humidity used as background and used in created the synthetic observations, the system is run a second time with aerosol number concentrations provided to the forward RTM calls. By ensuring that the true profile is retrieved when aerosol number concentration is provided to the 1DVar system, it can be ensured that the difference between the two analyses is only aerosol-induced and not due to other sources (e.g., truncation).

2.3.6 MERRA-2 Experiment

In an operational setting, the background atmosphere is from model forecast and thus, rarely truth, but some deviation about truth. As such, a second experiment for each of the 97 cases in which the merged radiosonde - standard atmospheric profiles used to create the synthetic observations are not used as background, and instead the bilinearly interpolated MERRA-2 temperature and humidity profiles are used. By examining the impact of both including and not including aerosol number concentrations, analysis uncertainties in an operational setting can be examined.

2.4 Results

2.4.1 Dust Induced Radiance Biases

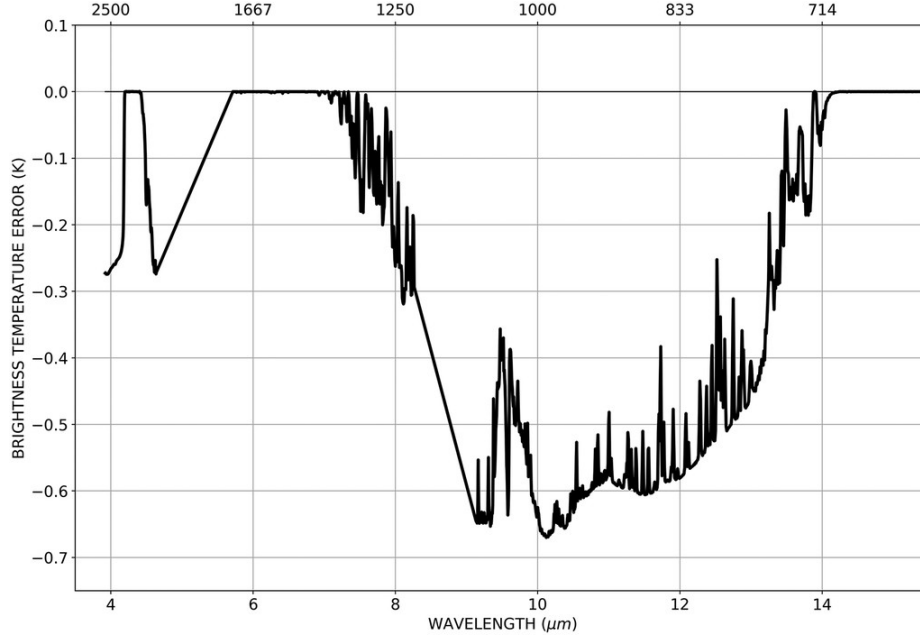


Figure 11: Mean brightness temperature bias as a function of wavelength for the 97 dust cases. Adapted from Marquis et al. (2021).

The mean brightness temperature bias imparted by the 97 dust profiles is shown in Fig. 11. Brightness temperature bias peaks at 0.65 K at a wavelength of 10 μm , with bias evident from 7 to 14 μm . Additional bias exists near 4 and 4.5 μm . Wavelengths bands from 4.1 to 4.5 μm , 5.5 to 7 μm , and those greater than 14 μm experience no dust-induced bias. Note, the straight lines at 4.5 to 5.5 μm and from 8.5 to 9 μm are due to spectral gaps in the CrIS bands. The spectral shape of these biases are consistent with the impacts shown in Pierangelo et al. (2004), including both experiencing peak bias near 10 μm . That said, overall brightness temperature bias seems lower, even when the lower AOD is considered. For example, Pierangelo et al. (2004) found a peak brightness temperature bias of 5 K for an AOD of 0.75.

This is over 7 times larger than what is found here, despite the mean AOD here only being 60% lower.

There are several possible reasons for the difference in brightness temperature impacts seen here versus those reported by Pierangelo et al. (2004). Firstly, Pierangelo et al. (2004) assume that all dust aerosols are located within a single model layer, whereas here, the observed profiles exhibit dust diffused through throughout the lowest 5 to 6 km. Next, they used a static, climatological meteorological profile, where here, observations that are physically coupled with the dust aerosol profiles are used. Pierangelo et al. (2004) also focuses on AIRS, whereas CrIS is the focus here. While differences due to the use of the different sensors should be limited, there are different spectral sampling characteristics (Tobin et al., 2013). That said, it is important to note that the spectral shape of the bias is consistent. Next, Pierangelo et al. (2004) uses the Automatized Atmospheric Absorption Atlas (4A; Scott and Chedin, 1981) whereas RTTOV is used for this study, possibly resulting in forward modeling differences. Finally, the mean bias in brightness temperature for 97 profiles of varying AOD is shown here instead of a single profile as reported by Pierangelo et al. (2004). As shown in Fig. 10, the shape of the AOD distribution of those 97 cases is biased towards lower AODs. As such, the mean bias may not be representative of an AOD of 0.3, but something smaller. This will be examined in section 2.4.4.

2.4.2 Impact on Analyzed Temperature

In section 2.4.1, the brightness temperature biases expected in contaminated HIS observations is shown. Given the expected biases, it was shown that even observations contaminated by relatively massive aerosol loading can be assimilated given current screening methods. Thus, the impacts of assimilating these contaminated radiances on analyzed temperature and moisture profiles need to be examined. As mentioned

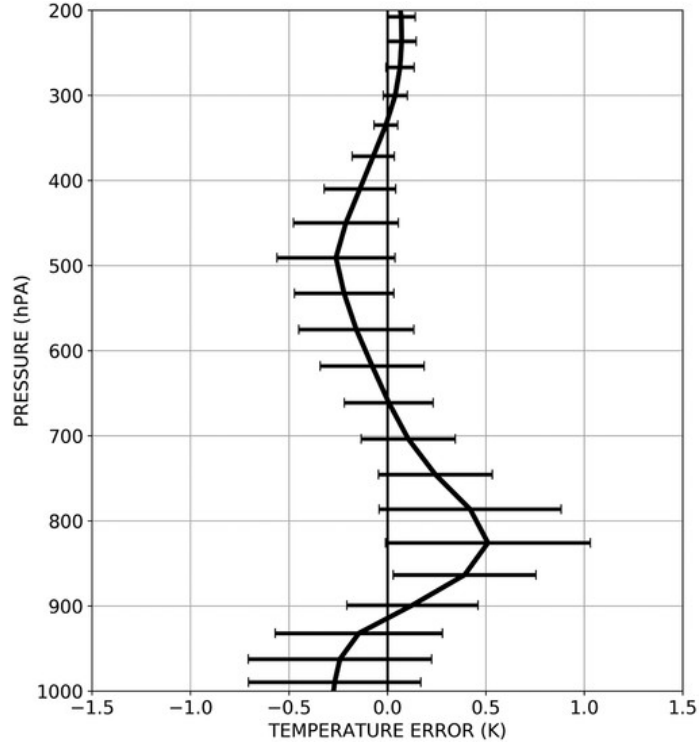


Figure 12: Vertical profile of the mean (± 1 standard deviation indicated by horizontal bounds) of the analyzed temperature bias for the 97 dust cases. Adapted from Marquis et al. (2021).

in section 2.3.5, analysis bias is defined as the difference between the analysis when a contaminated observation is assimilated and the analysis when a contaminated observation is assimilated but aerosol properties are provided to the forward and gradient RTMs. That said, the difference between the analysis when aerosol properties are provided to the system and the true atmosphere (i.e., that used to create the synthetic observations) is extremely small (10^{-3} K, due to truncation in providing observed radiances via ASCII). As such, the analysis bias as defined here is virtually equal to the difference between the contaminated observation analysis and the true atmosphere. That said, the fact the system is able to "retrieve" a true atmosphere when provided with aerosol properties points to a possible method of decoupling the aerosol contribution during assimilation.

The mean and standard deviation of the analyzed temperature bias as a function of altitude for the 97 profiles is shown in Fig. 12. Temperature biases are evident from the surface to at least 300 hPa - a level approximately 200 hPa above the top of the highest dust. While seemingly counterintuitive, this is easily explained when the temperature Jacobians are examined. Specifically, channels that may have sensitivity peaks at higher altitudes will still sense lower features. That said, the maximum mean temperature bias of 0.5 K occurs at approximately 825 hPa, near the base of the maximum in the mean aerosol layer. From the surface to approximately 750 hPa, the standard deviation of the analysis bias is approximately 0.5 K, while above 750 hPa the standard deviation is around 0.25 K. Given typical NAVGEM background temperature errors of 0.4 K, the mean biases seen here are of great concern. This is especially the case when it is considered that approximately 16% of all assimilated observations may be contaminated at AODs above the mean of 0.3 here (e.g., Fig. 4 and related discussion).

2.4.3 Impact on Analyzed Dewpoint Temperature

The dew point temperature is the temperature the air must be cooled to at a constant pressure for it to become saturated or for the relative humidity to equal 100% (Wallace and Hobbs, 2006). The dew point temperature is thus related to the water vapor mass density via the Clausius - Clapeyron equation and the ideal gas law. NAVGEM background water vapor error is about 20%. If this 20% value is assumed constant throughout the profile, the expected background dew point error is near 3 K in the lower troposphere, and below 2 K above 500 hPa.

The mean and standard deviation of the analyzed dew point temperature bias as a function of altitude for the 97 cases is shown in Fig. 13. Three peaks in dew point bias are evident: a 1 K peak at 950 hPa, a 0.8 K peak at 700 hPa, and a -0.8

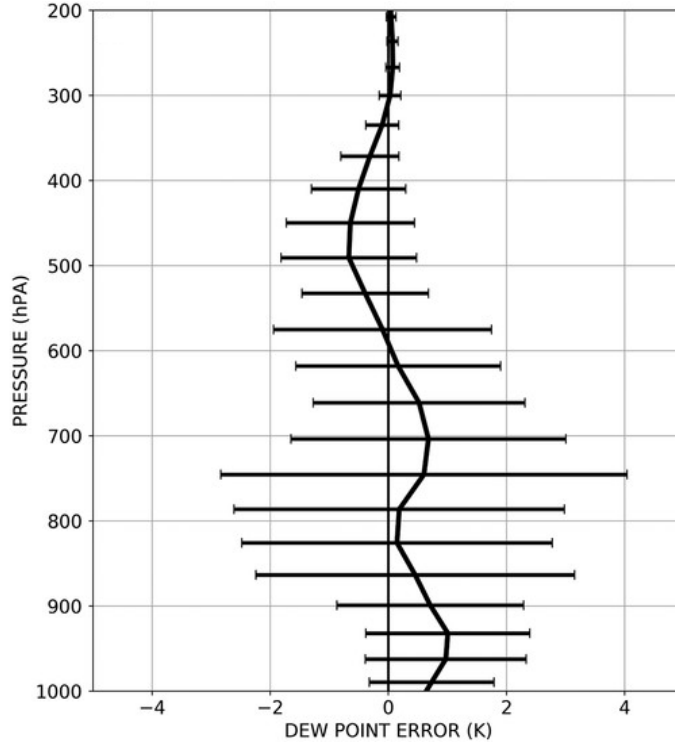


Figure 13: Vertical profile of the mean (± 1 standard deviation indicated by horizontal bounds) of the analyzed dew point temperature bias for the 97 dust cases. Adapted from Marquis et al. (2021).

K peak at 500 hPa. The middle peak at 700 hPa is associated with a very large standard deviation over 3 K. As such, while the mean bias may be lower than the expected background error, the standard deviation indicates that much larger biases are present in individual cases. It is important to note that the peak at 700 hPa is near the peak of aerosol loading shown in Fig. 10. Additionally, the 500 hPa bias peak is at the same altitude as the top of the aerosol plume. As with the temperature bias, dew point bias also extends above the aerosol layer.

2.4.4 Bias at Other Aerosol Loadings

As mentioned in section 2.4.1, the distribution of aerosol cases is biased towards lower AOD cases. Thus, in an attempt to better estimate the brightness temperature biases

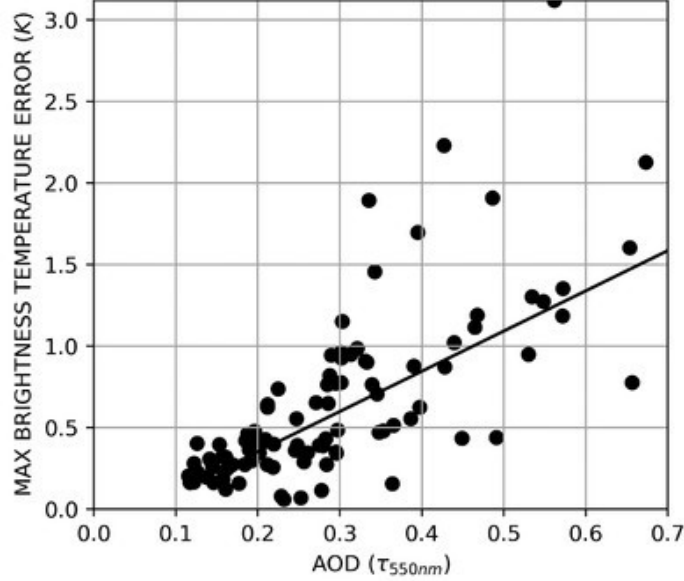


Figure 14: Scatter plot of the maximum brightness temperature bias as a function of column AOD for each of the 97 cases along with the best fit linear regression line. Adapted from Marquis et al. (2021).

as a function of column AOD, a scatter plot of the maximum brightness temperature bias for each profile is shown as a function of column AOD in Fig. 14. Linear regression is performed using the Theil-Sen method (Theil, 1950a,c,b). The Theil-Sen method determines the slope using the median value of all the slopes of every possible pair of points. As such, this method is less susceptible to outliers. Here, a slope of 2.608 K per unit AOD is found with a correlation of 0.756 ($BT_{bias} = 2.608K \times AOD_{550nm} - 0.141K$). Using this relationship, the maximum brightness temperature bias for an AOD of 0.75 should be near 1.8 K, still 3.2 K below the value reported by Pierangelo et al. (2004). This difference is likely due to the points mentioned above, specifically the use of relatively vertically diffuse aerosol layers here and different temperature and humidity profiles. These lower biases may actually result in more contamination. For example, as explained in section 1.3, the NAVDAS system removes observations with background innovations above 3 K or those with

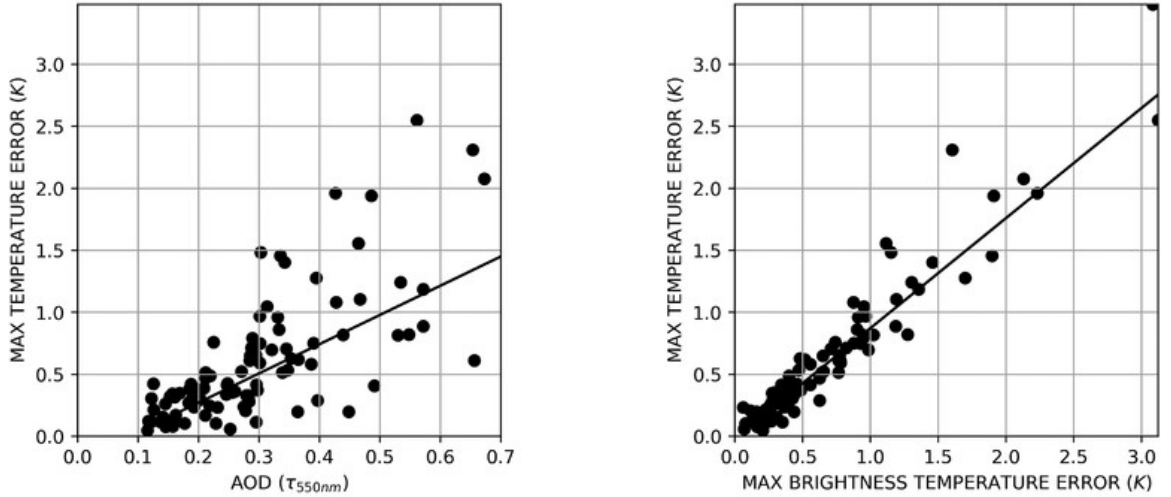


Figure 15: Scatter plot of the maximum tropospheric temperature bias as a function of AOD and brightness temperature bias for each of the 97 dust cases. Adapted from Marquis et al. (2021).

discontinuities over 0.5 K. Given the derived relationship, even aerosol layers with AOD greater than 1.0 can pass aerosol and cloud screening.

As is performed for brightness temperature bias, the maximum tropospheric analysis temperature bias at larger aerosol loadings (and larger brightness temperature biases) is examined by performing Theil-Sen linear regression as shown in Fig. 15. As with brightness temperature and AOD, there is a relatively high correlation between the maximum temperature bias and the AOD (r value of 0.759). Using linear regression the AOD at which the temperature bias exceeds the typical background error of 0.4 K is approximately 0.25 ($\Delta T_{max} = 2.357K \times AOD_{550} - 0.2K$). Further, given the conclusion that aerosol layers with AOD greater than 1.0 can pass screening, large analysis biases over 2.0 K likely exist.

Given that minimization of the cost function directly incorporates brightness temperature and not AOD, it is unsurprising that maximum troposphere temperature bias is correlated higher with maximum brightness temperature bias (r value of 0.957). Ad-

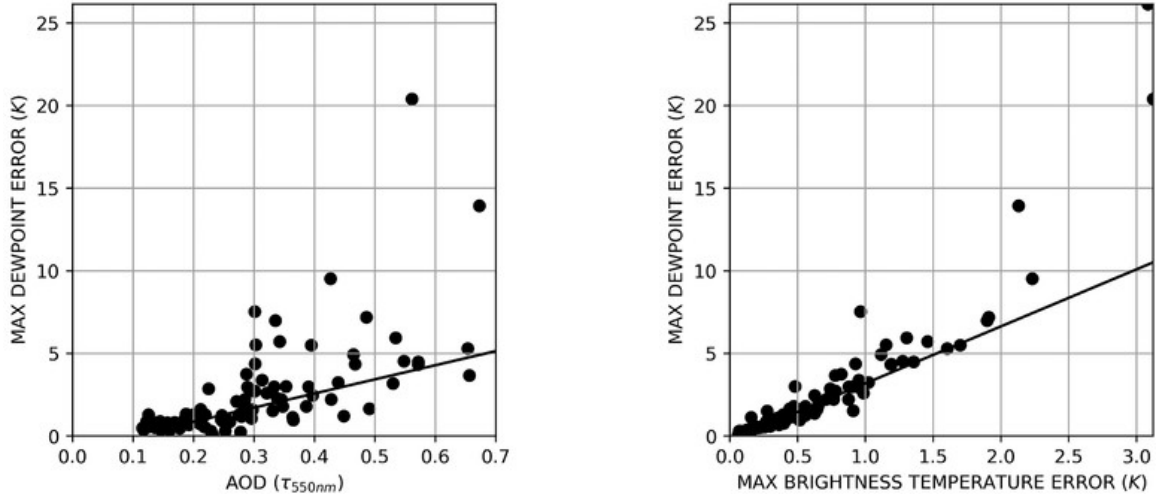


Figure 16: Scatter plot of the maximum tropospheric dew point temperature bias as a function of AOD and brightness temperature bias for each of the 97 dust cases. Adapted from Marquis et al. (2021).

ditionally, it is found that a 1 K bias in brightness temperature can induce a 1 K temperature analysis bias ($\Delta T_{max} = 0.887K \times \Delta BT - 0.015K$). Concerningly, since the NAVDAS innovation threshold is approximately 3 K, aerosol induced temperature biases may be as large as 3 K.

Finally, the same regression is performed for the maximum dew point bias as a function of AOD and brightness temperature bias in Fig. 16. As with brightness temperature and temperature, there is a relatively high correlation between the maximum dew point temperature bias and the AOD (r value of 0.688). Using linear regression the AOD at which the temperature bias exceeds the typical background error of 2-3 K is approximately 0.33 - 0.45 ($\Delta T_{Dmax} = 8.554K \times AOD_{550} - 0.848K$). Note, while these AODs are larger than that for the temperature background error, this is due to higher moisture uncertainties. That said, since observations contaminated by AOD greater than 1.0 can pass screening, large analysis biases over 8.0 K likely exist.

As is the case for temperature bias, the maximum tropospheric dew point temperature bias is correlated higher with maximum brightness temperature bias (r value of 0.918). Additionally, while a 1 K bias in brightness temperature can induce a 1 K temperature analysis bias, it may cause a 3 - 4 K bias in dew point temperature ($\Delta T_{Bmax} = 3.452K \times \Delta BT - 0.263K$). Concerningly, since the NAVDAS innovation threshold is approximately 3 K, aerosol induced dew point temperature biases may be as larger than 10 K.

2.4.5 Impact With Imperfect Background Atmosphere

The experiment thus far has been an attempt to fully isolate the impact of aerosol. That said, to ensure isolation, the background atmosphere was set to the true atmosphere. It is highly unlikely that the background atmosphere will be equal to truth in an operational setting since it is derived from a forecast. In reality, the background usually represents some deviation about the true atmosphere. To better understand impacts in a more operational setting, the bilinearly interpolated MERRA-2 atmospheres are used for background here. As before, the system is run twice: once with aerosol properties provided, once without aerosol.

The mean difference between the analyzed temperature and dew point temperature and the true atmosphere for the 97 dust cases when MERRA-2 reanalysis is used as background is shown in Fig. 17. The background MERRA-2 profile is, on average, too cold below 800 hPa and too warm at higher altitudes. Additionally, the MERRA-2 profile exhibits large positive moisture biases of 1 - 6 K, generally increasing with altitude. Both temperature and dew point temperature errors are generally decreased even when aerosol properties are not provided. That said, in the portions of the atmosphere with the heaviest aerosol loading (surface to 700 hPa), providing aerosol properties typically results in an analysis with less bias. Given the expected

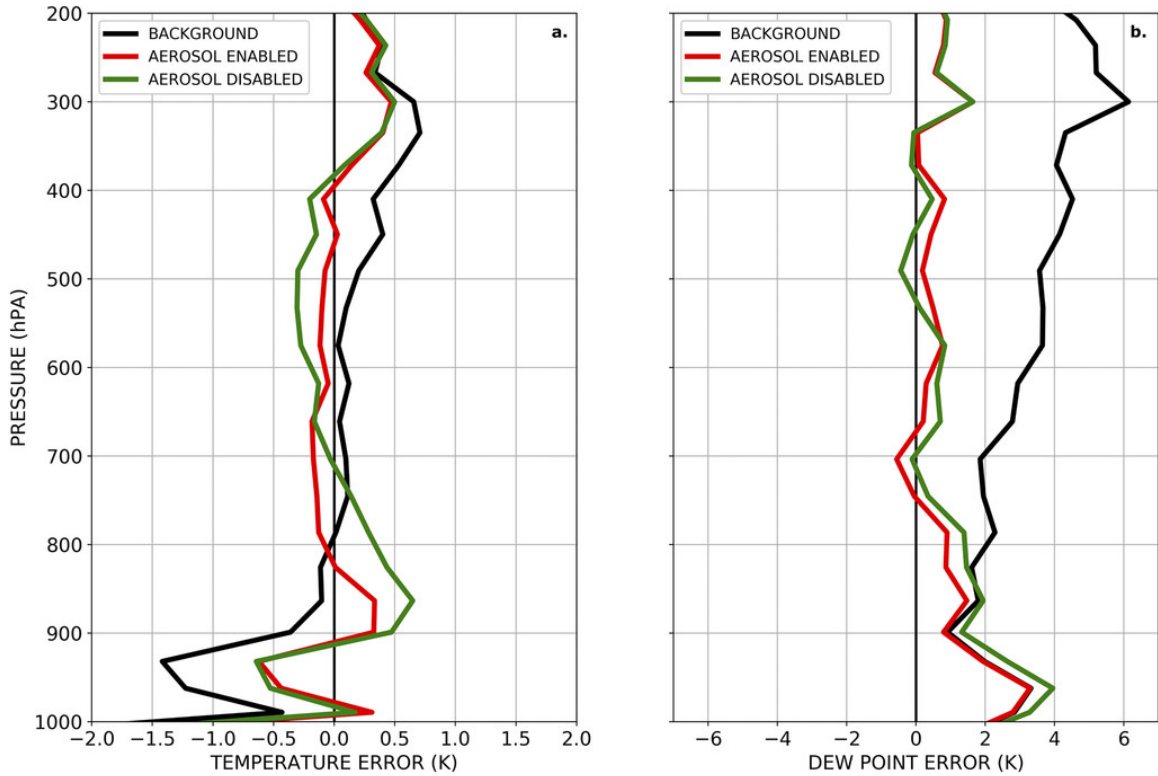


Figure 17: Temperature and dew point error after assimilation with aerosol optical properties included (red) and not included (green) compared to the background atmosphere from MERRA-2 (black) for the 97 dust cases. Adapted from Marquis et al. (2021).

temperature background error of 0.4 K, when aerosol is provided, the analyzed temperature is nearly always below that threshold whereas the "assumed clear-sky" still exhibits biases up to 0.6 K at 850 hPa. However, for dew point, while providing aerosol properties results in a better analysis, both analyses are below the expected uncertainty of 2 - 3 K.

2.5 Discussion

Aerosols contaminate assimilated HIS observations at very high rates. While these aerosols result in only slight impacts on observed brightness temperatures, the im-

pacts on analyzed temperature and dew point temperature are likely above expected uncertainties. In fact, given the relatively low impact on brightness temperature, contaminated observations are highly likely to pass screening measures. As such, model atmospheres likely exhibit aerosol-induced errors, particularly in regions where IR-active aerosols are likely to be present.

Since dust aerosols are often present at relatively high loadings in regions where tropical cyclones form, the presence of any aerosol-induced bias may be causing an additional complications in modeling tropical cyclogenesis and forecasts based upon these model predictions. Specifically, these regions are over open oceans far from in-situ observations, putting further dependence on assimilated HIS observations. That said, the experiment using MERRA-2 is encouraging - showing even assimilating aerosol biased radiances may be better than no observations at all. Possibly more importantly, however, it shows that it is possible to further increase analysis accuracy by providing aerosol properties either from observations for aerosol prediction models to decouple the aerosol impacts. Given the results here, forecast impacts due to assimilating aerosol biased radiances should be considered in future efforts.

CHAPTER 3

CLOUD INDUCED ANALYSIS BIAS

3.1 Introduction

3.1.1 Rationale

Unlike aerosols, clouds are always active in the IR. As such, any contaminating cloud will have a biasing impact on measured HIS radiances. Thankfully, given the contamination frequencies in Figs. 4 and 5, it seems clouds, particularly cirrus clouds, are less likely to contaminate assimilated observations. Presumably, this better screening may be due to larger impacts on observed radiances. That said, unlike aerosols like dust, clouds are both substantially more global and more transient, such that centers cannot just ignore observations in certain regions. Further, cirrus clouds in particular are difficult to observe while still presenting extremely high thermal contrast with the lower levels of the atmosphere. In this chapter, an experiment is conducted to estimate analysis error due to assimilating cirrus biased HIS radiances.

3.1.2 Background

Cirrus clouds present a constant concern for passive satellite observations. These clouds are completely composed of ice and thus, form at high altitudes where temperatures are below -30°C . In the midlatitudes, this is generally above at least 5 km in altitude (Ahrens and Henson, 2019), but can be much higher (e.g., Campbell et al., 2018). Cirrus clouds usually form either via deep convection or the local ascent of air in the upper portions of the troposphere. Specifically, atmospheric waves can result

in ascent of this upper tropospheric air, cooling the air to supersaturation with respect to ice and leading to cirrus formation (Virts et al., 2010). Additionally, anvils and outflow associated with deep convection (i.e., thunderstorms) will cause cirrus clouds. Due the possibility of mixed phase clouds at temperatures above -40°C , for this study, cirrus clouds are limited to those with temperatures below -40°C .

Half of all cirrus clouds are optically thin - exhibiting visible optical depths below 0.30 (Sassen and Cho, 1992). Mace et al. (2009) found that cirrus clouds are present over 40-60% of the Earth on average. While aerosols are present over the entire globe, they often exist at optical depths too small to cause noticeable impacts and larger loading is more limited to source regions and areas downstream. Conversely, cirrus clouds can, and do, form anywhere, while also exhibiting large variability. The frequency of optically thin cirrus (OTC) as retrieved from the CALIOP level-2 5 km cloud layer product is shown in Fig. 18. Frequency defined as number of observations containing at least one cirrus layer with visible COD below 0.3 to the number of total observations, with observations from both daytime and nighttime considered. Cirrus clouds are defined as any cloud layer with cloud top temperature below 233 K with cloud top temperature colder than cloud base temperature to limit stratospheric clouds. While the entire globe experiences OTC, areas near the intertropical convergence zone (ITCZ) and latitudes poleward of $\pm 60^{\circ}$ experience more than other regions. For example, Southeast Asia exhibits OTC frequencies approaching 60%. Note, however, that this does not mean the other 40% of days are clear of all cloud as other ice or liquid water clouds may be present. In fact, given that Marquis et al. (2017) found up to 70% of IR SST retrievals from this region have residual OTC as reported by the level 2 CALIOP 5 km cloud layer product, it is highly likely that scenes without other cloud more often than not contain OTC.

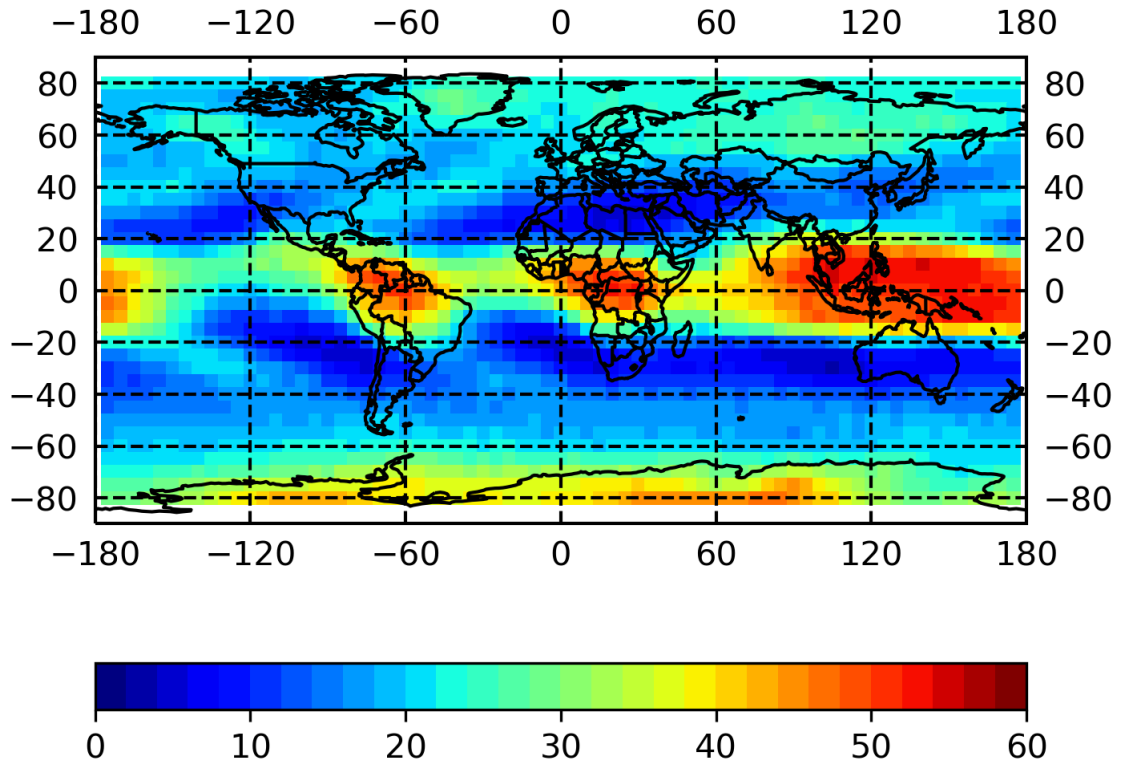


Figure 18: Frequency of optically thin cirrus clouds (visible optical depth below 0.30) from CALIOP based on 2006 - 2018.

Further, as with the regions impacted by dust, this region is of particular concern for NWP efforts in tropical cyclone forecasting.

On average, approximately 30% of the world’s tropical cyclones form in the Western North Pacific alone (Gray, 1975). As expected, uncertainties in model initial conditions lead to high uncertainties in tropical cyclone predictions of track and, more so, intensity. Specifically, Wang et al. (2020) found accuracy in initial humidity, and to a lesser extent, temperature at lower levels of the atmosphere were key factors in the accuracy of tropical cyclone forecasts. And while this region does contain more radiosonde observations than those with dust concerns (e.g., Fig. 8), models are still heavily reliant on IR radiance assimilation. Tropical cyclones have extensive impacts

on both economy and life. For example, Kunze (2021) showed direct worldwide impacts of over 16.7 billion USD per year on average due to the direct impacts of tropical cyclones with other estimates over 50 billion USD. Several recent years have tropical cyclone impacts at well over 100 billion USD in damage. Further, tropical cyclones are responsible for over 1,000 fatalities per year. As such, minimizing, or at the very least, recognizing uncertainties in forecasts due to analysis errors from sources such as cirrus cloud contamination is extremely important.

Simulating cirrus clouds is non-trivial however. To simulate the radiative effects of clouds, the microphysical properties often need to be known. As such, observations of the ice properties within cirrus clouds must be sufficiently numerous to understand the microphysical properties and variability. Obtaining observations in cirrus clouds can be extremely difficult and is often inherently biased. For instance, because cirrus clouds are often present at high altitudes, in-situ observations may be difficult for traditional observing aircraft. For instance, cirrus may be present to near 20 km in altitude (Marquis et al., 2017), whereas typical commercial and many (though not all) research aircraft are limited to altitudes below 13 km. Further, because aircraft must be aware of the presence of a cloud to measure its properties, optically thin cirrus may not be identified and, thus, not sampled. For instance, Heymsfield et al. (2014) examined in-situ observations of ice crystals collected within clouds. Their analysis shows substantially more observations at higher temperatures and low altitudes than those collected at high altitudes. Because warmer cirrus clouds are more likely to be formed via deep convection than higher clouds, inherent sampling biases exist where observations may not be representative of the cirrus forming in the upper troposphere. Finally, observations themselves are historically imperfect due to observational system issues such as ice crystals shattering on the measurement probes

themselves (Heymsfield et al., 2014), though new developments limit these impacts in newer campaigns (REF).

In this chapter, the analysis temperature and moisture error induced via assimilating cirrus biased radiances is estimated using a state of the art ice crystal optical model. In section 3.2, the models and datasets used are discussed. In section 3.3, the methodology for determining bias is outlined. The results are described in section 3.4 and the importance of these results and future work is explored in section 3.5.

3.2 Datasets & Models

3.2.1 RTTOV

Similar to the study presented in Ch. 2, RTTOV is used for radiative transfer. Here, RTTOV version 12.3 is used. Compared to version 11.2 used in Chapter 2, version 12.3 has several updates. For example, new subroutines for input and output array allocation are included, the ability to provide moisture as either number concentration or mixing ratio, the ability to provide aerosols in mass mixing ratio, and new ice optical parameterizations. While RTTOV version 13.0 was available at the time of the experiments, the latest version of the 1DVar assimilation system used here (explained in section 3.2.2) is only set up to be compiled with RTTOV v11 or RTTOV v12. The RTTOV input and output variables here are identical to RTTOV v11, unless mentioned above.

3.2.2 1DVAR & Error Variances

Again, as in Ch. 2, a modified version of the EUMETSAT NWP SAF 1DVar system built with RTTOV v12.3 is used. Whereas previously, 1DVar version 1.1 was used, here 1DVar version 1.2 is used. Version 1.2 is identical to version 1.1 except a satellite

observation simulator and the ability to retrieve surface emissivity have been added. The surface emissivity retrieval is not implemented here. The satellite observation simulator simply uses the coupled RTTOV to simulate observations. That said, the simulator has an option to include expected instrument noise. This is achieved via the following relationship:

$$I_\lambda = I_{\lambda,0} + [R_\lambda \cdot \mathbf{R}(\mu, \sigma)], \quad (3.1)$$

where I_λ is the simulated radiance with noise at wavelength λ , $I_{\lambda,0}$ is the simulated radiance from RTTOV at wavelength λ , R_λ is the error variance for wavelength λ , and $\mathbf{R}(\mu, \sigma)$ is a random number from a normal distribution with mean of μ and a standard deviation of σ . Here, since observations are assumed unbiased, the mean is set to 0.0. A standard deviation of 1.0 K is used for observations and error variances defined using brightness temperature.

As before, the 1DVar system has been modified, albeit to allow ice clouds in the forward and gradient simulations as opposed to aerosol as before. The RTTOV v12.3 allows clouds to be provided in a variety of ways with varying simplicity. The most simple method to provide cloud is via a cloud fraction and cloud top pressure. Radiances in scenes with clouds can also be simulated using several methods such as the Discrete Ordinates Method (DOM). The DOM approximately solves the radiative transfer equation and is implemented here with 8 radiation streams. When using DOM, several different cloud options can be used. For ice cloud specifically, three optical parameterizations are available - those defined in Baum et al. (2011), Vidot et al. (2015), and an updated version of the Vidot et al. (2015) model. Here, custom cloud optical properties for each wavelength at each vertical background level are

provided to the 1DVar system. These optical properties are described in detail in section 3.2.5.

Finally, as in Chapter 2, the sample 54-level background error covariance matrix provided in the 1DVar source code is used. Additionally, the error variances defined for the CrIS instrument aboard the Suomi-NPP satellite included in the 1DVar source code is used.

3.2.3 Meteorological Profile

In Ch. 2, temperature and moisture from observations were used. This ensured that observations with dust were realistic. However, it limited the variability in aerosol scenes. To greater estimate analysis errors for a wide variety of cloud types, observations are not used. Instead, the standard tropical atmosphere from McClatchey et al. (1972) is used. The temperature, humidity, and ozone profiles are interpolated to the 54 levels used in the background error covariance matrix. For vertical interpolation, the interpolation method discussed in Section 3.2.3.1 in Askelson (2002) is used. The interpolated temperature and dew point profile is shown in Fig. 19. Also in Fig. 19 are two dashed lines indicating the first model altitude with temperature below 233 K (at a pressure of 236 hPa) and the top of the troposphere (at a pressure of 97 K). The first level is approximately the temperature at which water droplets will freeze homogeneously. As such, all clouds above this level are likely to be ice clouds.

3.2.4 Simulated Cirrus Clouds

As alluded to above, by using a standard atmosphere for all cases, analysis biases can be estimated for a variety of clouds. Specifically, cirrus clouds of varying altitude and optical depth are superimposed upon the standard tropical atmosphere described in section 3.2.3. Clouds are created for each vertical layer between the first atmospheric

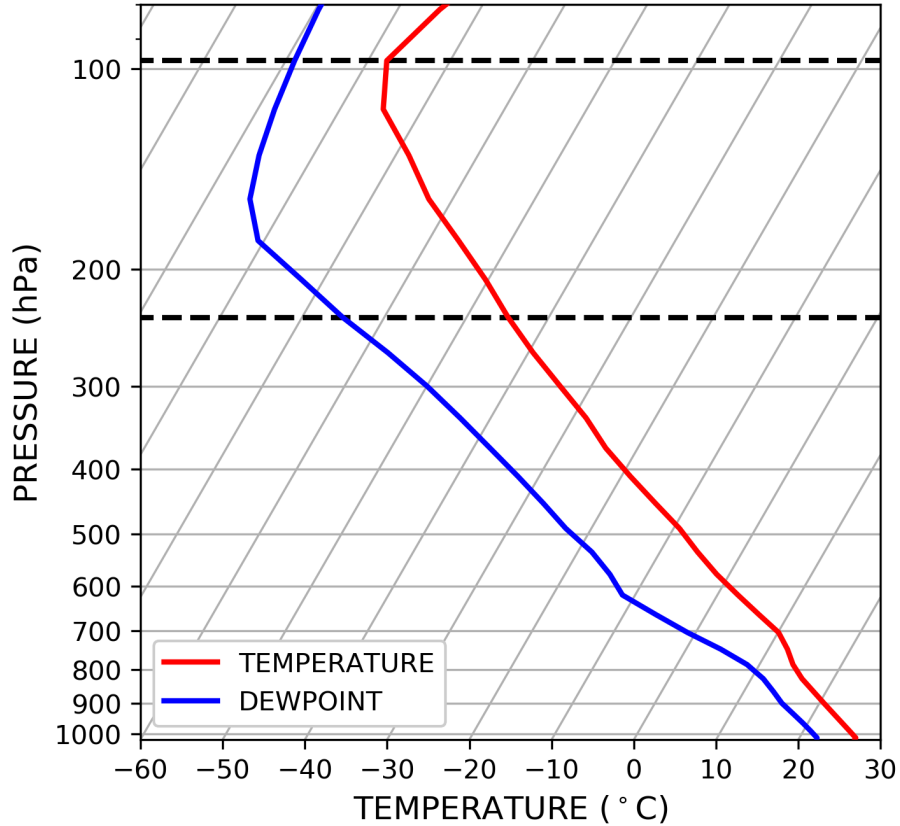


Figure 19: Temperature and humidity profiles for the McClatchey et al. (1972) tropical standard atmosphere interpolated to the study grid. Indicated by horizontal dashed lines are the first altitude below 233 K (at 236 hPa) and the tropopause (at 97 hPa) between which cirrus clouds are simulated.

layer with a temperature below 233 K and the top of the troposphere (indicated by dashed lines in Fig. 19), corresponding to 7 different vertical layers. Each cloud is limited to a single vertical layer of homogeneous cloud properties. Because the vertical layers stretch with altitude, the physical depth of the simulated clouds vary slightly. For instance, for the lowest cloud at 236 hPa, the cloud is approximately 854 m deep whereas the highest cloud at 97.2 hPa is 1021 m deep. While the physical depth may vary slightly by altitude, cloud properties are constrained by optical depth. Specifically, 43 different optical depths are defined, varying from 0.01 to 0.30 in 0.01

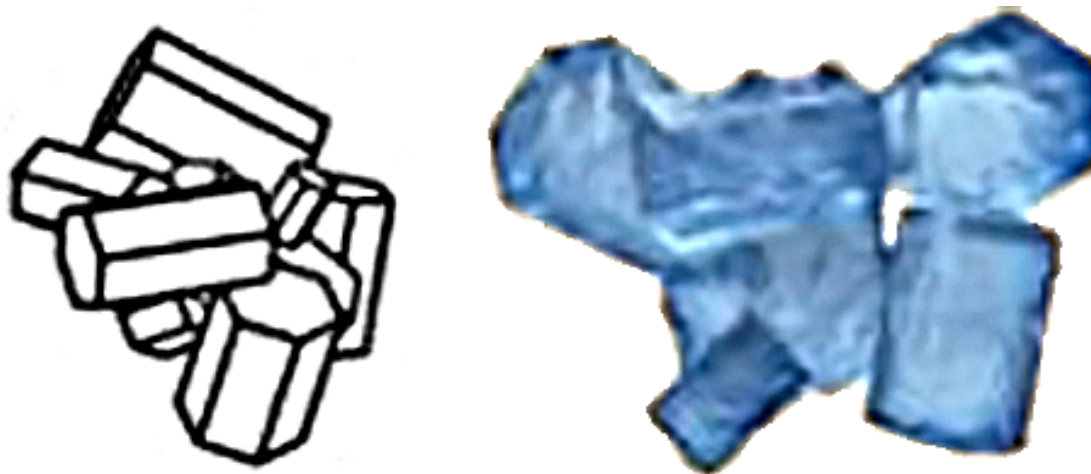


Figure 20: Impression of the 8-column aggregated ice crystals. Adapted from Yang et al. (2013) Fig. 3 and Platnick et al. (2017) Fig. 3.

increments and 0.35 to 1.0 in 0.05 increments. Each cloud is simulated with no other cloud in the vertical profile. The optical properties of the clouds are described in section 3.2.5.

3.2.5 8-Column Aggregate Ice

Clouds are provided to RTTOV for radiance and Jacobian calculations via layer absorption optical depth, scattering optical depth, and Legendre expansion coefficients of the phase function for each vertical layer and each assimilated channel. To provide these optical properties, an optical parameterization must be used. While a plethora are available, here, an optical model described in Yang et al. (2013) and Bi and Yang (2017) is used.

The Yang et al. (2013) and Bi and Yang (2017) ice optical model presents the current most state-of-the-art optical parameterization. Specifically, the ice crystals composed of aggregates of 8 solid-column ice crystals with severely roughened surfaces used here are (shown in Fig. 20). This optical model is hereafter referred to as

8CASM. This ice crystal model has been used for satellite-based retrievals of ice cloud properties resulting in an increase in consistency between retrieval techniques and observations. For example, cloud optical depth retrievals from MODIS Collection 5 cloud property retrievals showed a factor of two high bias as compared to retrievals using Version 3 CALIOP data. Further, MODIS COD retrievals based in the visible exhibited high biases compared to MODIS COD retrievals based in the IR. With the implementation of 8CASM in the MODIS Collection 6 cloud property retrieval, these biases have been removed. As such, 8CASM results in consistent results between infrared and visible, and between passive and active retrievals (Holz et al., 2016).

The model was provided by Ping Yang's research group at Texas A&M University. Optical properties of extinction efficiency, single-scattering albedo, asymmetry factor, and phase functions are given for wavelengths from 0.2 to 100 μm for ice crystal radii of 0.2 μm to 1 mm. For each ice crystal radius, geometric properties of maximum dimension, volume, and projected area are provided. All data was provided in ASCII, which was aggregated and stored in Network Common Data Form (NetCDF) version 4 for further use and storage considerations.

3.3 Methodology

3.3.1 Ice Optical Properties

3.3.1.1 Effective Optical Properties Derivation

As mentioned above, optical properties of absorption optical depth, scattering optical depth, and Legendre expansion coefficients of the phase function are provided to the 1DVar system and RTTOV. Since clouds are not composed of ice crystals of a single size, but a distribution of sizes, bulk optical properties must be calculated. Following the promising results of the MODIS Collection 6 algorithm, similar methodology is

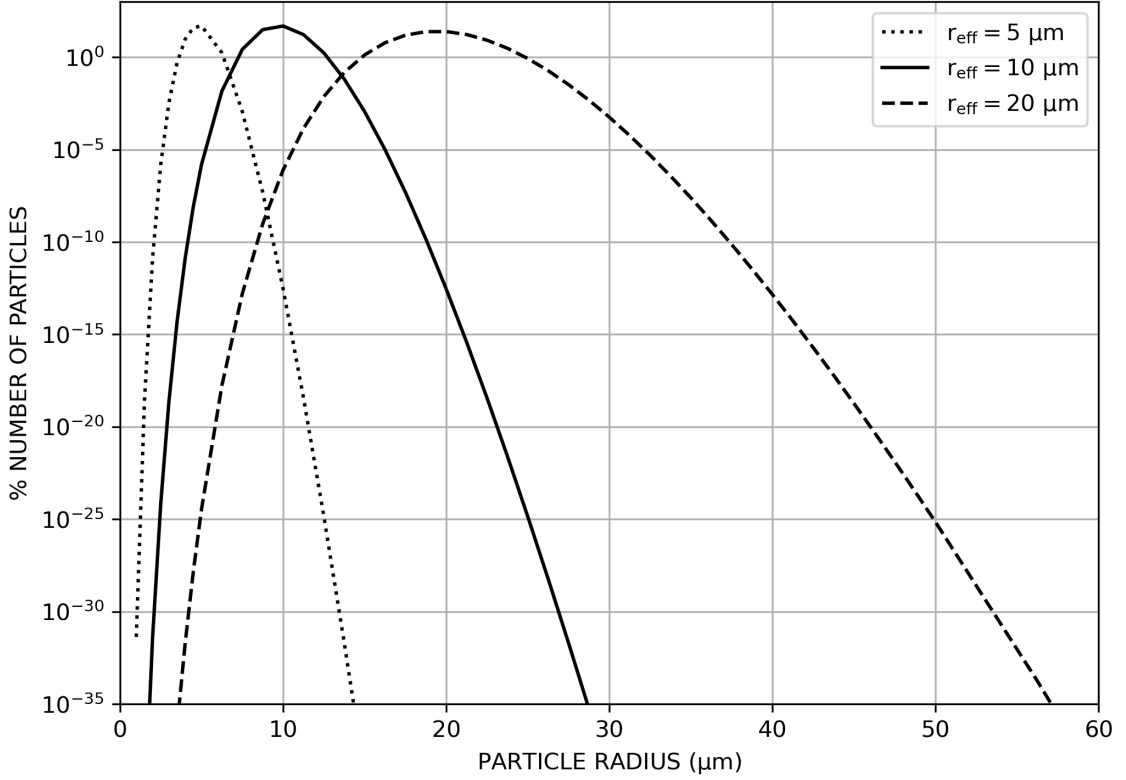


Figure 21: Relative percentage of particles of different sizes for effective radii of (dotted) 5.0, (solid) 10.0, and (dashed) 20 μm .

applied. Specifically, MODIS Collection 6 gamma size distribution is applied (Platnick et al., 2017):

$$n(r_e) = r_e^{\frac{1-3\sigma^2}{\sigma^2}} \cdot \exp\left(\frac{-1 \cdot r_e}{r_{eff} \cdot \sigma^2}\right), \quad (3.2)$$

where $n(r_e)$ is the number of particles with radius r_e , σ^2 is the variance of the gamma distribution (assumed to be 0.10 consistent with Platnick et al. 2017), and r_{eff} is the effective radius of the size distribution. The shape of the size distribution is shown for three different effective radii are shown in Fig. 21. Note, for very small effective radii, the particle size distribution is truncated for the tiniest particle sizes. Also note, the width of the distribution widens as the effective radius increases.

For consistency with Platnick et al. (2017), the radii used in Eq. 3.2 is not the particle physical radius, but an particle-effective. Despite similar nomenclature, the particle-effective radius is not the effective radius of the size distribution defined in Eq. 3.2. The particle-effective radius is defined as:

$$r_e = \frac{3 \cdot IWC(r)}{4 \cdot \rho_{ice} \cdot A(r)} = \frac{3 \cdot V(r)}{4 \cdot A(r)}, \quad (3.3)$$

where $IWC(r)$ is the mass of the ice particle with physical radius r , ρ_{ice} is the density of ice, $A(r)$ is the projected area of ice particle with radius r , and $V(r)$ is the volume of ice particle with radius r (Francis et al., 1994). As previously mentioned, this particle-effective radius is used as the particle radius in Eq. 3.2.

With the size distribution known, the effective optical properties of that size distribution can be determined following Baum et al. (2011). Specifically, the optical properties are normalized by the size distribution and the optical cross-sections. For instance, the extinction efficiency can be described via:

$$Q_{ext,eff}(\lambda) = \frac{\int_{r_{e,min}}^{r_{e,max}} Q_{ext}(r_e, \lambda) \cdot A(r_e) \cdot n(r_e) \cdot dr_e}{\int_{r_{e,min}}^{r_{e,max}} A(r_e) \cdot n(r_e) \cdot dr_e}, \quad (3.4)$$

where, $Q_{ext,eff}(\lambda)$ is the effective extinction efficiency of the size distribution at wavelength λ , $Q_{ext}(r_e, \lambda)$ is the extinction efficiency of particles with particle-effective radius r_e at wavelength λ , and $A(r_e)$ is the projected area of the particles. Note, the extinction efficiency multiplied by the projected area is the extinction cross section. Likewise, the scattering efficiency is given by:

$$Q_{sca,eff}(\lambda) = \frac{\int_{r_{e,min}}^{r_{e,max}} Q_{ext}(r_e, \lambda) \cdot SSA(r_e, \lambda) \cdot A(r_e) \cdot n(r_e) \cdot dr_e}{\int_{r_{e,min}}^{r_{e,max}} A(r_e) \cdot n(r_e) \cdot dr_e}, \quad (3.5)$$

where $SSA(r_e, \lambda)$ is the single scattering albedo of particles with particle-effective radius r_e at wavelength λ and all other variables are the same as defined above. The single scattering albedo is the ratio of scattering efficiency to extinction efficiency, or the ratio of scattering efficiency to the sum of scattering and absorption efficiency. Thus, the single scattering albedo multiplied by the extinction cross section is the scattering cross section. Similarly, $1 - SSA(r_e, \lambda)$ represents the absorption efficiency. As such, the absorption efficiency of the gamma size distribution is given by:

$$Q_{abs,eff}(\lambda) = \frac{\int_{r_{e,min}}^{r_{e,max}} Q_{ext}(r_e, \lambda) \cdot [1 - SSA(r_e, \lambda)] \cdot A(r_e) \cdot n(r_e) \cdot dr_e}{\int_{r_{e,min}}^{r_{e,max}} A(r_e) \cdot n(r_e) \cdot dr_e}. \quad (3.6)$$

Note, Equations 3.4 - 3.6 assume the number of particles is known. Instead, implemented here is the relative number of particles for weighting as opposed to actual number of particles. This methodology is valid given the assumed size distribution shown in Fig. 21. Specifically, the solution to the extinction efficiency of the size distribution written in summation form using a simple left-method Riemann sum to solve the integral:

$$Q_{ext,eff}(\lambda) = \frac{\sum_{i=r_{e,min}}^{r_{e,max}} Q_{ext,i}(\lambda) \cdot A_i \cdot \Delta r_{e,i} \cdot \frac{n_i}{\sum_{j=r_{e,min}}^{r_{e,max}} n_j}}{\sum_{i=r_{e,min}}^{r_{e,max}} A_i \cdot \Delta r_{e,i} \cdot \frac{n_i}{\sum_{j=r_{e,min}}^{r_{e,max}} n_j}}, \quad (3.7)$$

where $\Delta r_{e,i}$ is the step size for particle-effective radius r_e (from Eq. 3.3). Note, relative number concentration, given by $\frac{n_i}{\sum_{j=r_{e,min}}^{r_{e,max}} n_j}$, is simply taken as the gamma size distribution given in Eq. 3.2 divided by the sum of the size distribution. In fact, this relative number concentration is what is shown in Fig. 21. Following the same methods, the scattering efficiency of the size distribution can be written as:

$$Q_{sca,eff}(\lambda) = \frac{\sum_{i=r_{e,min}}^{r_{e,max}} Q_{ext,i}(\lambda) \cdot SSA_i(\lambda) \cdot A_i \cdot \Delta r_{e,i} \cdot \frac{n_i}{\sum_{j=r_{e,min}}^{r_{e,max}} n_j}}{\sum_{i=r_{e,min}}^{r_{e,max}} A_i \cdot \Delta r_{e,i} \cdot \frac{n_i}{\sum_{j=r_{e,min}}^{r_{e,max}} n_j}}, \quad (3.8)$$

and the absorption efficiency as:

$$Q_{sca,eff}(\lambda) = \frac{\sum_{i=r_{e,min}}^{r_{e,max}} Q_{ext,i}(\lambda) \cdot [1 - SSA_i(\lambda)] \cdot A_i \cdot \Delta r_{e,i} \cdot \frac{n_i}{\sum_{j=r_{e,min}}^{r_{e,max}} n_j}}{\sum_{i=r_{e,min}}^{r_{e,max}} A_i \cdot \Delta r_{e,i} \cdot \frac{n_i}{\sum_{j=r_{e,min}}^{r_{e,max}} n_j}}. \quad (3.9)$$

Now that effective scattering and absorption efficiencies for the size distribution are known, only the phase function is needed for the 1DVar system and RTTOV. The effective phase function of the size distribution can be determined by weighting the phase function of each particle in the size distribution by the scattering cross section. Thus, particles with little scattering will exhibit less influence over the effective phase function than those with significant scattering. In integral form, the phase function at each angle θ is given by:

$$P_{eff}(\lambda, \theta) = \frac{\int_{r_{e,min}}^{r_{e,max}} P(r_e, \lambda, \theta) \cdot Q_{ext}(r_e, \lambda) \cdot SSA(r_e, \lambda) \cdot A(r_e) \cdot n(r_e) \cdot dr_e}{\int_{r_{e,min}}^{r_{e,max}} Q_{ext}(r_e, \lambda) \cdot SSA(r_e, \lambda) \cdot A(r_e) \cdot n(r_e) \cdot dr_e}, \quad (3.10)$$

where $P_{eff}(\lambda, \theta)$ is the effective phase function of the size distribution at wavelength λ and scattering angle θ and $P(r_e, \lambda, \theta)$ is the phase function of ice with particle-effective radius r_e , wavelength λ , and scattering angle θ . As before, writing this in summation form using a left-method Riemann sum:

$$P_{eff}(\lambda, \theta) = \frac{\sum_{i=r_{e,min}}^{r_{e,max}} P_i(\lambda, \theta) \cdot Q_{ext,i}(\lambda) \cdot SSA_i(\lambda) \cdot A_i \cdot \Delta r_{e,i} \cdot \frac{n_i}{\sum_{j=r_{e,min}}^{r_{e,max}} n_j}}{\sum_{i=r_{e,min}}^{r_{e,max}} Q_{ext,i}(\lambda) \cdot SSA_i(\lambda) \cdot A_i \cdot \Delta r_{e,i} \cdot \frac{n_i}{\sum_{j=r_{e,min}}^{r_{e,max}} n_j}}. \quad (3.11)$$

The effective phase function can be described by a relative magnitude for each scattering angle as is calculated in Eq. 3.11. This, however, is not efficient for these purposes. Specifically, the input files for cloud properties for the 1DVar system and RTTOV are already very large as they contain the optical properties for each of the 1305 wavelengths and 54 model levels. Further, it is more computationally

efficient to define the phase function as coefficients for Legendre polynomials that approximate the phase function. That is, the phase function can be described as a series of polynomials with increasing degree, via a process described in Wiscombe (1977). Specifically, the phase function can be approximated via:

$$P[\lambda, \cos(\theta)] = \sum_{n=0}^N (2n + 1) \cdot \chi_n(\lambda) \cdot P_n[\cos(\theta)], \quad (3.12)$$

where $P[\lambda, \cos(\theta)]$ is the phase function for wavelength λ and scattering angle θ , N is the number of coefficients for expansion, $\chi_n(\lambda)$ is the n-th expansion coefficient for wavelength λ , and $P_n[\cos(\theta)]$ is the n-th Legendre Polynomial. Wiscombe (1977) also provides a solution for the expansion coefficients, χ_n , in integral form:

$$\chi_n(\lambda) = \frac{1}{2} \cdot \int_0^\pi P[\lambda, \cos(\theta)] \cdot P_n[\cos(\theta)] \cdot \sin(\theta) \cdot d\theta. \quad (3.13)$$

Note, the integral in Eq. 3.12 is from 0 to π because the phase function is assumed symmetric. Finally, using a left-method Riemann sum, the phase function expansion coefficients, χ_n can be determined via:

$$\chi_n(\lambda) = \frac{1}{2} \cdot \sum_{i=0}^N P[\lambda, \cos(\theta_i)] \cdot P_n[\cos(\theta_i)] \cdot \sin(\theta_i) \cdot \Delta\theta. \quad (3.14)$$

Note, Eq. 3.14 assumes the sum of the phase function is 1.0.

Since the true phase function is known, the error in the phase function as defined by Legendre expansion can be determined. In Fig. 22 the root mean squared error (RMSE) as a function of number of Legendre expansion coefficients is shown. While the Legendre expansion representation of the phase function is never a perfect representation for the optical model used here with less than 100 coefficients, the RMSE of

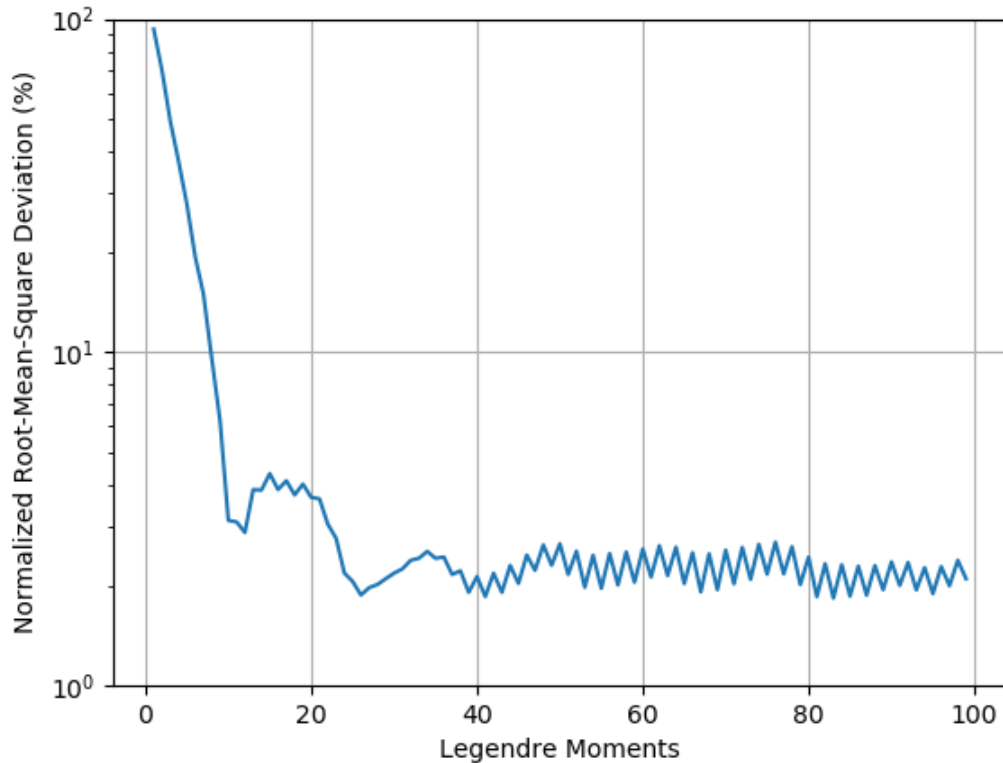


Figure 22: Normalized root mean squared error (RMSE) of the phase function by number of Legendre expansion coefficients.

the phase function converges to around 1% at near 30 moments. As such, the phase function has been defined using 30 Legendre expansion coefficients.

While strong forward scattering peaks are not usually a concern in the IR, Delta-M scaling of the phase function as described by Wiscombe (1977) is performed here for completeness. Delta-M scaling removes sharp forward scattering peaks in the phase function that may result in aliasing of the Legendre expansion coefficients (see the phase function peaks near 0° scattering angle in Fig. 24). Delta-M scaling is

performed using the following relationship:

$$\chi_m^*(\lambda) = \frac{\chi_m(\lambda) - \chi_{N+1}(\lambda)}{1 - \chi_{N+1}(\lambda)}, \quad (3.15)$$

where χ_m^* is the scaled Legendre expansion coefficient, and χ_{N+1} is the expansion coefficient for the $N + 1$ -th moment where N is the maximum number of moments used. Thus, in this case χ_{N+1} in this case is χ_{31} .

After Delta-M scaling, the forward scattering that cannot be described by the number of Legendre moments used is assumed to be transmitted (i.e., unaffected). As such, the scattering optical depth must be updated to account for the removal of the forward scattered light. Using equations 20a-b in Wiscombe (1977) the Delta-M normalized optical depth is:

$$\tau'_\lambda = \tau_\lambda \cdot [1 - (SSA_\lambda \cdot \chi_{N+1})], \quad (3.16)$$

where τ'_λ is the normalized optical depth at wavelength λ , τ_λ is the actual optical depth at wavelength λ , SSA_λ is the single scattering albedo at wavelength λ and χ_{N+1} is as described for eq. 3.15. Likewise, using equations 20a-b in Wiscombe (1977), the normalized single scattering albedo is given by:

$$SSA'_\lambda = SSA_\lambda \cdot \frac{1 - \chi_{N+1}}{[1 - (SSA_\lambda \cdot \chi_{N+1})]}. \quad (3.17)$$

3.3.1.2 Optical Properties Verification

To ensure the proper application of the methodology presented in section 3.3.1.1 for determining the bulk optical properties, verification is required. Since the gamma size distribution used for the MODIS Collection 6 cloud property retrieval algorithm is applied, it is reasonable to use the properties reported for that product for verifica-

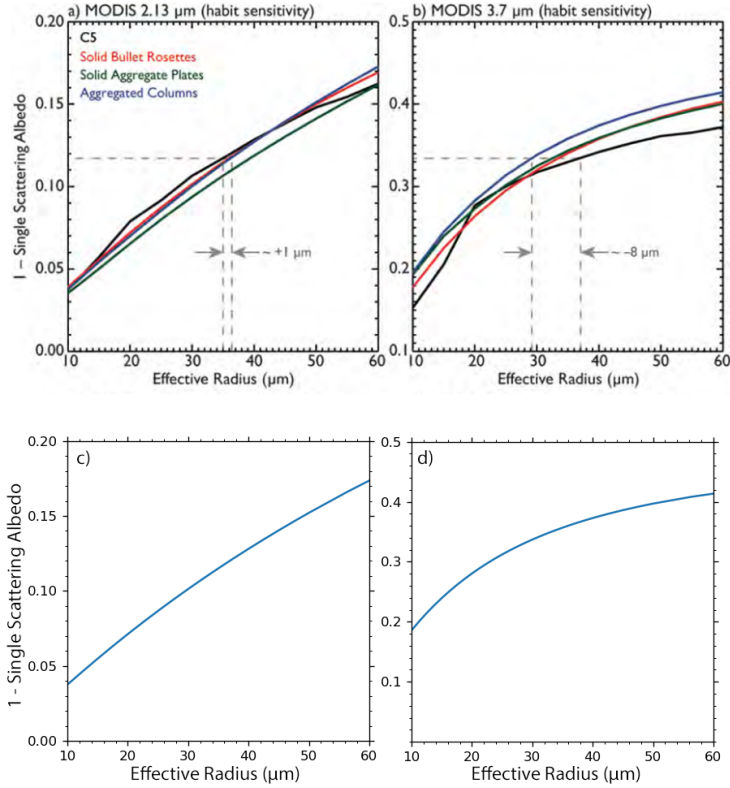


Figure 23: Absorption efficiency (given by 1-SSA) for MODIS band (a) 2.13 μm and (b) 3.7 μm as a function of effective radius. Also shown in (c-d) is the absorption efficiency derived here for the same bands. The curve in (c-d) corresponds to the (blue) *Aggregated Columns* curve in (a-b). (a-b) is adapted from Platnick et al. (2017).

tion. However, the MODIS spectral bands are rather wide (i.e., 0.1 - 1.0 μm) whereas the CrIS bands are much thinner in comparison. As such, the spectral response of the MODIS bands must be accounted for by integrating the optical properties with respect to the MODIS band spectral response functions. For comparison, the optical properties for the following 4 MODIS Bands are calculated: 0.87, 1.63, 2.13, and 3.70 μm . Note, while most of these bands are primarily solar and not IR bands, the process outlined above is identical for both solar and IR. Thus, a consistent result in the solar is sufficient to indicate consistent results in the IR.

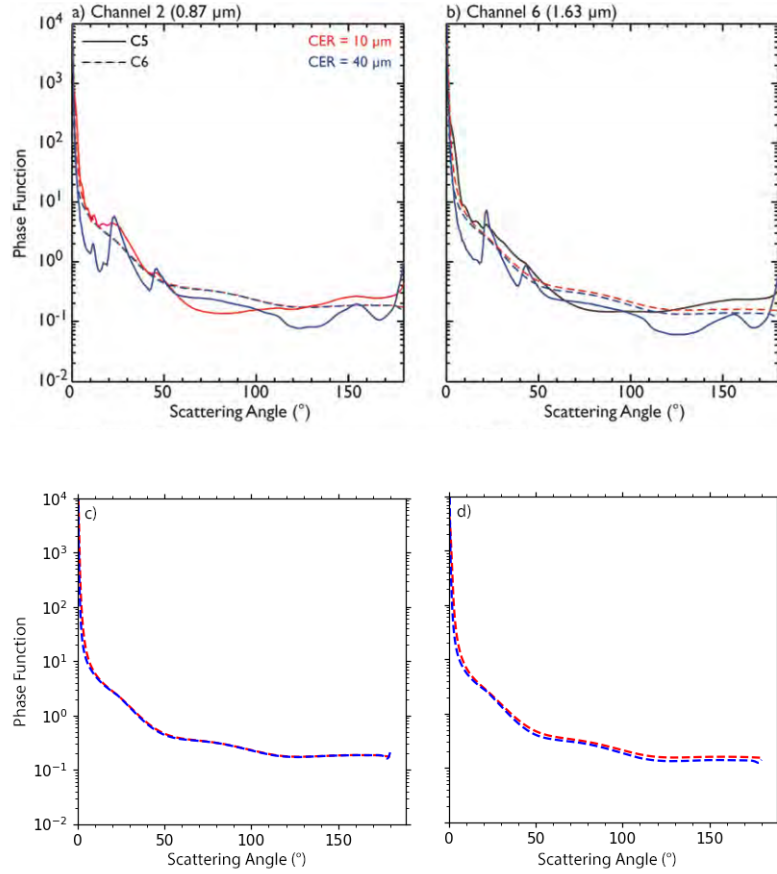


Figure 24: Phase function for MODIS band (a) $0.87 \mu\text{m}$ and (b) $1.63 \mu\text{m}$ for (red) $10 \mu\text{m}$ and (blue) $40 \mu\text{m}$ effective radii. Also shown in (c-d) is the phase function derived here for the same bands and effective radii. The curves in (c-d) corresponds to the (dashed) *Collection 6* curve in (a-b). (a-b) is adapted from Platnick et al. (2017).

The comparison of the absorption efficiency reported by the MODIS *Collection 6* document (Platnick et al., 2017) and that determined here for the MODIS bands is shown in Fig. 23. Given that the results developed here are identical to those shown for *Aggregated Columns*, the model developed here is identical to that of MODIS for extinction, absorption, and scattering efficiency and single scattering albedo.

The comparison of the phase function reported by the MODIS *Collection 6* document (Platnick et al., 2017) and that derived here is shown in Fig. 24 for four different

bands and two effective radii. Again, the results are consistent, verifying the derived phase functions.

3.3.1.3 Optical Properties of Cirrus at CrIS Wavelengths

While the optical properties are known for all 1305 CrIS channels used here, cloud optical depth is only defined in the visible at 532 nm at the 43 different optical depths discussed in section 3.2.4. Using the extinction efficiency at 532 nm though, the extinction at other wavelengths can be determined. Specifically, optical depth can be defined as:

$$\tau_\lambda = \int_{SFC}^{TOA} N(z) \cdot \sigma_{ext,eff,\lambda}(z) \cdot dz, \quad (3.18)$$

where τ_λ is the optical depth at wavelength λ , $N(z)$ is the number of particles at altitude z , and $\sigma_{ext,eff,\lambda}(z)$ is the effective extinction cross section of the size distribution at altitude z and wavelength λ . If evaluated over the a homogeneous layer, the layer optical depth can be defined as:

$$\tau_\lambda = N \cdot \sigma_{ext,eff,\lambda} \cdot \Delta z, \quad (3.19)$$

The ratio of the optical depth at 532 nm to any wavelength for a homogeneous layer can be expressed as:

$$\frac{\tau_{532nm}}{\tau_\lambda} = \frac{N \cdot \sigma_{ext,eff,532nm} \cdot \Delta z}{N \cdot \sigma_{ext,eff,\lambda} \cdot \Delta z} = \frac{\sigma_{ext,eff,532nm}}{\sigma_{ext,eff,\lambda}}. \quad (3.20)$$

Note, the extinction cross section at some wavelength is just the size distribution effective area A_{eff} multiplied by the extinction efficiency at that wavelength $Q_{ext,\lambda}$, or:

$$\sigma_{ext,eff,\lambda} = A_{eff} \cdot Q_{ext,\lambda}. \quad (3.21)$$

Thus, given the extinction efficiencies at 532 nm and any other wavelength, the optical depth at that wavelength can be determined from the 532 nm optical depth via:

$$\tau_{\lambda} = \tau_{532nm} \cdot \frac{Q_{ext,\lambda}}{Q_{ext,532nm}}. \quad (3.22)$$

Finally, the scattering and absorption optical depth for any wavelength is found via the total optical depth and the single scattering albedo.

3.3.2 Synthetic Hyperspectral Observations

As mentioned above, synthetic HIS observations for the CrIS sensor aboard the Suomi-NPP satellite are created using RTTOV. To create these HIS observations, the simulated clouds discussed in section 3.2.4 are provided to RTTOV via an ASCII file with Delta-M normalized layer scattering and absorption optical depth and the 30 normalized Legendre expansion coefficients of the phase function for each vertical layer and wavelength. That said, as may be inferred when examining the optical model derivation described in section 3.3.1.1, all of the provided optical properties are dependent upon the cloud ice effective radius. Here, the Heymsfield et al. (2014) temperature to effective radius relationship is used to constrain cloud ice effective radius, and thus, optical properties.

The Heymsfield et al. (2014) parameterization relates atmospheric temperature to ice crystal effective radius using in-situ observations collected within ice clouds. As mentioned above, due to sampling biases, this parameterization may not equal truth. That said, it has been used extensively in radiation modeling studies (e.g., Marquis et al., 2017; Campbell et al., 2021; etc.). The computed ice crystal effective radius as determined using the Heymsfield et al. (2014) parameterization for the clouds simulated here is shown in Fig. 25 along with the standard parameterization. Note,

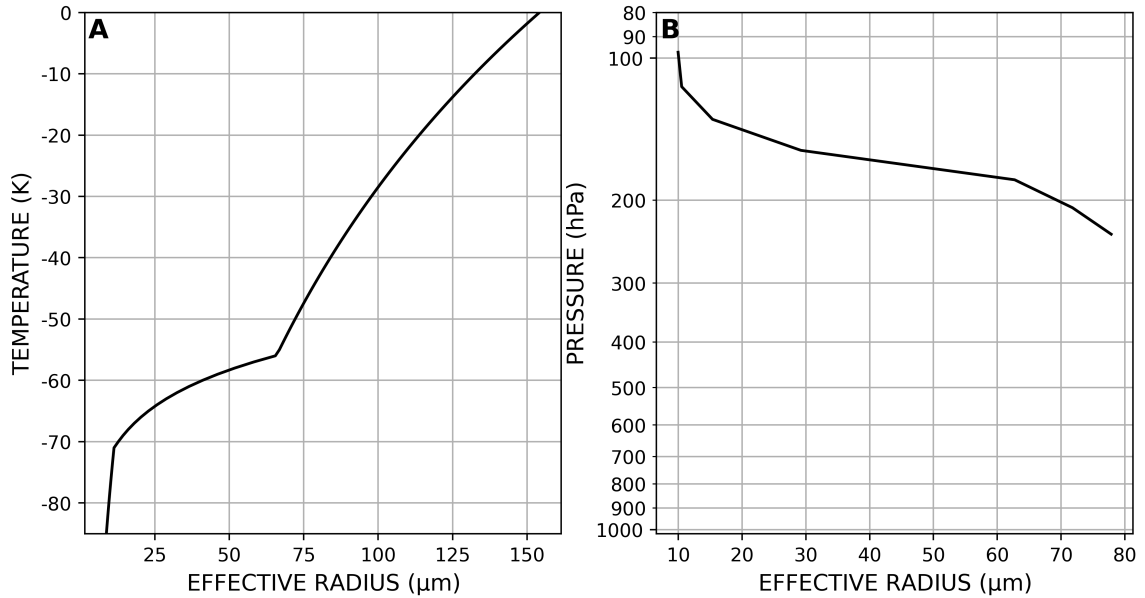


Figure 25: (A) Heymsfield et al. (2014) ice crystal effective radius versus temperature parameterization and (B) the ice crystal effective radius as a function of pressure altitude for the standard tropical atmosphere used here.

ice effective radius decreases significantly from near 80 μm for the lowest cloud to near 10 μm for the highest cloud. Because visible optical depth has been constrained and smaller crystals are more effective at extinguishing light than larger crystals, the total ice mass (defined via ice water content) of the cloud decreases slightly with altitude. Specifically, for the Yang et al. (2013) and Bi and Yang (2017) optical model used here, a cloud with ice effective radius of 10 μm will exhibit total ice water content 1.27% higher than a cloud with identical 532 nm optical depth, but with an effective radius of 75 μm .

With effective radius constrained, the optical properties at each CrIS wavelength can be determined and provided to RTTOV. RTTOV is run with the same configuration as is used by the 1DVar system, providing synthetic radiances for the standard tropical atmosphere with simulated clouds. These radiances are saved locally as is. Additionally, noise is added using the methods implemented in the 1DVar system

mentioned above. Note, all simulations are performed with solar terms turned off (i.e., nighttime).

3.3.3 Radiance Impacts

3.3.4 Determining Radiance and Analysis Bias

To determine the radiance impacts of cirrus clouds, a RTTOV is run with no clouds to provide clear-sky synthetic radiances. By comparing these to the synthetic radiances without noise, the impacts of cirrus cloud on measured radiances can be determined. The synthetic radiances with noise are then provided to the 1DVar system and the analyzed temperature and humidity fields are examined.

By running the 1DVar system twice, once with no cloud properties in the background or analysis (i.e., clear-sky assumption) and once with the cloud properties provided to the system, two analyses are retrieved. By using the exact same observation such that the noise is identical between the two runs, the difference between the analyses should be due to the cloud. This is performed for all of the possible COD and cloud altitude combinations described above giving a matrix of bias estimates. Finally, the contamination statistics found for NAVDAS (Fig. 5) can be superimposed and integrated to get an estimated analysis error for clouds that actually pass screening. Note, in reality NAVDAS assimilates observations from a variety of sources and implements a different background error covariance matrix. As such, these estimates would likely present a worst-case scenario in which only cloud contaminated HIS radiances were available.

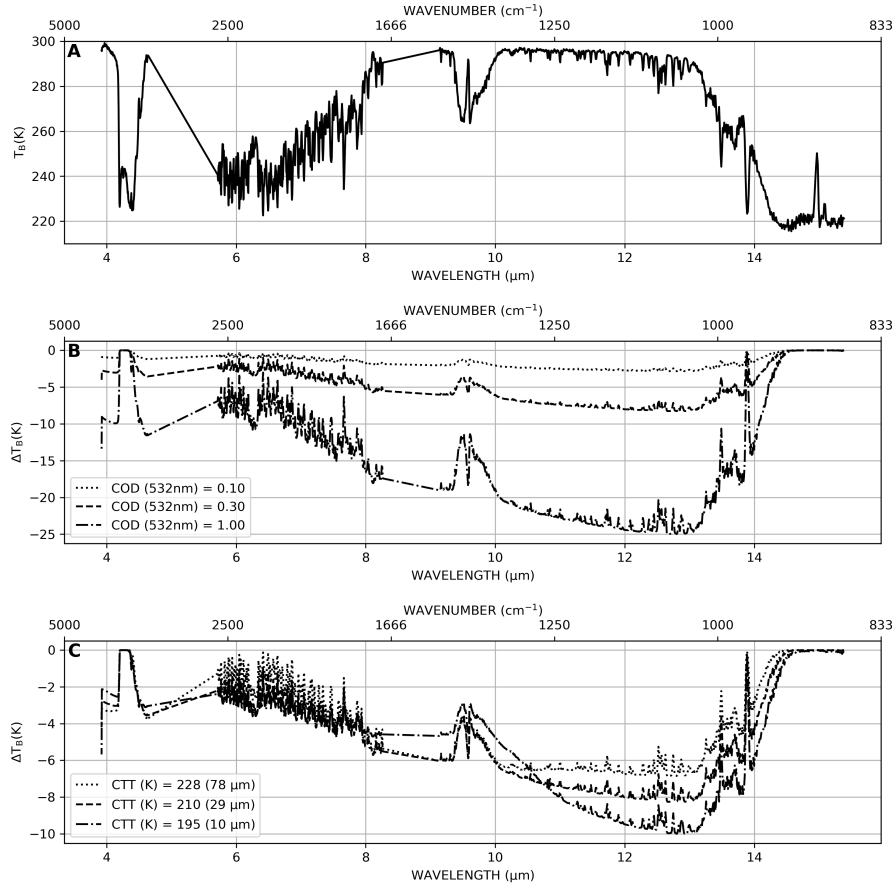


Figure 26: (A) CrIS clear-sky brightness temperature curve for the standard tropical atmosphere and (B) brightness temperature bias for a cloud with cloud top temperature of 210 K and (dotted) COD of 0.10, (dashed) COD of 0.30, and (dot-dashed) COD of 1.00. Also, (C) the brightness temperature bias of a cloud of COD 0.30 with (dotted) cloud top temperature of 228 K, (dashed) 210 K, and (dot-dashed) 195 K.

3.4 Results

3.4.1 Cirrus Induced Radiance Biases

The simulated clear-sky brightness temperature is presented in Fig. 26 along with the biases due to cirrus clouds of differing cloud top temperature and COD. For a cloud at 210 K, a COD of 0.10 exhibits a peak brightness temperature bias of just below 3 K near a wavelength of 12 μm. Note, 3 K is also the innovation threshold implemented

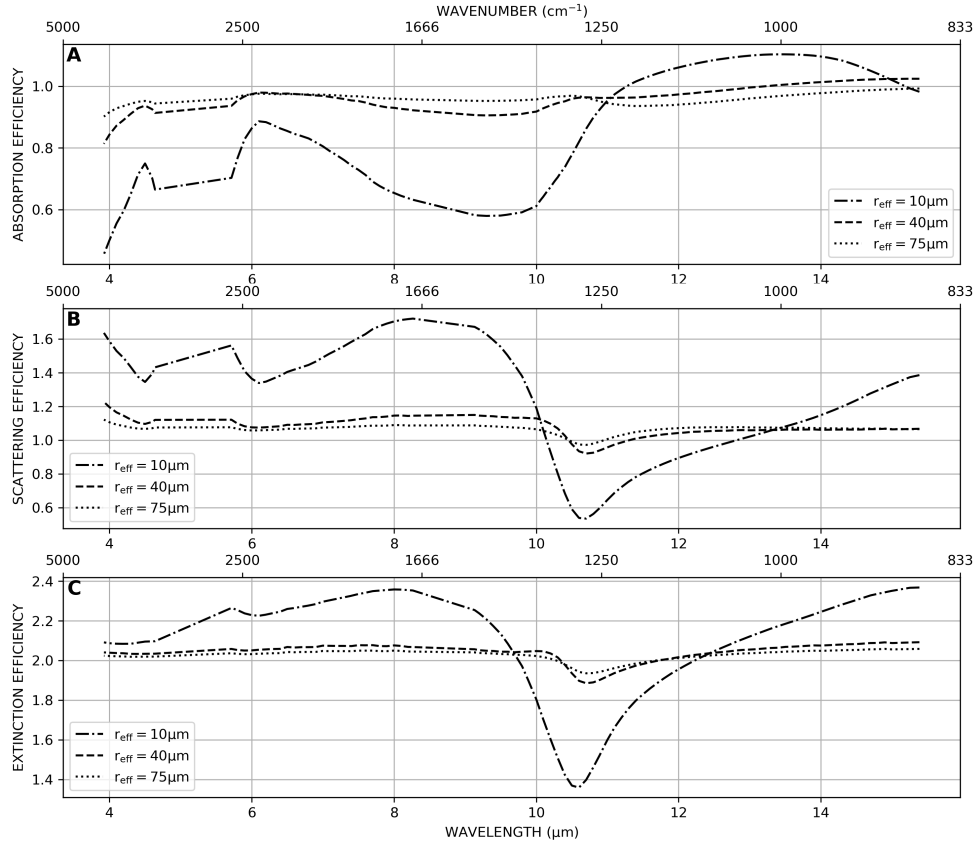


Figure 27: (A) Absorption efficiency, (B) scattering efficiency, and (C) extinction efficiency for the CrIS wavelengths for effective radii of (dot-dashed) 10 μm , (dashed) 40 μm , and (dotted) 75 μm . Created using the 8CASM optical model from Yang et al. (2013).

by NAVDAS (see section 1.3). Thus, it would be expected that a cloud of visible COD 0.10 and cloud top temperature of 210 K would pass screening measures. As may be anticipated, when optical depth increases, brightness temperature bias also increases. For example, a COD of 0.30 and 1.00 correspond to peak biases of near 10 K and 25 K, respectively. This cold bias is due to some of the lower atmospheric emitted radiance being absorbed by the cloud while the cloud itself emits some radiance, albeit at a much colder temperature. As such, brightness temperature is overall decreased. The impact of cloud top temperature on brightness temperature is a bit less straight-

forward though. For example, between 5.5 μm and 8.5 μm the 228 K cloud imparts less bias than the colder clouds. This pattern flips between 9.5 μm and approximately 11 μm , with the coldest cloud imparting the bias. At wavelengths over 11 μm , the coldest cloud again imparts the largest bias. This is the physical manifestation of a minimum in extinction efficiency of the smaller ice effective radius of the coldest clouds primarily due to decreased IR absorption - and thus emission via Kirchhoff's law (Liou, 2002) - as shown in Fig. 27. It is important to note that the scattering, absorption, and extinction efficiencies at effective radii of 40 and 75 μm are very similar. Interestingly, the spectral difference of the smaller ice crystals at 190 K may indicate a possible method of cloud effective radius, and thus, cloud top temperature retrieval using HIS sensors similar to the study presented by Pierangelo et al. (2004) for aerosol, though such a topic is not examined further here.

3.4.2 Jacobian Impacts

As discussed before, the Jacobians describe the sensitivity of the measured radiance to some state variable (e.g., temperature). As such, the Jacobians are used in finding the analysis that minimizes the cost function shown in Eq. 1.3. The clear-sky temperature Jacobians are shown in Fig. 2, but these Jacobians are no longer valid in the presence of cloud since cloud is not transparent in the IR.

The temperature Jacobians for two lower tropospheric peaking CrIS bands at 8.0 μm and 12.0 μm with cloud present is shown in Fig. 28. As mentioned earlier, because cloud is non-transparent, as optical depth increases, less signal from the lower atmosphere reaches the sensor. Further, because the cloud layer is now partially opaque, some of the radiance measured by the sensor is from the cloud layer. Since new, or at the very least more, information is available from the cloud layer, attempts at cloudy-sky assimilation for fully opaque cloud layers have resulted in increased

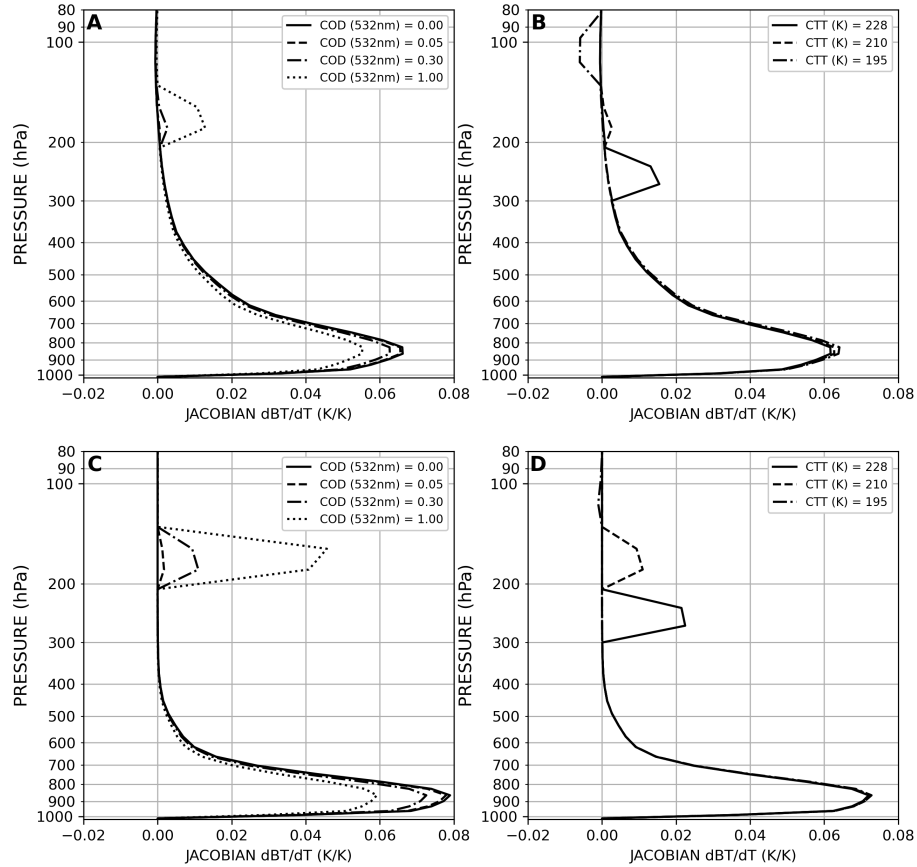


Figure 28: Temperature Jacobians as a function of 532 nm cloud optical depth (A & C) for a cloud with cloud top temperature of 210 K and (B & D) as a function of cloud top temperature for an optical depth of 0.30 for CrIS bands (A-B) 745 corresponding to 8.0 μm and (C-D) 293 corresponding to 12.0 μm .

analysis accuracy above cloud (McNally, 2009; Okamoto, 2013). Interestingly, for the highest cloud layers, the temperature Jacobian actually becomes negative. This is presumably due to the cloud being within the tropopause and near the stratospheric temperature inversion where temperature increases with altitude. Finally, it is important to recognize that even for clouds with visible COD of 1.0, there is still sensitivity to the lowest portions of the atmosphere. As such, it may be possible to see increased analysis accuracy beneath the cloud when performing cloudy-sky IR radiance assimilation of semi-transparent clouds. Thus far however, cloudy-sky assimilation in the

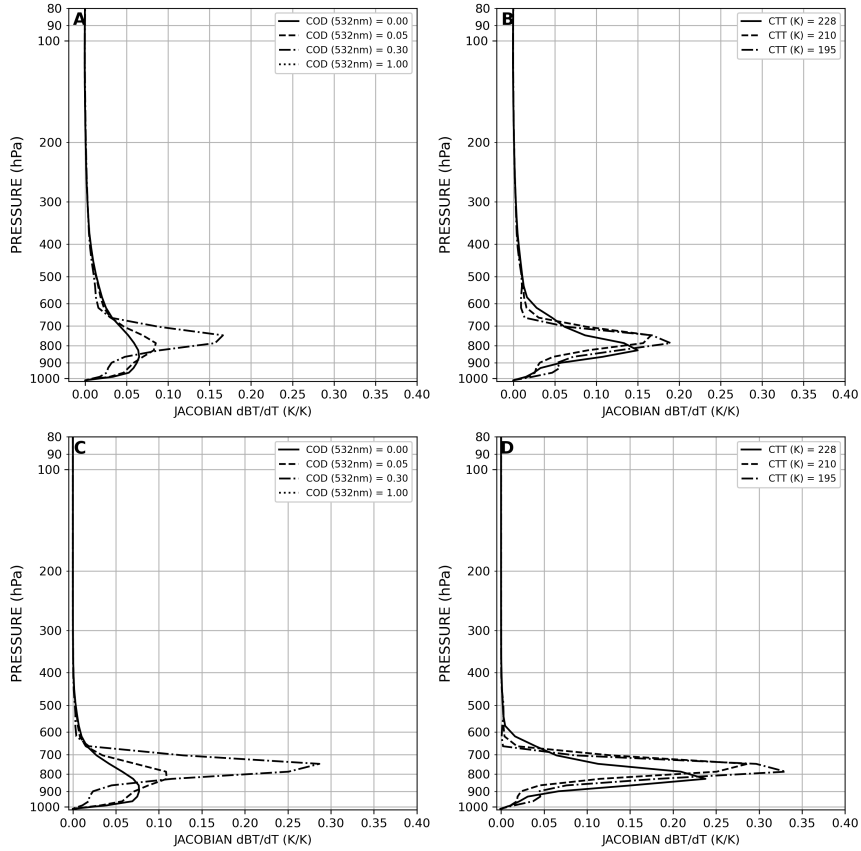


Figure 29: Temperature Jacobians when background and analysis contain no cloud as a function of 532 nm cloud optical depth (A & C) for a cloud with cloud top temperature of 210 K and (B & D) as a function of cloud top temperature for an optical depth of 0.30 for CrIS bands (A-B) 745 corresponding to 8.0 μm and (C-D) 293 corresponding to 12.0 μm .

IR has been limited to opaque scenes and cloud has been represented very simply, so these impacts may not be realized in the near future.

When the background and analysis atmosphere contains no cloud (i.e., observation assumed clear), the contribution from the cloud layer is not realized by the forward model, resulting in the unusual results shown in Fig. 29. Specifically, the spikes visible when clouds are present indicate the system has interpreted the cloud impacts to brightness temperatures as a large increase in lower atmospheric opacity - mostly likely by increasing low-level moisture. In other words, because the system assumes

the observation is clear-sky, the system rectifies the differences between the simulated and observed radiances by adding low-level moisture to rise the peak altitude of the Jacobians and decrease the analysis' brightness temperatures. As such, the impact of the cloud is not seen primarily within the cloud layer, but much lower in the atmosphere.

3.4.3 Cirrus Impact on Analyzed Temperature & Moisture

While the cirrus impact on brightness temperature can help indicate which clouds are likely to pass screening, it does not provide much insight on how that cloud-induced bias translates to analysis bias. As mentioned above and similar to that performed for the aerosol study presented in Ch. 2, the analysis bias is determined by taking the difference between the analysis when the true cloud properties are provided to RTTOV versus when the contaminated observation is assimilated as if it were a clear-sky observation. Whereas the aerosol study was performed this way to ensure isolation of the aerosol impact, the process is even more important here due to the inclusion of noise in the synthetic CrIS observations. Because the noise is identical for both 1DVar runs, the analyses differences should indicate an isolated cirrus impact.

The maximum temperature and dew point biases in the troposphere as a function of cloud top temperature and COD are shown in Fig. 30. As expected as COD increases or cloud top temperature decreases, the maximum tropospheric bias in both temperature and dew point increase. For instance, the cloud discussed above with COD of 0.1 and cloud top temperature of 210 K (i.e., the cloud that induces brightness temperature biases that should pass screening) would impart a maximum temperature bias of about 3 K and dew point bias of near 10 K. Note, despite this cloud likely passing screening, the biases it imparts are nearly 7 and 3 times larger than the expected background uncertainty, respectively. Conversely, the same cloud

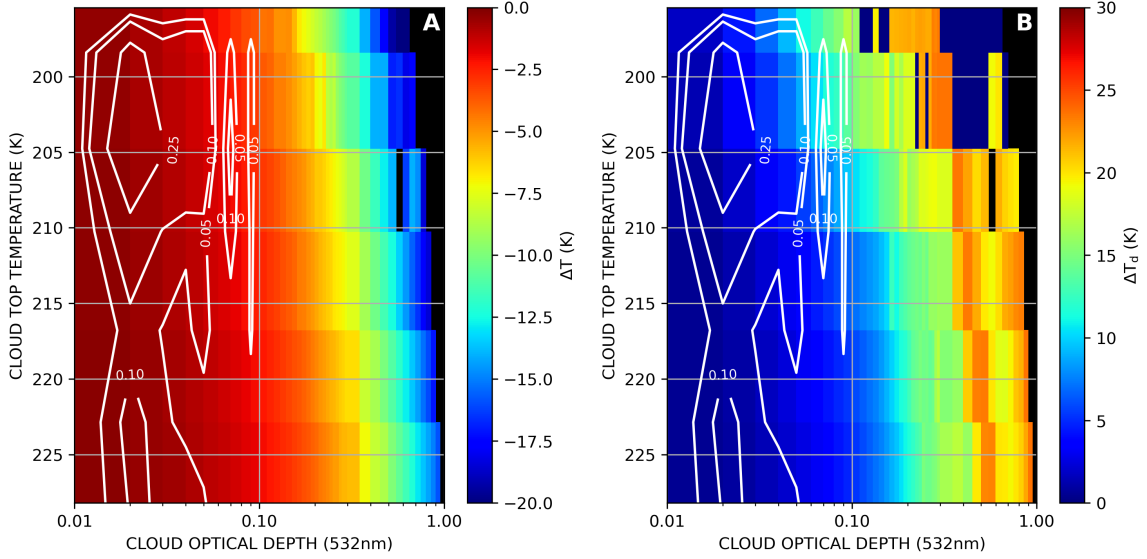


Figure 30: Maximum analyzed (A) temperature and (B) dew point bias in the tropopause associated with assimilation of cloud contaminated radiances when assuming clear-sky observations as a function of cloud top temperature and optical depth. Black areas indicate that the assimilation system failed to converge to a solution when assuming clear-sky. Super-imposed in white is the contamination percentage of that cloud type as determined by co-location with lidar observations.

with a cloud top temperature of 225 K only imparts a 2.5 K temperature and 7 K dew point. Likewise, a cloud with a cloud top temperature of 210 K and optical depth of 0.03 would only impart a bias of near 2 K in temperature and 5 K in dew point. Note, there are two signals present in these biases, one due to cloud temperature and one due to optical differences associated with different effective radii. That said, because effective radii is constrained with temperature using the Heymsfield et al. (2014) parameterization, the impact of different effective radii at a specific temperature is not examined. Regardless, for all but the coldest clouds, the optical properties are not extremely variable for the effective radii used here. As such, much of the impact is likely due to the cloud temperature itself.

Superimposed upon the biases are the relative frequencies of contamination as shown in 5. For instance, a cloud with COD of 0.02 and cloud top temperature of 205 K occurs in over 0.25% of all observations. By integrating the bias with the contamination frequencies, the bias of the mean contaminating cloud can be determined. This method was performed by Marquis et al. (2017) to estimate expected sea surface temperature bias. Using the contamination statistics, the maximum tropospheric temperature bias due to the average contaminating cloud is 1.43 K and dew point bias is 4.29 K, while the biases normalized by the 7.7% contamination rate are 0.11 K for temperature and 0.33 K for dew point. Note, the maximum biases are, on average, below the expected uncertainties in temperature and dew point, but this is again only for the global contamination rate of near 7%. In regions where cirrus is predominately present, errors will be much larger. For instance, in the Tropical Atlantic where cirrus is present between 30-40% of the time, bias may be much times near 0.4 to 0.6 K for temperature and 1.3 to 1.7 K for dew point. Meanwhile, in Southeast Asia, cirrus is present in 50-60% of observations suggesting bias may be as high as 0.86 K for temperature and 2.57 K for dew point. Thus, in these regions, assimilation of HIS radiances may be imparting biases as large or larger than the expected background uncertainty.

While the maximum biases in the troposphere are concerningly large, it is important to understand the average uncertainty in the tropospheric analyses. This bias can be determined using the tropospheric root mean squared error (RMSE). These tropospheric temperature and dew point RMSEs as a function of cloud top temperature and COD are shown in Fig. 31. As expected, the RMSEs are smaller than the maximum biases, but still large when compared to the background uncertainties of 0.4 K for temperature and near 3.5 K for dew point. For example, for a cloud of COD 0.1 and cloud top temperature of 210 K, the tropospheric RMSE in tem-

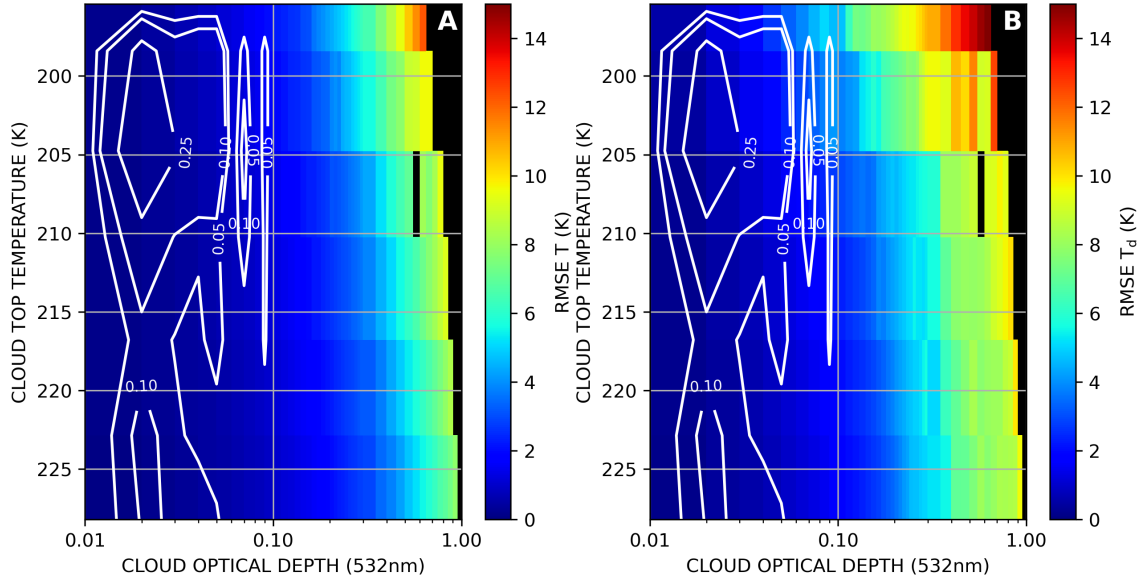


Figure 31: As in Figure 30 except for tropospheric root mean squared error.

perature is near 3 K and the dew point RMSE is near 5 K, both much larger than the expected uncertainty. Again, as COD increases and/or cloud top temperature decreases, RMSE increases.

Superimposed upon the tropospheric RMSEs are again the contamination frequencies. When integrated, the tropospheric RMSE for the average cloud is 0.78 K for temperature and 1.56 for dew point. Using the contamination rate of 7.7%, the average tropospheric RMSE is 0.06 K for temperature and 0.12 K for dew point. In regions with presumably higher contamination such as the Tropical Atlantic this corresponds to as much as 0.31 K for temperature and 0.62 K for dew point. For temperature, this is near the expected background uncertainty, yet this RMSE is indicative of the entire troposphere, not a maximum bias. Further, in Maritime Southeast Asia, RMSEs may be as large as 0.47 K for temperature (i.e., larger than the background uncertainty) and 0.95 K for dew point.

3.5 Discussion

While cirrus clouds contaminate assimilated HIS radiances less than that of aerosols, their impact can be much larger for lower optical depths due to much more thermal contrast with the surface. Due to the increased thermal contrast, the impacts on observed radiances is very large, allowing for better screening. For instance, only optically thin cirrus with optical depths less than 0.3 contaminate assimilated HIS radiances. Further, the contamination rate is only near 7.7%. That said, cirrus clouds are often present at high frequencies in many regions important for tropical cyclone forecasting.

While more strict screening measures could better limit assimilation of cirrus biased radiances, since cirrus contamination happens in other radiometric products at rates nearly 4 times larger than that for HIS assimilation, strict screening may be resulting in rejection of clear-sky observations. Thus, such a process is not optimal. Further given the maximum analysis biases, unsatisfactory errors will be present unless clouds as thin as CODs of 0.03 are screened. While information from visible channels can be used to attempt to better screen clouds, this would only be possible during daylight hours. As, nighttime impacts could be even larger.

It is important to note that the above results represent a near worst-case scenario. In operations, observations from several observing platforms are used, limiting the impact of any one biased observation. In regions where few observations are available and the only observation may be from an HIS sensor, the above results may be possible.

CHAPTER 4

AEROSOL INFRARED RADIATIVE CLOSURE

4.1 Introduction

4.1.1 Rationale

The study presented in chapter 2 and Marquis et al. (2021), suggest that aerosol-sky assimilation may be possible using model aerosol analyses. While that study held aerosol properties static for both the background and analysis, aerosols are not one-size-fits-all. In fact, aerosols come from a variety of sources, chemical makeups, and sizes. While it is important to ensure the impact of aerosols are correctly modeled, in practical, aerosol-related modeling studies must make assumptions about the optical properties of these aerosols present. This is often done by implementing pre-built optical models based on an aerosol size and/or type. For instance, the OPAC model discussed above provides optical properties for 4 sub-types of dust, among other aerosol types. Despite this relatively simple classification, aerosol optical properties are known to evolve as they age (Reid and Hobbs, 1998).

In this study, the impact of aerosols and aerosol optical properties on NWP is simplified to focus only on the aerosol radiative effects. In particular, this study attempts to answer the following question:

Are the optical models currently implemented sufficient to model the radiative effects of aerosols?

In the following study, the impact of aerosol optical model on aerosol radiative forcing is examined using measurements collected during the Studies of Emissions and Atmospheric Composition, Clouds and Climate Coupling by Regional Surveys (SEAC⁴RS; Toon et al., 2016) field campaign.

4.1.2 Background

As mentioned in chapter 2, aerosols interact with radiation either through absorption or scattering. This interaction can cause significant decreases in the amount of solar radiation reaching the surface, resulting in a much cooler near-surface temperature (e.g., Zhang et al., 2016). Likewise, infrared radiation from the surface can be absorbed and re-emitted by aerosols, increasing minimum near-surface temperatures (Jacob, 1999). The impacts are not limited to the surface though. For instance, Carlson and Benjamin (1980) report the radiative effects of Saharan Dust by specifically examining solar and IR heating rates. They found increased solar heating throughout the aerosol layer, with increased IR heating near the bottom of the layer and IR cooling in the middle and upper portions of the aerosol layer. Specifically, they report total heating rates of up to 1 K per day within the aerosol layer for a visible optical depth of 1.0.

Despite these significant impacts on both surface and atmospheric radiation budgets, until recently, these aerosol radiative effects were either ignored or based on aerosol climatology in weather forecasts (Tegen et al., 1997). The radiative impact of aerosols is substantial enough that even when only aerosol climatology is used, significant increases in forecast skill are found (e.g., Tompkins et al., 2005). Using climatology is insufficient for transient aerosol events however. For those cases, aerosol must be predicted for accurate forecasts. Carson-Marquis et al. (2021) ingested aerosol analyses from NAAPS into a weather prediction model and found

substantial increases in accuracy of predicted surface measured solar radiation and near-surface temperature. Despite the promising early results, the process of including aerosols in weather prediction is still rather new and only recently has research been focused on verifying the radiative impacts of aerosols from models. Further, these efforts to incorporate prognostic aerosols in NWP likely fix the aerosol optical properties for prediction of radiative impacts. It is therefore necessary to study the variances in shortwave and IR radiative impacts between different commonly used aerosol optical models.

One of the direct methods for studying the impacts of aerosol properties to the atmospheric radiation balance is through a *radiative closure* study. In the radiative closure approach, simulated radiation is compared to observed values using the observed or simulated atmospheric profile, occasionally including aerosol, cloud, and/or surface physical and optical properties. In such an exercise, the sensitivity of several pre-built optical models is examined with respect to radiative closure and examine the ability NWP aerosol analyses to recreate the observed radiative fluxes.

In a similar vein, Oyola et al. (2019) examined the accuracy of using modeled aerosol analyses to simulate the radiative effects of solar radiation absorbing aerosols. This study was based upon observations collected during the SEAC⁴RS field campaign. Specifically, they used observations of the aerosol profile measured from lidar to calculate broadband solar fluxes to achieve radiative closure for a smoke and urban aerosol plume sampled over Northeastern Wyoming on 19 August 2013. They examined the impact of different surface albedos and aerosol profiles from observations and models on radiative forcing compared to broadband flux measurements. Oyola et al. (2019) reported that the model vertical distribution of aerosols was insufficient to provide closure, causing substantial heating rate biases. This analysis is somewhat limited however. Firstly, they focused on urban and smoke aerosols which are not

active in the IR. As such, the ability for the models to recreate aerosol impacts in the IR could not be commented on. Further, urban and smoke aerosol optical properties are much more constrained than other aerosols such as dust. As such, they did not see it necessary to confirm the optical properties using in-situ observations. Thus, despite the results of Oyola et al. (2019), experiments using other aerosol types are required.

Haywood et al. (2011a) examined the IR and solar radiative effects of a dust event sampled off the coast of Saharan Africa during the Geostationary Earth Radiation Budget Intercomparison of Long-wave and Short-wave radiation (GERBILS) during June 2007 (Haywood et al., 2011b). While they did examine the difference in some of the optical properties of dust by changing dust shape from spheroids to irregular hexagonal prisms, this analysis was only performed in the solar spectrum. Further, while Haywood et al. (2011a) did investigate the use of aerosol optical depth from a Met Office global NWP model, the investigation was limited to optical depth and not flux or heating rate representativeness.

In the following section, a dust aerosol plume sampled during the SEAC⁴RS campaign is presented. The case discussed is then used for studying the accuracy of pre-built aerosol optical models for dust and the ability of aerosol model analyses to sufficiently recreate the observed radiative profile.

4.1.3 08 August 2013

The SEAC⁴RS field campaign collected observations using 57 science flights during August and September 2013 based out of Ellington Field Joint Reserve Base near Houston, Texas (location indicated in Fig. 32). The campaign had a broad set of goals, including investigating atmospheric composition and examining the lower stratosphere, the Earth's radiation budget, and tropospheric chemistry over North



Figure 32: Aircraft ground tracks for the relocation flight from Palmdale Regional Airport to Ellington Field Joint Reserve Base on 08 August 2013. (Red) ER-2 flight track and (Blue) DC-8 flight track.

America. To achieve these goals, three aircraft were used (the NASA ER-2, DC-8, and the SPEC Inc. Learjet) each with a wide array of instrumentation.

On 08 August 2013, the ER-2 and DC-8 aircraft relocated from Palmdale, California (34.633°N , 118.074°W , 775 m AMSL) to Ellington Field Joint Reserve Base near Houston, Texas (29.999°N , 95.163°W , 10 m AMSL). The aircraft tracks for this relocation flight are shown in Figure 32. During the relocation flights, the aircraft encountered a plume of dust over the Northern Gulf of Mexico. The dust plume was present with little to no cloud, except for transient high altitude cirrus. The Cloud Physics Lidar (CPL; McGill et al., 2002) backscatter curtain plot from the ER-2 is shown in Fig. 33. The backscatter curtain shows the measured reflected light as a function of time. Because the aircraft is in movement much faster than the evolution

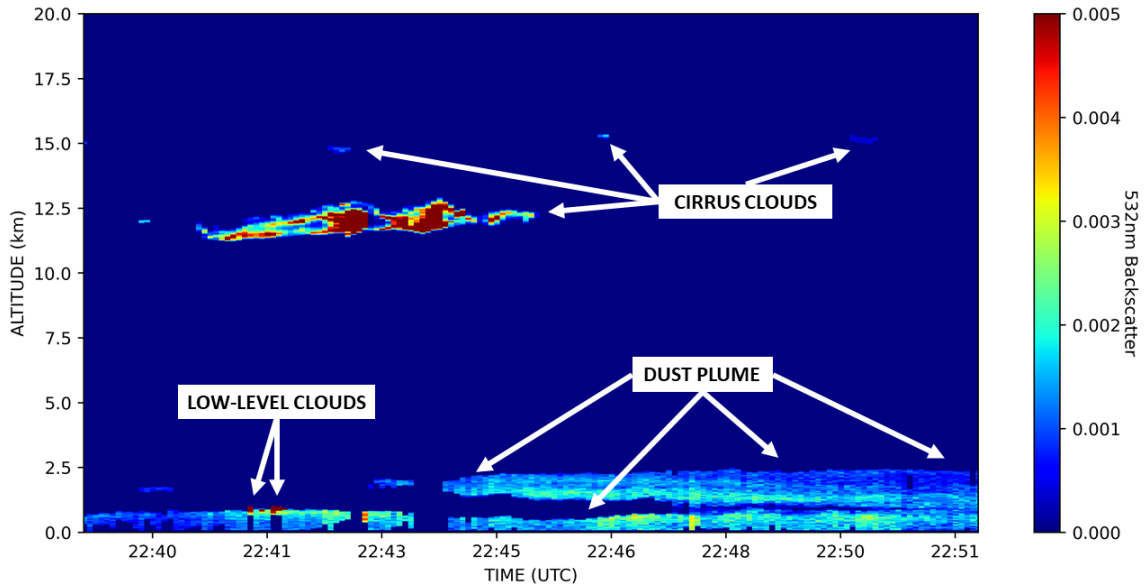


Figure 33: CPL measured backscatter from on-board the ER-2 during the first transect of the aerosol plume with features identified.

of the plume or clouds, the curtain can be approximated to an instantaneous view of the atmosphere along the aircraft track. Indicated on Fig. 33 are the transient high altitude cirrus, the few low-level clouds, and the aerosol plume. Using satellite imagery, it is determined that this plume of dust likely originated in the Sahara desert and has been transported across the Atlantic and Caribbean.

After exiting the Louisiana coast and entering the Northern Gulf of Mexico, the DC-8 circled and dropped in altitude to prepare to sample the dust layer. The DC-8 and ER-2 then flew in tandem with the DC-8 within the dust plume below 1 km in altitude and the ER-2 at 18-20 km altitude. After transecting the dust plume, the ER-2 continued to Ellington Field for landing while the DC-8 continued for two more transects of the dust plume: one more traveling eastward within the plume, and a final transect above the plume headed back westward. The aircraft altitude and ground track for each of the three transects is shown in Fig. 34.

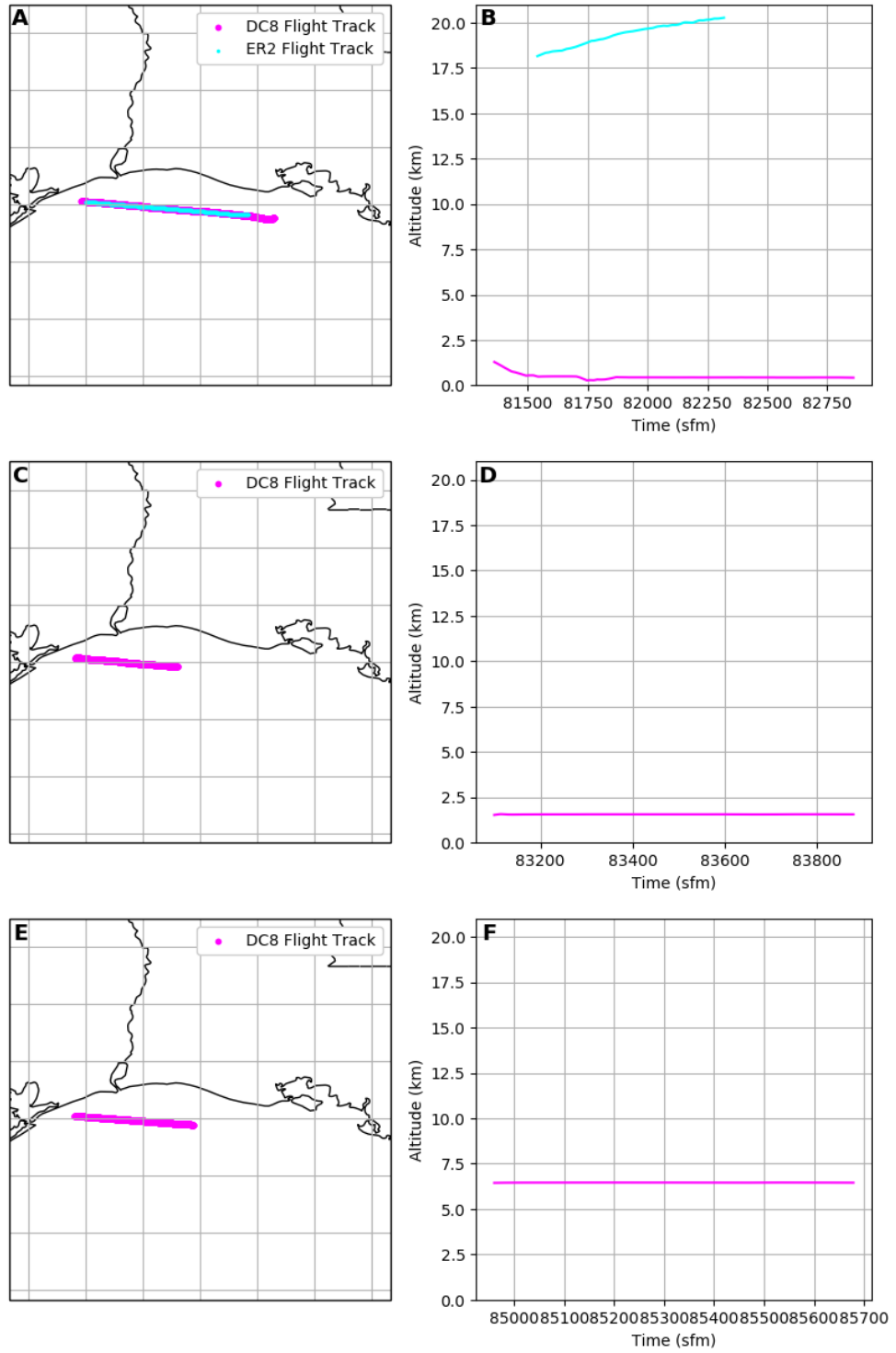


Figure 34: Aircraft ground tracks and altitudes for the three transects of the dust plume on 08 August 2013. (Cyan) ER-2 flight track and (Magenta) DC-8 flight track.

Because the dust is present over open ocean with little cloud present, this case provides an opportunity to attempt radiative closure with IR-active aerosols. Using the observations collected, the impact of aerosol optical model on radiative flux and heating rate can be examined. Then, the accuracy of the radiative fluxes and heating rates determined using model aerosol analyses can be determined. Finally, because the DC-8 collected measurements within the dust plume, basic analysis of the representativeness of pre-built aerosol optical models for this dust aerosol plume can be performed.

4.2 Datasets & Models

4.2.1 Fu-Liou-Gu Radiative Transfer Model

For radiative transfer, the Fu-Liou-Gu (FLG) radiative transfer model is used (Gu et al., 2011). The FLG model is built upon the Fu-Liou radiative transfer model (Fu and Liou, 1992, 1993) with updated and improved parameterizations for ice crystals and aerosols.

The Fu-Liou RTM simulates broadband fluxes and heating rates using 6 solar and 12 IR wavelength bands indicated in Table 1. By using relatively wide spectral bands, the FLG RTM can perform extremely rapid flux and heating rate calculations making it very useful for NWP. The FLG model is highly configurable, allowing users to define number of vertical levels, choose the between two and four radiation streams, provide aerosol and cloud information, either broadband or spectral surface emissivity and albedo, as well as meteorological profiles. Additionally, up to 22 trace gases can be considered for simulations. For simulations, users must provide temperature, moisture, and ozone concentrations at each model level. To include aerosols, layer AOD and wavelength for the AOD can be provided to the FLG model. The

Table 1: Spectral bands used in radiative transfer simulations by the Fu-Liou-Gu radiative transfer model.

Solar Spectrum			Infrared Spectrum		
Band Number	Center Wavelength (μm)	Band Limits (μm)	Band Number	Center Wavelength (μm)	Band Limits (μm)
1	0.55	0.20-0.70	7	4.90	4.55-5.26
2	1.00	0.70-1.30	8	5.60	5.26-5.88
3	1.60	1.30-1.90	9	6.50	5.88-7.14
4	2.20	1.90-2.50	10	7.60	7.14-8.00
5	3.00	2.50-3.50	11	8.50	8.00-9.09
6	3.70	3.50-4.00	12	9.60	9.09-10.20
			13	11.3	10.20-12.50
			14	13.7	12.50-14.93
			15	16.6	14.93-18.52
			16	21.5	18.52-25.00
			17	30.0	25.00-35.71
			18	70.0	35.71-10 ⁴

OPAC aerosol optical models and the Tegen and Lacis (1996) dust optical models are pre-built into the FLG source code. The FLG model determines AOD at other wavelengths using extinction ratios for the aerosol optical models built into the source code. Note, this means that extinction efficiency is not stored, but instead a value that is representative of the ratio between the extinction efficiencies. The impacts of this caveat will be discussed later.

While FLG solves the radiative transfer model similar to RTTOV discussed in chapters 2 and 3, FLG does so using only the 18 bands indicated in Table 1 and up to only four radiation streams. Due to this simplicity, it cannot accurately simulate radiances, but is sufficiently accurate for solar and IR fluxes and/or heating rates. As such, the FLG model has been used for several closure and radiative forcing studies (e.g., Lolli et al., 2017; Oyola et al., 2019; Campbell et al., 2021). As such, FLG is more simple than RTTOV and generally less resource intensive.

4.2.2 GEOS-5 Meteorological & Aerosol Profiles

The SEAC⁴RS data archive¹ includes meteorological and aerosol analyses for each of the DC-8 and ER-2 from the GEOS-5 SEAC⁴RS mini-reanalysis fields (Molod et al., 2015). Unlike MERRA-2, this reanalysis is performed specifically for the SEAC⁴RS campaign. The analyses have been sampled to the aircraft track at 60 second temporal resolution using flow-following interpolation. Meteorological variables pressure, temperature, specific humidity, aerosol mass mixing ratio at 72 vertical levels plus the surface are available and used for this study. The GEOS-5 analysis uses the Goddard Chemistry Aerosol Radiation & Transport (GOCART) aerosol model. Among other aerosol types, the GOCART model represents dust aerosols as a function of the dust particle size using size bins (Ginoux et al., 2001). While GOCART is built to allow for 8 size bins, the version implemented in GOCART allows for 5 size bins with effective particle radii of 0.5, 1.4, 2.4, 4.5, and 8.0 μm . Later, the optical properties of the GEOS-5/GOCART analyzed dust aerosols are determined by applying the size distribution into the OPAC and Tegen and Lacis (1996) optical models.

4.2.3 Surface Reflectance

Because sunlight will be reflected by the surface, the surface reflectance or albedo needs to be described and provided to the FLG model. The surface albedo is determined by modifying the surface albedo as reported in the Clouds and the Earth's Radiant Energy System (CERES) level-3 Synoptic TOA and surface fluxes and clouds at 1-degree (SYN1deg) and monthly resolution. Note, only albedo from the CERES sensors on the AQUA and TERRA satellites is considered here. The CERES reported broadband albedo for the northern Gulf of Mexico is shown in Fig. 35.

¹<https://www-air.larc.nasa.gov/cgi-bin/ArcView/seac4rs>

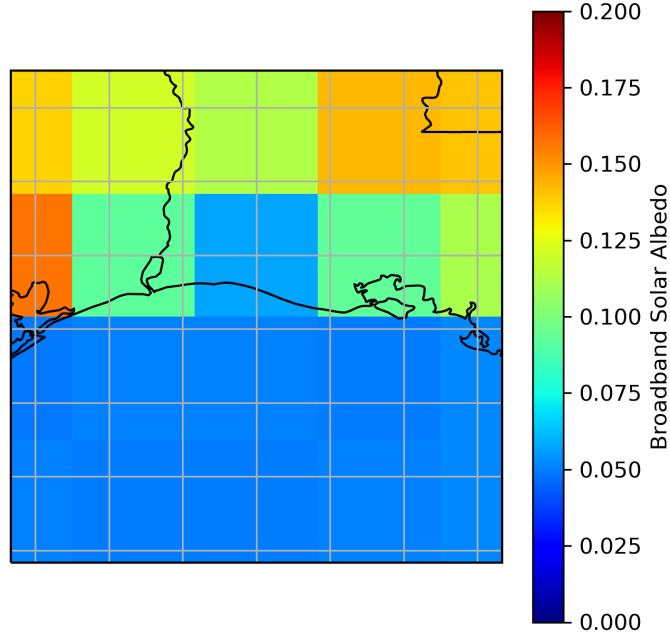


Figure 35: Average broadband solar albedo over the northern Gulf of Mexico from CERES aboard the NASA TERRA and AQUA satellites for August 2013.

Since ocean water albedo changes with solar zenith angle, the CERES albedo is corrected for the solar zenith angle of the study window. A solar zenith correction factor is developed using ocean surface albedo to solar zenith angle relationship reported by Taylor et al. (1996):

$$A = \frac{0.037}{1.1\mu_0^{1.4} + 0.15}, \quad (4.1)$$

where A is the albedo and μ_0 is the cosine of the solar zenith angle. The correction factor applied is simply the ratio of the albedos as calculated by Taylor et al. (1996) for the solar zenith of the study window to the solar zenith of the mean CERES overpass time (set to 37°). The correction factor for the study window is set to 1.90. Given the CERES reported broadband albedo of 0.055, the albedo for this study window is set to 0.105.

4.2.4 Broadband Radiometers

On board both the DC-8 and ER-2 are the Naval Research Laboratory (NRL) broadband radiometers (BBR). These instruments measure the hemispheric solar and IR fluxes (or irradiances) using modified Kipp & Zonen CM22 pyranometers and CG4 pyrgeometers, respectively (Bucholtz et al., 2010). By placing an upward and downward facing BBR, both the upwelling and downwelling fluxes are measured. The solar radiometer measures flux from 0.2 to 3.6 μm and the IR radiometer measures flux from 4.5 to 42 μm with an estimated 3-5% uncertainty. Note the BBR on the ER-2 only measures IR fluxes and the results using this instrument on this aircraft are not shown here. The BBR measured fluxes are available at the online SEAC⁴RS data archive, however, fluxes with additional corrections were provided by the instrument PI (A. Bucholtz).

4.2.5 DIAL-HSRL

The Airborne Differential Absorption Lidar (DIAL) - High Spectral Resolution Lidar (HSRL) instrument on board the DC-8 measures ozone concentration using UV lasers while also measuring aerosol profiles using visible and near-IR lasers (Hair et al., 2008; Burton et al., 2012, 2013). The DIAL-HSRL provides aerosol backscatter at 355, 532, and 1064 nm at 30 m vertical resolution and approximately 10s temporal resolution. Aerosol extinction at 532 nm at 270 m vertical resolution is reported at 60s temporal resolution. The DIAL-HSRL is installed within the aircraft with both downward and upward pointed telescopes, allowing retrievals in both vertical directions. Note, backscatter or extinction is not available directly adjacent to the aircraft in either direction for approximately 500 m for backscatter or 1500 m for extinction. As such, when the DC-8 is near or within the aerosol layer, most of the plume is in this region without data.

Unlike the MPL discussed in Ch. 2, the DIAL-HSRL directly retrieves 532 nm extinction using the HSRL technique (Hair et al., 2008). The HSRL technique separates the aerosol contribution to the measured signal from the contribution due to air molecular scattering by using the spectral distribution of the measured signal. From the aerosol signal, the lidar ratio can be directly retrieved. As such, the DIAL-HSRL does not need a coincident optical depth measurement or an assumed extinction-to-backscatter ratio to derive extinction coefficient.

4.2.6 PINeph

Also on the DC-8 is the Polarized Imaging Nephelometer (PINeph; Espinosa et al., 2019). The PINeph data files report aerosol size distribution, single scattering albedo, extinction coefficient, asymmetry parameter, and phase function among other variables. Measurements are made in-situ by measuring the light scattering and absorption of individual aerosols. Because the PINeph measures aerosols passing through an inlet on the aircraft, the measured aerosol properties are limited only to the aircraft altitude. In other words, there may be representativeness errors associated with the PINeph measurements. For example, Rogers et al. (2009) compared nephelometer observations with HSRL retrievals. While nephelometer extinction measurements correlated well with the HSRL extinction, large differences occurred when the nephelometer performed measurements near the edge of the aerosol plume. Note, the PINeph does not directly measure size distribution, but instead uses provides the Generalized Retrieval of Aerosol and Surface Properties (GRASP; Dubovik et al., 2014) software the measured phase function linear-polarized and phase function from which the GRASP software infers the size distribution.

Table 2: Default 532 nm lidar ratios used in unconstrained aerosol extinction retrievals using CPL.

Aerosol Type	532 nm Lidar Ratio
Marine	25.0
Marine Mixture	45.0
Dust	45.0
Dust Mixture	35.0
Clean/Background	55.0
Polluted Continental	65.0
Smoke	70.0
Volcanic	45.0

4.2.7 CPL

Installed on the ER-2 is the Cloud Physics Lidar (CPL). The CPL measures below aircraft backscatter and derived extinction at 355, 532, and 1064 nm wavelengths and approximately 1 s temporal resolution (McGill et al., 2002). The CPL backscatter and extinction are provided at 30 m vertical resolution. Unlike the DIAL-HSRL, extinction is not directly retrieved, but is derived using a variety of methods identical to those used for Cloud-Aerosol Transport System (CATS) lidar (Yorks et al., 2016). The four methods for Lidar ratio determination are: constrained, unconstrained default, modified default, and opaque, with the constrained and unconstrained being the main methods (John E. Yorks, *personal communication, June 2021*). In the constrained method, the lidar ratio is determined by estimating the amount of signal that is lost within the aerosol layer. This method requires the aerosol layer to be both transparent and above an area of pristine air without any cloud or aerosol. When the constrained method is unavailable, the system falls back to an unconstrained or default method where the lidar ratio is set to a default value based upon the object being sensed. These default lidar ratios are shown in Table 2. Note, in cases where

the default lidar ratio is used, uncertainties exist in derived extinction due to this assumed lidar ratio. That said, due to the ER-2 aircraft's relatively high altitude, the CPL provides a complete view of the troposphere, and is used extensively in this case.

Note, the CPL backscatter and extinction profiles are available in the level 2.0 profile product dataset while the method used for determination of the lidar ratio is stored within the level 2.0 layer product dataset. Thus, as a precursor to analysis and further use of this data, each valid extinction value in the profile product and that value's corresponding lidar ratio determination method is extracted and stored in a merged dataset.

4.2.8 Aerosol Models

Built into FLG are the dust aerosol optical models from the Optical Properties of Aerosols and Clouds (OPAC) database (Hess et al., 1998). For the OPAC database (also discussed in section 2.2.8, the optical properties of spherical dust particles are defined for four different dust optical models based upon dust of different sizes: nucleating-mode, accumulating-mode, coarse-mode, and transported-mode. For this study, the OPAC database is prebuilt in FLG as look-up-tables of spectral-relative extinction coefficient, asymmetry parameter, and single scattering albedo. For PINeph comparison methods discussed in section 4.3.5, OPAC version 3.1 is used to determine dust model optical properties. Note, there exists a version of OPAC with updated dust optical properties based upon spheroids (Koepke et al., 2015), this version is not used here.

While OPAC assumes dust aerosols are spherical, because dust is formed from mechanical weathering, these aerosols are often irregularly shaped (Falkovich et al., 2001). While spheroid dust particles have similar single scattering albedos and ex-

inction efficiencies to spherical dust, the phase function and asymmetry parameter can be quite different (Fu et al., 2009). Particularly, non-spherical dust will suppress backwards scattering and increase sideward scattering (Koepke and Hess, 1988). That said, while these scattering properties are important in the shortwave spectrum, in the IR, scattering by dust is less significant. Despite this caveat, the OPAC database is still widely used and only a few studies have examined its validity in different scenes (e.g., Wagner et al., 2009; Bi et al., 2016)

Also built into the FLG RTM are dust optical models from Tegen and Lacis (1996). These include optical properties of dust for five different effective radii at 0.5, 1.0, 2.0, 4.0, and 8.0 μm . The optical properties of the Tegen and Lacis (1996) model are derived from Mie-scattering experiments assuming a gamma size distribution with effective variance of 0.2 and refractive indices reported by Volz (1973) and Patterson et al. (1977). Because both Volz (1973) and Patterson et al. (1977) report the refractive indices for Saharan dust, the Tegen and Lacis (1996) optical model is likely best for dust originating from the Sahara desert. As with OPAC, the dust aerosols are assumed spherical, though they report the spherical assumption is sufficient for fluxes and heating rates (Tegen and Lacis, 1996).

4.3 Methodology

4.3.1 Verifying Fu-Liou-Gu

To ensure FLG has been compiled and configured correctly, a verification test is performed in which radiative closure is attempted in a relatively simple atmosphere. To perform this verification, the level 1.0 solar flux measurements from the AERONET site at Bermuda (32.370°N, 64.696°W, 10.0 m AMSL) on a day with little to no cloud or aerosol (07 March 2009) are used. The AERONET location is indicated on the

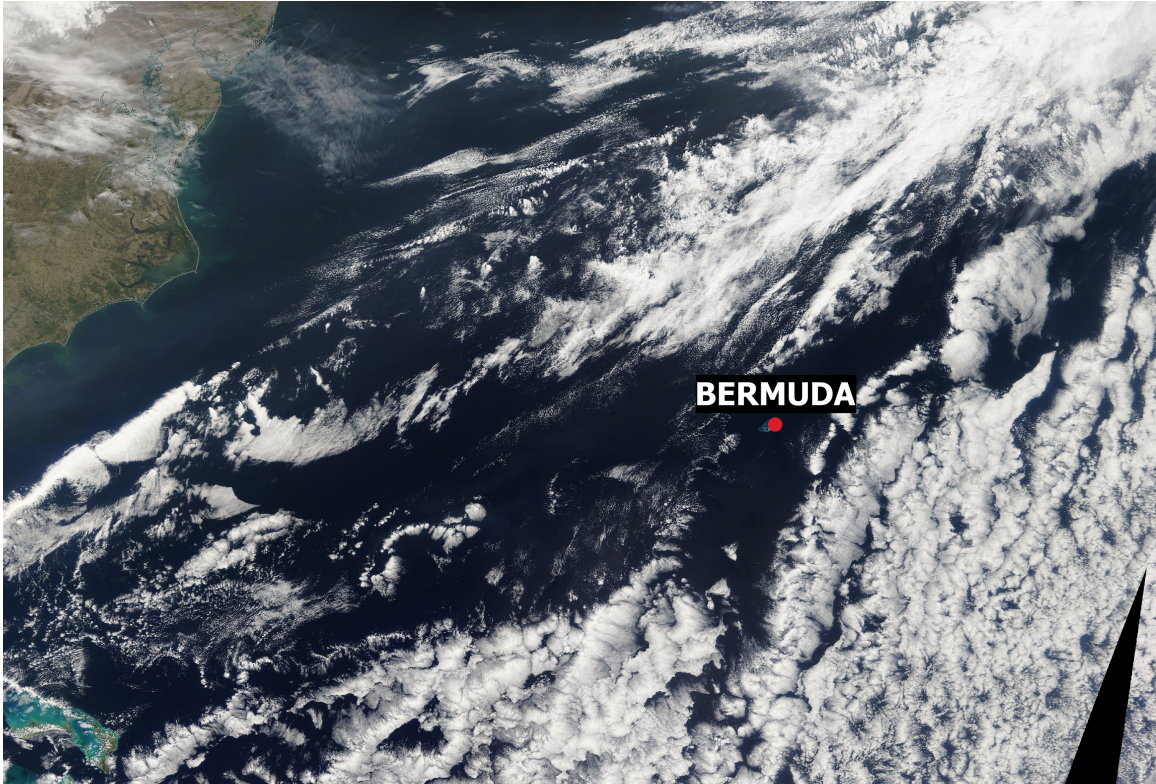


Figure 36: TERRA-MODIS true color image from 07 March 2009 with the Bermuda AERONET site indicated by the red point.

TERRA-MODIS true color image from that day at near 10:30 AM Local Time in Fig. 36. As evident in the true color image, while clouds exist in the regions around Bermuda, the island is under clear skies. For verification, downwelling broadband solar flux measured at the Bermuda AERONET site is used. The three radiosonde soundings launched from Bermuda (32.37°N , 64.68°W , 37.0 m AMSL) at 00 UTC and 12 UTC on 07 March and 00 UTC on 08 March are used for the meteorological profiles.

Downwelling solar flux calculations from FLG are determined at 60 s resolution throughout the day consistent with the 60 s observations reported by AERONET. For the meteorological profile provided to FLG, the three soundings are interpolated linearly with time to 60 s resolution of the solar flux measurements. Note, while

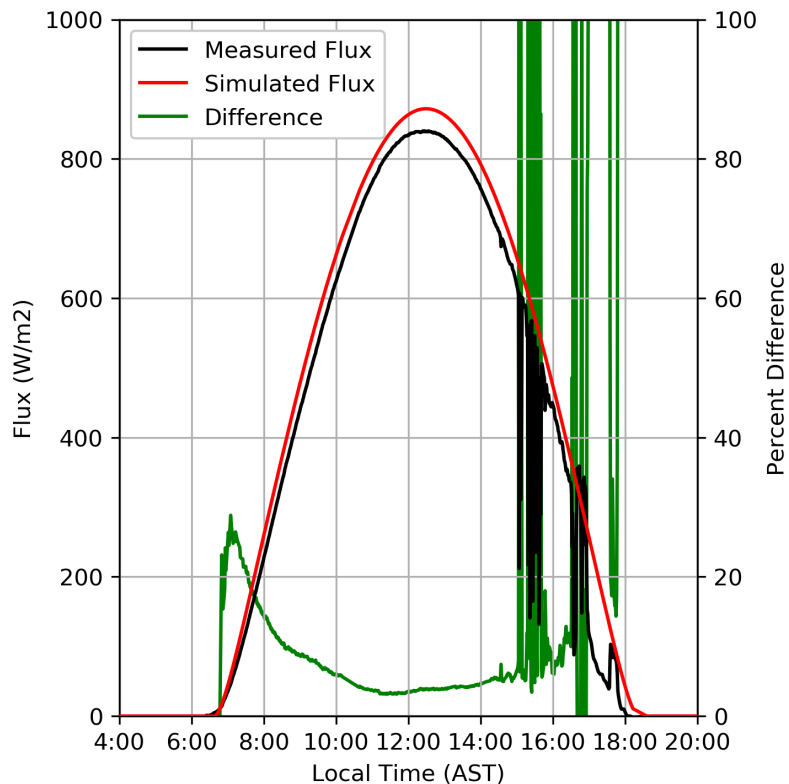


Figure 37: (Black) Measured and (red) simulated downwelling solar flux at the Bermuda AERONET site for 07 March 2009 along with (green) the percent difference between the two measurements.

simulations assume no cloud or aerosol is present, the nearby Tudor Hill AERONET site (32.264°N, 64.879°W, 51.0 m AMSL) reported an average 0.075 AOD at 500 nm for that day.

The measured and simulated downwelling solar fluxes at Bermuda are shown in Fig. 37 along with the percent difference between the two. Relatively large differences of near 30% are evident at sunrise, though this corresponds to a very small absolute flux difference. Near solar noon, larger absolute differences of up to $50 \frac{W}{m^2}$ are visible, however, relative difference is below 5%. Later in the afternoon, near 15:00 AST (19:00 UTC), clouds begin to pass over the site and large absolute and relative differences are evident. Despite all simulations resulting in differences, when

clear-skies are present, the flux simulations are very consistent with observations. Further, while FLG calculated flux is slightly higher than measured, this may be due to the presence of aerosols or thin cirrus which have not been included in the FLG simulations. As such, the results are consistent with observations and the system is correctly compiled and configured.

4.3.2 Determining Study Window

To attempt radiative closure in the presence of aerosols, it is best to limit the study window to a time in which aerosol was present without cloud over an easily characterized surface. Further, limiting the study window to the first transect allows information from both aircraft to be used. For instance, during the first transect, the DC-8 is flying within the aerosol plume. As such, nephelometer observations can be examined along with flux measurements in both the upwelling and downwelling directions that should be affected by the aerosol, and lidar extinction profiles from the CPL on the ER-2.

The study window is chosen visually using the co-located DIAL-HSRL and CPL backscatter curtain plots for the first transect as shown in Fig. 38. The study window chosen is indicated by the times between two black vertical lines. During this window, the plume is present over the open ocean without any other cloud.

4.3.3 Interpolation

Not only are the aircraft not flying in perfect tandem in time, the observations from the variety of instruments on each aircraft are provided at a variety of different temporal and vertical resolutions. Temporally, all observations have been interpolated linearly by time to the 1 s resolution aircraft navigational data (i.e., latitude, longitude, and altitude). Spatially, observations from the ER-2 aircraft are interpolated

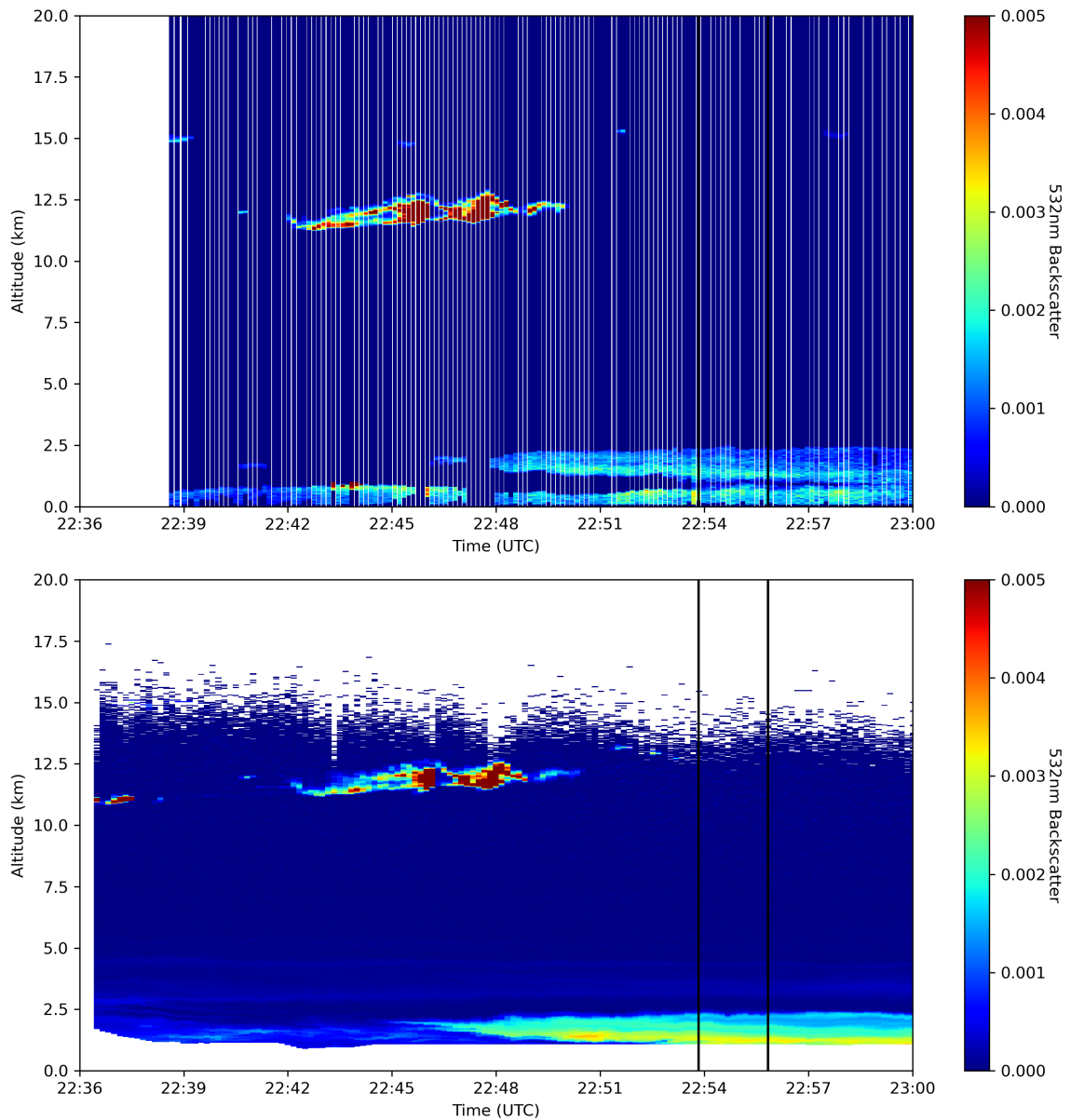


Figure 38: (Bottom) Upward looking DIAL-HSRL and co-located (top) downward looking CPL backscatterer curtains from the first transect of the dust plume in the northern Gulf of Mexico with the chosen study window indicated by vertical black lines. The altitudes of the aircraft are approximately 0.5 km for the DC-8 and 18 - 20 km for the ER-2 (see Fig. 34)

to the DC-8 locations with maximum observation distance limited to 10 km, though all observations within the study period co-locate within 1 km.

Vertically, the meteorological profiles from GEOS-5 and the aerosol extinction from CPL and DIAL-HSRL are interpolated linearly by altitude to the 30 m DIAL-HSRL levels. Finally, above the top DIAL-HSRL level, the higher GEOS-5 meteorological levels are appended. This ensures the FLG simulations contain information above the troposphere. For these vertical levels, aerosol extinction is assumed zero. This results in a total of 701 vertical layers and 1 surface layer.

4.3.4 Aerosol Extinction Profiles

The study window is during the first transect, and thus, the DC-8 is within the dust plume such that observations of the plume from the DIAL-HSRL are limited. Since aerosol extinction is not available for the entire aerosol plume from DIAL-HSRL, the observed extinction profile from the CPL is used. For the study window, the CPL lidar ratio was determined using the unconstrained or default value of 35.0 sr for dust mixture. For a more accurate aerosol profile, the extinction from CPL is corrected using the lidar ratio retrieved from the DIAL-HSRL during the third transect where the DC-8 is far enough above the aerosol plume that the entire plume is observed by the DIAL-HSRL. Specifically, only the lidar ratio within the dust plume for profiles within 1 km of the study window are averaged. This averaging window is shown as the block box near the surface between 85300 and 85400 s in Fig. 39. The averaged dust plume lidar ratio from the DIAL-HSRL for the third transect is 51.49 sr. As such, the CPL aerosol extinction is increased by a factor of $51.49/35.00$ to create a more accurate extinction profile.

Aerosol extinction profiles from the GEOS-5 binned dust mixing ratios are determined for comparison with observations and FLG flux and heating rate calculations.

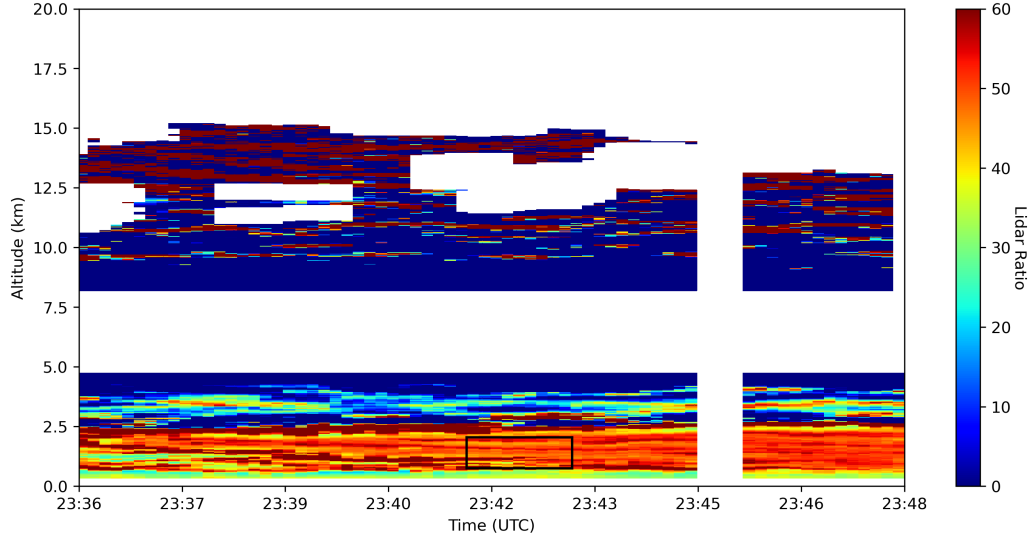


Figure 39: Both upward and downward pointed DIAL-HSRL extinction-to-backscatter ratio during the third transect. The averaging window for the lidar ratio within 1 km of the study window and within the aerosol layer is indicated by the black box. During this transect, the DC-8 was at an altitude of approximately 6.5 km.

The process of converting from dust mass mixing ratio to extinction is performed for both the OPAC and Tegen and Lacis (1996) optical models. For the Tegen and Lacis (1996) model, the mass extinction efficiency is calculated for each of the five GEOS-5 models using the optical depth and mass loading values reported by Table 1 in Tegen and Lacis (1996). The extinction coefficient is then calculated from the mass extinction efficiency and the GEOS-5 calculated mass concentrations where mass concentrations are calculated using the ideal gas law. Specifically:

$$M_c = \omega \cdot \frac{R_d \cdot T}{P}, \quad (4.2)$$

where M_c is the calculated aerosol mass concentration, ω is the aerosol mass mixing ratio, R_d is the dry air gas constant, T is the layer temperature, and P is the layer pressure. For the OPAC optical model, the GEOS-5 calculated aerosol mass concen-

trations are multiplied by the mass extinction efficiency for the OPAC dust model with nearest effective radius to the GEOS-5 bin. The OPAC dust mass extinction efficiencies are determined using the OPAC database. Note, for both the OPAC and Tegen and Lacis (1996) optical models, by using mass extinction efficiency for the aerosol size closest to the GOCART aerosol bin, the dust size distribution is at least partially accounted for in the optical parameterization.

4.3.5 Comparing PiNeph Measurements

The PiNeph data files include aerosol size distribution, scattering coefficient, single scattering albedo, and asymmetry parameter at 473, 532, and 671 nm. To compare the observed dust properties from PiNeph to those from the OPAC and Tegen and Lacis (1996) optical models, PiNeph extinction efficiency needs to be determined. The extinction efficiency is calculated as:

$$Q_{ext,\lambda} = \frac{4}{\pi} \cdot \frac{\beta_{s,\lambda}}{SSA_\lambda} \cdot \left(\sum_{i=1}^{n_{bins}} N_i \cdot r_i^2 \right)^{-1}, \quad (4.3)$$

where $\beta_{s,\lambda}$ is the reported scattering coefficient at wavelength λ , SSA_λ is the reported single scattering albedo at wavelength λ , r_i is the midpoint of the reported size distribution bins, and N_i is the number of particles within that size distribution bin. The number of particles is determined from the following relationship:

$$N_i = \left(\frac{dN}{dLog(r)} \right)_i \cdot \ln \left(\frac{r_{i,max}}{r_{i,min}} \right), \quad (4.4)$$

where $\left(\frac{dN}{dLog(r)} \right)_i$ is the reported size distribution for bin i , and $r_{i,max}$ and $r_{i,min}$ are the maximum and minimum radii in bin i . Finally, the broadband extinction efficiency is calculated by performing a weighted average for the extinction efficiency at the three wavelengths using the solar irradiance curve from Wehrli (July 1985). Similarly the

broadband asymmetry parameter is calculated using the product of the scattering efficiency determined from the single scattering albedo and extinction efficiency at each wavelength and the solar irradiance curve.

As mentioned above, the FLG aerosol look-up-tables do not include extinction efficiency but a spectrally normalized extinction value. Thus, to compare the PINeph extinction efficiency calculated above to the Tegen and Lacis (1996) or OPAC optical models, extinction efficiency for these models must be determined. For the Tegen and Lacis (1996) optical model, the extinction efficiency for the effective radii used by FLG are computed by interpolating the extinction efficiencies reported by Table 1 in Tegen and Lacis (1996). For OPAC, the extinction efficiency is derived from the OPAC dust particle density, the dust mass, the dust number concentration, and the dust extinction coefficient at 450, 500, 550, 600, 650, and 700 nm. First, the effective radius of each dust type is determined from the mass and density:

$$r_{eff,i} = \left(\frac{m_i}{\rho_i} \cdot \frac{3}{4\pi} \right)^{\frac{1}{3}}, \quad (4.5)$$

where $r_{eff,i}$ is the effective radius of the dust model i , m_i is the dust particle mass, and ρ_i is the dust particle mass density. Then, from the extinction coefficient and number concentration, the extinction efficiency can be derived from the following relationship:

$$Q_{ext,i} = \frac{\beta_{ext,i}}{N_{c,i} \cdot \pi \cdot \left(\frac{3 \cdot m_i}{4 \cdot \pi \cdot \rho_i} \right)^{\frac{2}{3}}}, \quad (4.6)$$

where $Q_{ext,i}$ is the extinction efficiency of the dust model i , $\beta_{ext,i}$ is the extinction coefficient for dust model i , and $N_{c,i}$ is the number concentration of the dust model i . Finally, the broadband asymmetry parameter is solved using the weighted averaged scattering efficiency at each wavelength and solar irradiance curve, and the broadband single scattering albedo and extinction efficiency are computed using

the solar irradiance curve. Note, these relationships assume the dust aerosols are spherical, consistent with the development of the OPAC database (Hess et al., 1998). Finally, the single scattering albedo and asymmetry parameter for the Tegen and Lacis (1996) model are retrieved from the FLG source code for the first solar band.

4.4 Results

4.4.1 Optical Property Comparison

The broadband optical properties measured by the PINeph during the first transect are plotted along with the optical properties of the different models from OPAC and Tegen and Lacis (1996) in Fig. 40. Large variability in observations is seen throughout the transect. Observed extinction efficiency ranges from near 0.8 to near 1.25, single scattering albedo ranges from near 0.65 to 0.80, and asymmetry parameter ranges from near 0.60 to near 0.90. Interestingly, the extinction efficiency is lower than that of any of the OPAC or Tegen and Lacis (1996) models. This may be due to uncertainties in the binning of the size distribution, specifically the use of the bin mid-point as the radius for all particles within that bin. If the particles within a bin are biased towards the smaller sizes, the calculated extinction efficiency will be higher. Specifically, in Eq. 4.3 the radius used here is the bin-mid point. If the actual mean radius within that bin was biased towards a smaller size, this term would decrease, increasing the overall extinction efficiency. This may also be due to uncertainties associated with the deriving of the size distribution using the GRASP software.

Despite the extinction efficiency discrepancies, the single scattering albedo and asymmetry parameters are largely within the bounds set by the prebuilt optical models. For instance, the single scattering albedo is often consistent with, or between the 1.0 and 4.0 μm dust models from Tegen and Lacis (1996) or the coarse-mode

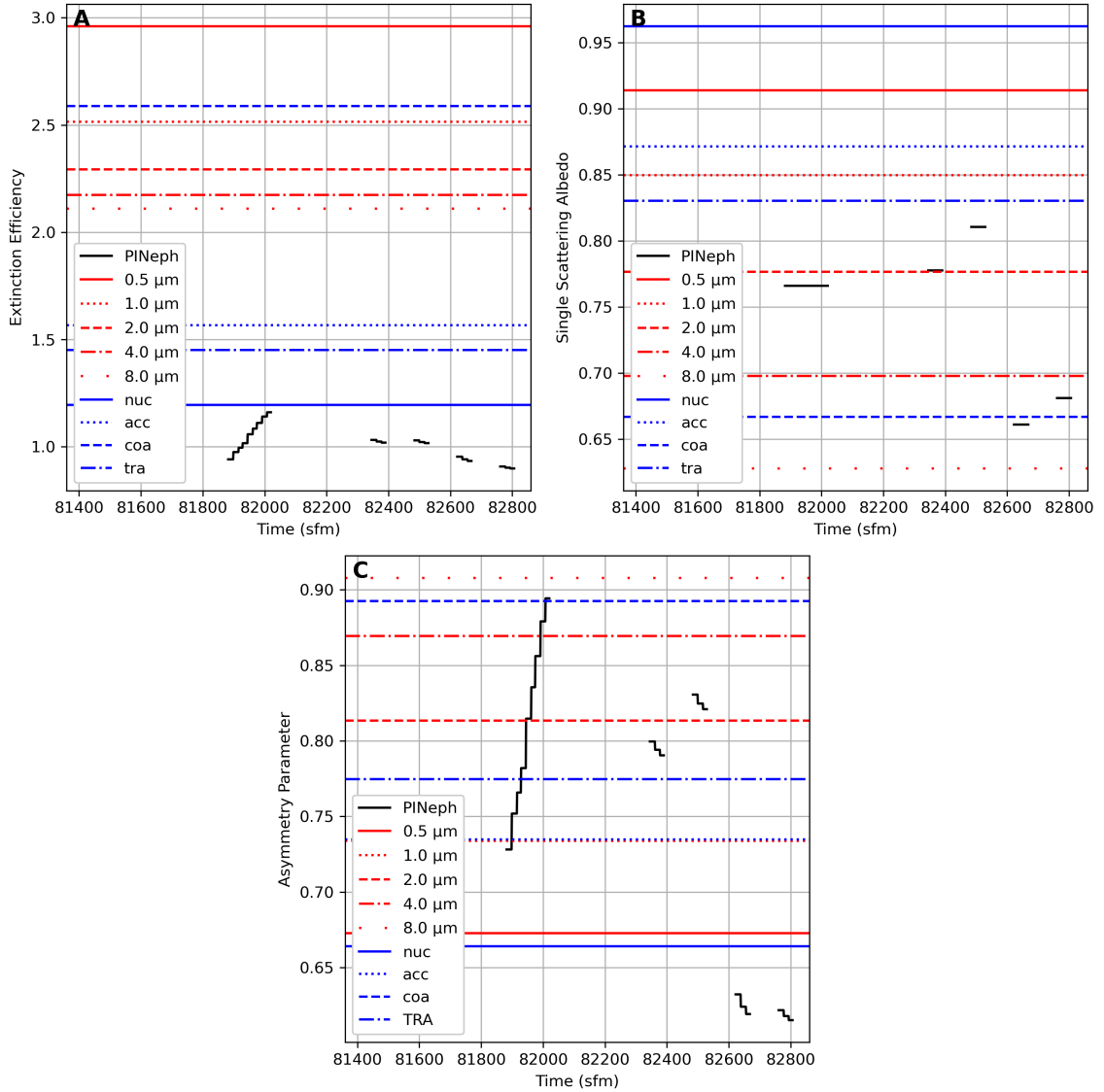


Figure 40: (Black) PINeph measured optical properties of broadband (A) extinction efficiency, (B) single scattering albedo, and (C) asymmetry parameter compared to the (blue) OPAC and (red) Tegen and Lacis (1996) dust optical models.

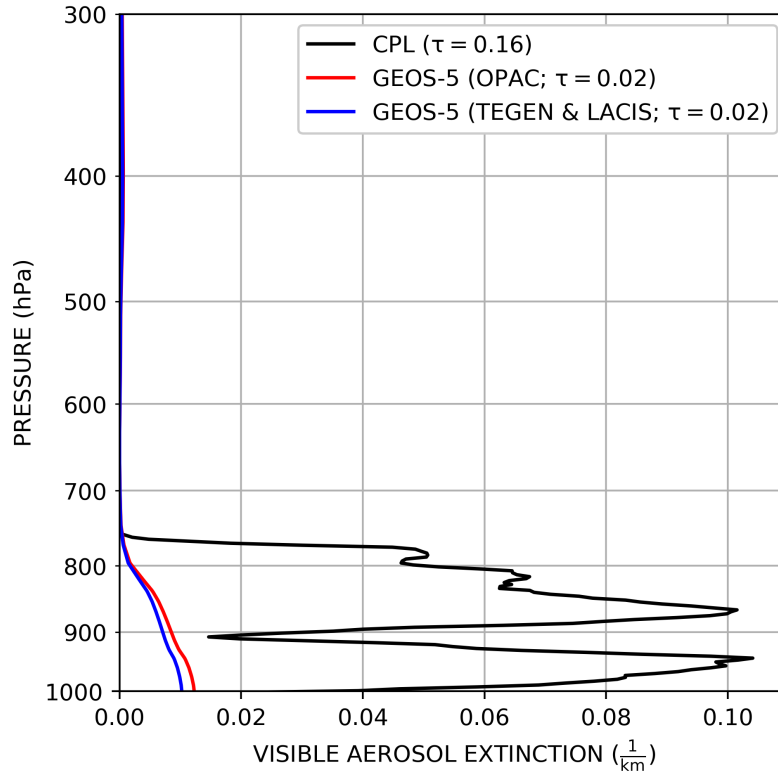


Figure 41: Dust extinction profiles from (black) CPL, (red) GEOS-5 using the OPAC optical model, and (blue) GEOS-5 using the Tegen and Lacis (1996) optical model for the study window.

and transported-mode dust models from OPAC. For the asymmetry parameter, observations again range from 1.0 to 4.0 μm dust from Tegen and Lacis (1996) and coarse-mode and transported-mode dust. Note, unlike the extinction efficiency, the single scattering albedo and asymmetry parameters are directly measured by the PINeph. Interestingly, there is variability throughout the transect even after the aircraft is well within the dust plume (i.e., after 82400 sfm). This suggests that the aerosol plume may not be homogeneously mixed. In such a case, observations from the PINeph would not be representative of the entire plume.

4.4.2 Aerosol Extinction Profiles

The study-window-averaged aerosol extinction profile from the DIAL-HSRL-lidar-ratio-corrected CPL extinction profile is plotted alongside the GEOS-5 aerosol extinction profiles calculated using the OPAC and Tegen and Lacis (1996) optical models in Fig. 41. The observed extinction pattern from CPL presents much more aerosol loading than those calculated from the GEOS-5 dust mass mixing ratio. For instance, the AOD from the CPL observations corrected with the DIAL-HSRL lidar ratio is 0.16, whereas the GEOS-5 analysis using either optical model exhibit an AOD of 0.02. Consistent with the backscatter observations shown in Fig. 38, the CPL extinction profile shows what appear to be two aerosol layers, one between the surface and 900 hPa, the between 900 and 750 hPa. While the presence of these two layers may suggest that these two layers exhibit differing optical properties, the lidar ratio (see Fig. 39) for both layers are very consistent suggesting similar aerosol properties. Interestingly, the rather homogeneous lidar ratio is also inconsistent with the variable measurements from the PINeph, though further investigation into this facet is not performed here.

For the GEOS-5 analysis in particular, near-but-non-zero aerosol loading exists in the mid-to-upper troposphere between 300 and 500 hPa. This higher altitude aerosol was not detected by the lidar and is not immediately visible in either the DIAL-HSRL or the CPL backscatter, suggesting this upper level aerosol to be a GEOS-5 feature only. In fact, comparisons between aerosol vertical distribution from CALIOP show MERRA (based upon GEOS) and GOCART exhibit low biases near the surface and high biases aloft (Koffi et al., 2016). As such, this artifact is unlikely to be an issue with observations, but biases consistent with the aerosol model.

4.4.3 Flux Comparison

The FLG calculated fluxes for the different OPAC and Tegen and Lacis (1996) optical models are shown in Fig. 42. The clear-sky downwelling solar flux (shown by the black line in Fig. 42A), is calculated using the GEOS-5 reanalysis atmosphere with no aerosol loading, and ranges from near $430 \frac{\text{W}}{\text{m}^2}$ at the surface to near $480 \frac{\text{W}}{\text{m}^2}$ at 700 hPa. Using the observed extinction profile, the downwelling solar flux is decreased throughout the aerosol layer from the surface to near 800 hPa. The downwelling solar flux based upon the GEOS-5 analyzed aerosol are also lower than the clear-sky flux, albeit from the surface to at least an altitude of 700 hPa. The deeper impact of aerosols for the GEOS-5 aerosol cases is not unexpected given the small aerosol loading in the middle-to-upper levels of the troposphere discussed above. Consistent with the lower AOD, the downwelling fluxes from the GEOS-5 aerosol analysis exhibit less impact within the aerosol layer than the fluxes using the observed extinction profile. Surprisingly, the GEOS-5 flux profile using the OPAC and Tegen and Lacis (1996) optical models are identical. That said, variability of up to $30 \frac{\text{W}}{\text{m}^2}$ exists between the range of OPAC and Tegen and Lacis (1996) optical models for the observed extinction profile.

Several of the aerosol optical models provide downwelling shortwave fluxes near the observed flux from the BBR on the DC-8 (given by the black star). Note, for the measured downwelling solar flux of $408.7 \frac{\text{W}}{\text{m}^2}$, the uncertainty in BBR of 3-5% corresponds to approximately $\pm 10 - 20 \frac{\text{W}}{\text{m}^2}$. As such, any of the simulations exhibiting fluxes between approximately 390 and $430 \frac{\text{W}}{\text{m}^2}$ are consistent with the observed flux. All optical models fall within this range, with only the simulations. That said, the calculations using the GEOS-5 aerosol analysis is outside of this range. These GEOS-5 cases falling outside the range of fluxes consistent with observations is unsurprising

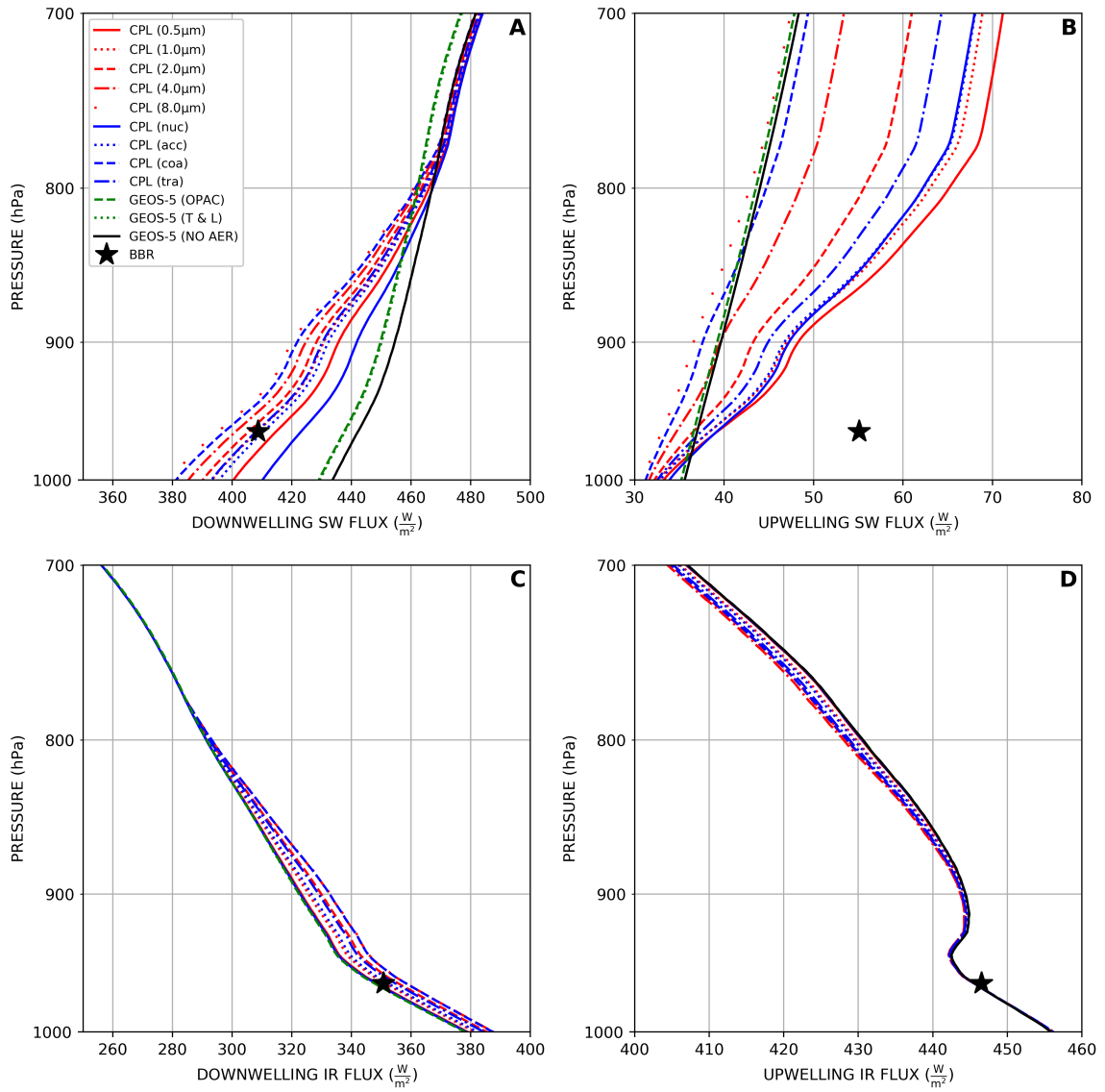


Figure 42: (A) Downwelling, (B) upwelling shortwave flux and (c) downwelling and (d) upwelling IR flux as a function of altitude calculated using FLG with the CPL extinction profile for (red) each of the Tegen and Lacis (1996) and (blue) OPAC dust optical models. Also shown are fluxes for the (green) GEOS-5 aerosol analyses for each of the optical models and (black) aerosol-free fluxes. The BBR flux measurements are shown at the aircraft altitude as a black star.

given the extremely low AOD from the GEOS-5 aerosol analyses. That said, that this analyzed aerosol profile cannot provide accurate downwelling flux is concerning.

There is much more relative variability in the upwelling shortwave flux as a function of aerosol optical model (Fig. 42B). The fluxes calculated using the observed extinction with the OPAC and Tegen and Lacis (1996) optical models range from near the clear sky value of 43 to near $65 \frac{\text{W}}{\text{m}^2}$ at 800 hPa (near the top of the aerosol plume). All values are greater the clear-sky case at altitudes above 800 hPa, and all optical models exhibit fluxes under the clear-sky beneath near 980 hPa. The increased upwelling shortwave flux above the aerosol is due to the increased solar reflection off the aerosols, whereas the decreased flux near the surface is due to less downwelling flux reaching the surface. Interestingly, the upwelling flux using the GEOS-5 aerosol analysis is nearly identical to the clear-sky case likely due to the much lower aerosol loading.

Despite the large relative range in upwelling solar flux for the different aerosol optical models, none of the simulations come near to matching the BBR observation of $55.11 \frac{\text{W}}{\text{m}^2}$. Different broadband surface albedos and AODs were attempted to rectify these differences. For the same AOD, the albedo needs to be roughly 0.30, which is highly unrealistic for ocean water, and unlikely given the derived albedos in Fig. 35. The instrument principle investigator analyzed the data and examined the cameras on the aircraft before determining the observation was likely contaminated by solar glint off of the ocean surface. While the aircraft was not directly over a glint region, glint is visible off-nadir in the aircraft camera. Since the BBR measures hemispheric flux, the presence of off-nadir glint likely contaminated the observations (Anthony Bucholtz, *personal communication, July 2020*). It is important to note that the upwelling flux values simulated here are similar to those reported by Jin et al. (2002) using observations collected at the CERES Ocean Validation Experiment COVE site.

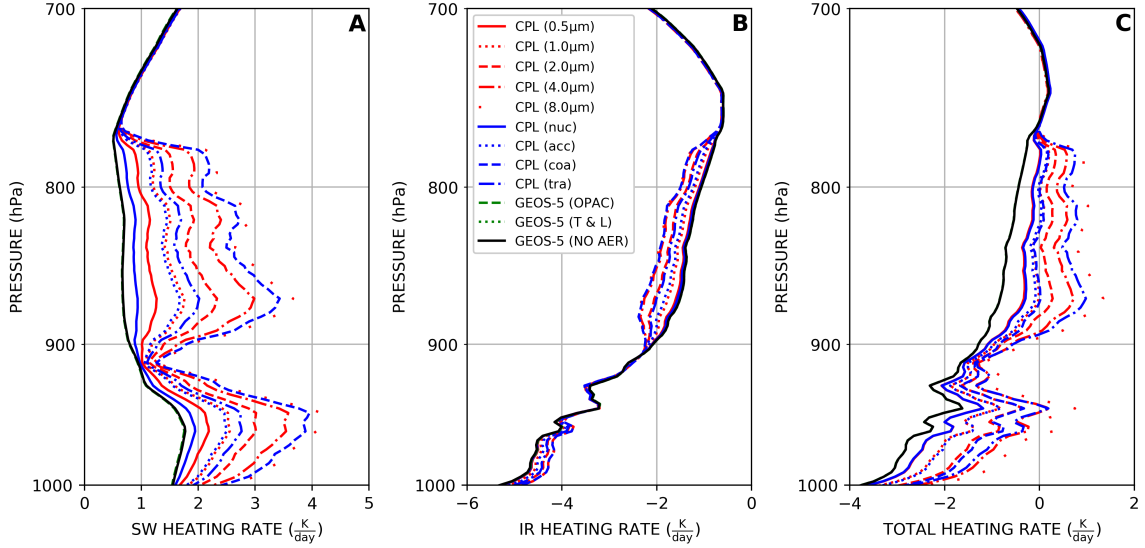


Figure 43: As in Fig. 42, but for (A) shortwave heating rate, (B) IR heating rate, and (C) total heating rate.

In the IR, the aerosol impact and the variability of optical model is much less than in the shortwave. For instance, the aerosol impact on downwelling IR flux (Fig. 42C) versus the clear-sky simulation maximizes at 900 hPa near $15 \frac{\text{W}}{\text{m}^2}$ or below 5%. Meanwhile, for the upwelling IR flux (Fig. 42D) aerosol impact peaks below $5 \frac{\text{W}}{\text{m}^2}$, or below 2%. Compared to the BBR observation, both upwelling and downwelling flux simulations for all the aerosol models *and the clear-sky simulation* are within the BBR uncertainty. As such, the impact of aerosol and aerosol optical model in the shortwave is much more pronounced. That said, this may not be the case for larger aerosol loadings. Regardless, the observed aerosol profile results in radiative closure in both the IR and shortwave.

4.4.4 Heating Rate Comparison

The FLG calculated radiative heating rates consistent with the fluxes above are shown in Fig. 43. The radiative heating rate is the rate of change of temperature in a layer

due absorption and emission of radiation within that layer and can be calculated using the following relationship from Quijano et al. (2000):

$$\frac{dT}{dt} = \frac{g \cdot \nabla F_{tot}}{c_p \cdot dP}, \quad (4.7)$$

where $\frac{dT}{dt}$ is the layer heating rate in Kelvin per second, g is the acceleration of gravity in meters per second, ∇F_{tot} is the vertical gradient in total (i.e., shortwave plus IR) flux in Watts per meter squared per pascals, C_p is the specific heat of air at constant pressure in Joules per kilogram, and dP is the change in pressure over the layer in pascals (Quijano et al., 2000). That said, this relationship is not directly implemented by the author, as FLG directly reports these heating rates.

Clear-sky solar heating is evident throughout the lower atmosphere at rates of near 1 to 2 $\frac{K}{day}$ (Fig. 43A). When the observed aerosol profile is used, relatively large variability exists, though the impact of aerosol is consistently to increase the heating rate. For instance, the clear sky shortwave heating rate between 900 hPa and 800 hPa is near 0.8 $\frac{K}{day}$. The observed aerosol plume results in heating rates within the aerosol layer between 1.0 and 4.0 $\frac{K}{day}$. This solar warming occurring throughout the aerosol plume was also reported by Carlson and Benjamin (1980) for Saharan dust. As may be expected, the heating rates differ from the clear-sky most where extinction is highest. As such, the heating rates exhibit two areas of variability consistent with the two layers of aerosol shown in Fig. 41. Given that all aerosol optical models provide fluxes consistent with the observations, this 2.0 - 3.0 $\frac{K}{day}$ range is obviously concerning. Finally, as is consistent with little aerosol loading, the shortwave heating rate for the simulations with GEOS-5 analyzed aerosol is virtually identical to the non-aerosol case - also a concerning fact.

In the IR, the heating rate is always negative indicating IR cooling (Fig. 43B). The observed aerosol causes decreased cooling (i.e., relative heating) in the lower portions of the aerosol plume and an increased cooling in the upper portions of the aerosol plume again consistent with the results reported by Carlson and Benjamin (1980). The impact of the aerosol is relatively less than in the solar and the variability due to optical model is comparatively decreased. As before, the heating rates calculated using the GEOS-5 aerosol profile are nearly identical to the clear-sky rates.

When combined into a total heating rate (Fig. 43C), much of the lower atmosphere experiences cooling. In fact, the solar heating term can dominate the IR cooling term and force total heating in the upper layers of the dust plume, effectively changing the sign of the heating while maintaining similar magnitude. In the lower portions of the profile, only the OPAC coarse-mode and Tegen and Lacis (1996) 8.0 μm optical models are able to overcome the IR cooling to cause total warming. As such, there is substantial variability in heating rates due to optical model, primarily a result of the large variability in the shortwave term. Consistent with the IR and shortwave heating, the heating rates calculated using the GEOS-5 aerosol profile are again nearly identical to the clear-sky rates.

4.5 Discussion

Similar to Oyola et al. (2019), closure using observations was achieved. However, while Oyola et al. (2019) achieved closure for non-IR active aerosols, here closure was achieved in both the shortwave and IR spectrums given the caveat of glint contaminated upwelling shortwave flux. Also consistent with Oyola et al. (2019), the model analyzed aerosol profile was unable to recreate measured fluxes, presumably also resulting in inaccurate heating rates. This second point is of particular concern as NWP centers begin to integrate aerosols into their operational forecast systems.

Non-insignificant optical model variability is evident in both fluxes and heating rates. While the variability is maximized in the shortwave, there is also variance in the IR fluxes and heating rates. That variability exists between models at similar sizes is likewise concerning, especially for aerosol property retrievals based upon these models. Additionally, this variability, presents an additional source of uncertainty for NWP incorporating aerosol radiative effects. Particularly, even if predicted AOD were perfect, uncertainties would exist due to assumed optical model, including refractive index, shape, size distribution, etc. (e.g., Song et al., 2018).

Finally, the optical models were examined for a Saharan dust layer that had been advected across the Atlantic and Caribbean. Given both the OPAC and Tegen and Lacis (1996) optical models are based upon observations of Saharan dust, while the models achieve closure here, the models may not be applicable in other dusty regions (e.g., Asia and Australia). Further, this case also exhibited relatively low AOD, especially considering dust AOD often exceeds 1.0 in the Eastern Tropical Atlantic. As such, future studies should examine other geographical regions.

CHAPTER 5

SUMMARY AND CONCLUSIONS

Numerical weather prediction (NWP) is an initial value problem, where an initial atmospheric state is integrated forward in time to provide forecasts. It is vitally important that this initial atmospheric state be as accurate as possible since errors in the initial state will grow rapidly with forecast time. One common method to ensure the initial atmospheric state is highly accurate is the process of data assimilation. Data assimilation is the process of merging a previous model forecast with observations in such a way to minimize error associated with both the forecast and the observations.

Recently, the assimilation of hyperspectral infrared sounder (HIS) radiances has resulted in the most significant decreases in NWP forecast error of all assimilated satellite products. Assimilating HIS radiances allows for updating of forecast humidity and temperature vertical profiles and, as such, is highly useful in regions without conventional observations (e.g., oceans). Accordingly, all major operational NWP centers assimilate HIS radiances and several agencies have made HIS sensors core to future satellite missions. Assimilation of HIS radiances is typically reserved to clear-sky observations, however.

To ensure HIS radiances are collected from clear-sky scenes, assimilation systems perform several checks on the observed radiances to detect aerosol and cloud contamination. These checks examine the difference between the observed radiances and simulated radiances based upon the forecast atmosphere. If these differences are above a specific threshold or there are discontinuities in the differences consistent with

cloud or aerosol, all biased radiances are rejected. That said, given significant aerosol and cloud contamination in have been identified in many other satellite radiometric products that include other information for cloud screening such as visible radiances. As such, cloud and aerosol contamination of assimilated HIS radiances is expected.

Using co-located aerosol analyses and cloud observations residual aerosol and cloud is found in HIS observations assimilated by the Naval Research Laboratory Data Assimilation System (NAVDAS) from the Cross-track infrared sounder (CrIS), the Infrared Atmospheric Sounding Interferometer (IASI), and the Atmospheric Infrared Sounder (AIRS) sensor. Aerosol contamination rates of 30 - 35% for visible aerosol optical depths (AOD) of 0.1 were found. Similarly, cirrus cloud contamination rates of near 8% were found. Using the Radiative Transfer for TOVS (RTTOV) radiative transfer model (RTM) it was found that observations with AODs above 0.3 and cloud optical depths (CODs) near 0.1 could pass the screening methods. Using a one-dimensional variational (1DVar) assimilation system, the impact on analyzed temperature and humidity profiles due to assimilating cloud and aerosol contaminated HIS radiances is estimated.

The impact of dust contaminated HIS radiances is estimated using a series of 97 coincident aerosol, temperature, and humidity profiles collected from the island of Tenerife, Spain in the Canary Islands. Simulated dust-contaminated HIS radiances for the CrIS sensor creating using these observed profiles are assimilated and, since the atmosphere used to create the observations is known, the analysis bias can be determined. For the 97 profiles, the average temperature and dew point temperature biases peaked near 0.5 K and 1.0 K with large standard deviations, respectively. Both values are of similar magnitude of the expected forecast error. Larger maximum temperature and dew point biases of 2.6 K and 8.5 K exist for observations contaminated by an AOD of 1.0. Despite these biases, when an imperfect forecast is used as

background during assimilation, even the assimilation of biased radiances results in a better analysis than no assimilation at all. That said, this may not always be the case. Further, when the aerosol profile is decoupled from the radiances, the analysis is consistently better than when the observations are assumed uncontaminated.

For the impact of assimilating cirrus contaminated HIS radiances, a similar experiment is developed. However, instead of using observations to create synthetic CrIS observations, a standard tropical atmosphere is merged with clouds of varying COD and cloud top temperature/altitude to create a total of 301 atmospheres with a single cloud layer, and 1 clear sky atmosphere. The assimilation of these cirrus contaminated HIS radiances results in extremely large analysis biases. For instance for a cloud at a temperature of 210 K with a COD of 0.10, maximum temperature bias may be as high as 3 K while dew point bias is near 10 K. The column root mean squared errors (RMSEs) are similarly concerning at 3 K and 5 K for temperature and dew point, respectively. These RMSEs indicate the large analysis bias throughout the entire troposphere. As such, these errors are extremely concerning given the expected forecast error and contamination rate.

Given that errors in the initial atmospheric state grow rapidly with time, these aerosol and cloud-induced biases are particularly concerning. That said, these estimates are likely on the high-end since a wide array of observations are usually assimilated. As such, the estimates shown here are likely only to appear in the special case where only contaminated HIS radiances are available. Concerningly, because tropical cyclones that impact land often form or transient remote oceans where both optically thin cirrus clouds and dust are frequent, assimilation of contaminated HIS radiances may present an unrealized noise in tropical cyclone forecasting.

Recently, operational centers have begun to experiment with assimilating radiances in regions with cloud, but these efforts treat clouds simply and are unlikely

to remove biases due to unscreened cirrus clouds. For example, McNally (2009) and Okamoto (2013) presented two experiments with cloudy-sky IR assimilation. While both studies found statistically significant increases in analysis and forecast accuracy, both only examined overcast scenes. As mentioned, the treatment of cloud was extremely simplistic, effectively ignoring optical differences between clouds. Understanding the limitations of models in forecasting clouds, both studies modeled clouds using observations. While such a process may seem to be promising, it does not remedy the issue shown in Fig. 5 - clouds not observed in operations. Thus, even if the experiments above become standard practice, cirrus clouds may be missed and assimilated as clear-sky anyway.

In a separate study, the ability for NWP predicted aerosol fields to be used to recreate accurate radiative flux profiles and the impacts of different aerosol optical models on those fluxes is examined. Several operational NWP centers are transitioning their systems to include prognostic aerosols and aerosol radiative impacts. Similar, studies have shown the inclusion of aerosol radiative effects can result in substantially better weather forecasts. Despite these efforts accelerating recently, little verification has been performed of the predicted radiative effects, particularly those impacts away from the surface. Further, these systems usually implement pre-built optical models for practicality. Due to a limitation on the number and variability of these optical models, the chosen model may not always be applicable due to wide variability in aerosol composition (e.g., African versus Asian dust).

To examine the effects of aerosol optical model on flux simulations and determine the accuracy of predicted aerosol fields, radiative closure experiments are performed using observations collected during the Studies of Emissions and Atmospheric Composition, Clouds and Climate Coupling by Regional Surveys (SEAC⁴RS). Specifically, observations collected in and above a dust aerosol plume over the northern Gulf of

Mexico are used as input for the Fu-Liou-Gu (FLG) radiative transfer model using several commonly used dust optical models. Fluxes from the FLG simulations for the different dust optical models were compared to fluxes observed by broadband radiometers on the DC-8 aircraft. Relatively large variability exists between optical models in the shortwave spectrum, but in the IR, variability is much less. For instance, for the same visible extinction profile, downwelling shortwave flux variability of about $30 \frac{\text{W}}{\text{m}^2}$ is shown, corresponding to near 8%. Upward flux is even more variable with a similar range of near $30 \frac{\text{W}}{\text{m}^2}$ above the aerosol layer, corresponding to over 50%. In the IR however, variability was on the order of $5 - 10 \frac{\text{W}}{\text{m}^2}$ or less than 3%. Similar impacts were seen for heating rates, with large variability of up to 400% in the shortwave spectrum with relatively slight variability in the IR spectrum of near 25-50%. Finally, fluxes and heating rates are simulated using aerosol fields from the Goddard Earth Observing System, Version 5 (GEOS-5) NWP model. The GEOS-5 aerosol profile exhibits too little aerosol in the lower atmosphere compared to observations, which results in biases in both the fluxes and heating rates. In fact, due to very low GEOS-5 aerosol loading (AOD of 0.02), the simulated fluxes and heating rates were more comparable to the clear-sky simulations. That said, the case here only examined a single aerosol case with relatively low AOD (0.16) and examination of fluxes at higher loadings and different regions should be examined.

APPENDIX A

LIST OF ABBREVIATIONS

Table 3: List of Abbreviations

Abbreviation	Full Text
1DVar	One-Dimensional Variational Assimilation System
4A	Automatized Atmospheric Absorption Atlas
8CASM	8-Column Aggregated Ice With Severely Roughened Surface Optical Model
AERONET	AERosol ROBotic NETwork
AGCM	GEOS-5 Atmospheric General Circulation Model
AIRS	Atmospheric Infrared Sounder
AMSL	Above Mean Sea Level
AOD	Aerosol Optical Depth
BBR	Broadband Radiometers
CALIPSO	Cloud-Aerosol LiDAR and Infrared Pathfinder Satellite Observation
CALIOP	Cloud-Aerosol LiDAR with Orthogonal Polarization
CERES	Clouds and the Earth's Radiant Energy System
COAMPS	Navy's Coupled Ocean-Atmospher Mesoscale Prediction System

Continued on next page

Table 3 – continued from previous page

Abbreviation	Full Text
COD	Cloud Optical Depth
COVE	CERES Ocean Validation Experiment
CPL	Cloud Physics Lidar
CrIS	Cross-track Infrared Sounder
DOM	Discrete Ordinates Method
DWD	Deutscher Wetterdienst (German Weather Service)
ECMWF	European Centre for Medium Range Weather Forecasts
ESRL	NOAA Earth System Research Laboratory
EUMETSAT	European Organisation for the Exploitation of Meteorological Satellites
FLG	Fu-Liou-Gu Radiative Transfer Model
GDAS	Global Data Assimilation System
GEOS-5	Goddard Earth Observing System, Version 5
GERBILS	Geostationary Earth Radiation Budget Intercomparison of Long-wave and Shortwave radiation
GFS	Global Forecast System
GIIRS	Geostationary Interferometric Infrared Sounder
GMAO	NASA Global Modeling and Assimilation Office
HIRS	High resolution Infrared Sounder
HIS	Hyperspectral Infrared Sounder
HRRR	High Resolution Rapid Refresh Model
IASI	Infrared Atmospheric Sounding Interferometer
IR	Infrared

Continued on next page

Table 3 – continued from previous page

Abbreviation	Full Text
IRS	Infrared Sounder
JMA	Japanese Meteorological Agency
LiDAR	Light Detection and Ranging
MERRA-2	Modern-Era Retrospective analysis for Research and Applications, Version 2
MetOp	Meteorological Operational Satellites
MODIS	Moderate Resolution Imaging Spectroradiometer
MPL	Micro-Pulse Lidar
MPLNET	Micro-Pulse Lidar Network
MTG	Meteosat Third Generation
MTSAT-1R	Multifunctional Transport Satellite - 1R
NAAPS	Navy Aerosol Analysis and Prediction System
NASA	National Aeronautics and Space Administration
NAVDAS	Naval Research Laboratory Atmospheric Variational Data Assimilation System
NAVGENM	U.S. Navy Global Environmental Model
NCEP	National Centers for Environmental Prediction
NOAA	National Oceanic and Atmospheric Administration
NPP	National Polar-orbiting Partnership
NRB	Normalized Relative Backscatter
NRL	Naval Research Laboratory
NWP	Numerical Weather Prediction
NWP SAF	Numerical Weather Prediction Satellite Applications Facility

Continued on next page

Table 3 – continued from previous page

Abbreviation	Full Text
OPAC	Optical Properties of Aerosols and Clouds
OTC	Optically Thin Cirrus
PINeph	Polarized Imaging Nephelometer
QA	Quality Assured
QL	Quality Level
RMSE	Root Mean Squared Error
RTM	Radiative Transfer Model
RTTOV	Radiative Transfer for TOVS
SDA	Spectral Deconvolution Algorithm
SEAC ⁴ RS	Studies of Emissions and Atmospheric Composition, Clouds and Climate Coupling by Regional Surveys
SST	Sea Surface Temperature
Suomi-NPP	Suomi National Polar-orbiting Partnership
TOVS	TIROS Operational Vertical Sounder
WMO	World Meteorological Organization

REFERENCES

- Ahrens, C. D., and R. Henson, 2019: *Meteorology Today: An Introduction to Weather, Climate, and the Environment, Edition 12*. Cengage, 587 pp.
- Alfaro-Contreras, R., J. Zhang, J. S. Reid, and S. Christopher, 2017: A study of 15-year aerosol optical thickness and direct shortwave aerosol radiative effect trends using MODIS, MISR, CALIOP and CERES. *Atmos. Chem. Phys.*, **17**, 13 849–13 868, doi:10.5194/acp-17-13849-2017.
- Askelson, M. A., 2002: Kinematic, dynamic, and thermodynamic impacts of hook echo hydrometeors, including explorations into the utilization of polarimetric radar data. Ph.D. thesis, University of Oklahoma, 245 pp.
- Aumann, H. H., and R. J. Pagano, 1994: Atmospheric Infrared Sounder on the Earth observing system. *Opt. Eng.*, **33**, 776–785, doi:10.117/12.159325.
- Baldasano, J. M., A. Soret, M. Guevara, F. Martínez, and S. Gassó, 2013: Integrated assessment of air pollution using observations and modelling in Santa Cruz de Tenerife (Canary Islands). *Sci. Tot. Env.*, **473-474**, 576–588, doi:10.1016/j.scitotenv.2013.12.062.
- Bannister, R. N., 2008: A review of forecast error covariance statistics in atmospheric data assimilation. i: Characteristics and measurements of forecast error covariances. *Quart. J. Roy. Meteor. Soc.*, **134**, 1951–1970, doi:10.1002/qj.339.

- Baum, B. A., P. Yang, A. J. Heymsfield, C. G. Schmitt, Y. Xie, A. Bansemmer, Y. Hu, and Z. Zhang, 2011: Improvements in shortwave bulk scattering and absorption models for the remote sensing of ice clouds. *J. Appl. Meteor. Climatol.*, **50**, 1037–1056, doi:10.1175/2010JAMC2608.1.
- Bergthórsson, P., and B. R. Döös, 1955: Numerical weather map analysis. *Tellus*, **7**, 329–340, doi:10.1111/j.2153-3490.1955.tb01170.x.
- Bi, J., J. Huang, B. Holben, and G. Zhang, 2016: Comparison of key absorption and optical properties between pure and transported anthropogenic dust over East and Central Asia. *Atmos. Chem. Phys.*, **16**, 15 501–15 516, doi:10.5194/acp-16-15501-2016.
- Bi, L., and P. Yang, 2017: Improved ice particle optical property simulations in the ultraviolet to far-infrared regime. *J. Quant. Spectrosc. Radiat. Transfer*, **189**, 228–237, doi:10.1016/j.jqsrt.2016.12.007.
- Bloom, H., 2001: The Cross-Track Infrared Sounder (CrIS): A sensor for operational meteorological remote sensing. *Proc. IEEE 2001 Int. Geosci. Remote Sensing Symp.*, Sydney, Australia, IEEE, doi:10.1109/IGARSS.2001.976838.
- Brown, O. B., P. J. Minnet, R. Evans, E. Kearns, K. Kilpatrick, A. Kumar, R. Sikorski, and A. Závody, 1999: MODIS infrared sea surface temperature algorithm. version 2.0. Algorithm theoretical basis document, University of Miami, 91 pp.
- Bucholtz, A., D. L. Hlavka, M. J. McGill, S. Schmidt, P. Pilewskie, S. M. Davis, E. A. Reid, and A. L. Walker, 2010: Directly measured heating rates of a tropical subvisible cirrus cloud. *J. Geophys. Res. Atmos.*, **115**, D00J09, doi:10.1029/2009JD013128.

- Burton, S. P., R. A. Ferrare, M. A. Vaughan, A. H. Omar, R. R. Rogers, C. A. Hostetler, and J. W. Hair, 2013: Aerosol classification from airborne HSRL and comparisons with the CALIPSO vertical feature mask. *Atmos. Meas. Tech.*, **6**, 1397–1412, doi:10.5194/amt-6-1397-2013.
- Burton, S. P., and Coauthors, 2012: Aerosol classification using airborne High Spectral Resolution Lidar measurements - methodology and examples. *Atmos. Meas. Tech.*, **5**, 73–98, doi:10.5194/amt-5-73-2012.
- Campbell, J. R., D. L. Hlavka, E. J. Welton, C. J. Flynn, D. D. Turner, J. D. Spinhirne, V. S. Scott, and I. H. Hwang, 2002: Full-time, eye-safe cloud and aerosol lidar observation at Atmospheric Radiation Measurement program sites: Instruments and data processing. *J. Atmos. Oceanic Technol.*, **19**, 431–442, doi:10.1175/1520-0426(2002)019<0431:FTESCA>2.0.CO;2.
- Campbell, J. R., K. Sassen, and E. J. Welton, 2008: Elevated cloud and aerosol retrievals from micropulse lidar signal profiles. *J. Atmos. Oceanic Technol.*, **25**, 685–700, doi:10.1175/2007JTECHA1034.1.
- Campbell, J. R., M. A. Vaughan, M. Oo, R. E. Holz, J. R. Lewis, and E. J. Welton, 2015: Distinguishing cirrus cloud presence in autonomous lidar measurements. *Atmos. Meas. Tech.*, **8**, 435–449, doi:10.5194/amt-8-435-2015.
- Campbell, J. R., and Coauthors, 2018: Unusually deep wintertime cirrus clouds observed over the Alaska Subarctic. *Bull. Amer. Meteorol. Soc.*, **99**, 27–32, doi:10.1175/BAMS-D-17-0084.1.
- Campbell, J. R., and Coauthors, 2021: Cirrus cloud top-of-the-atmosphere net daytime forcing in the Alaskan Subarctic from ground-based MPLNET monitoring. *J. Appl. Meteor. Climatol.*, **60**, 51–63, doi:10.1175/JAMC-D-20-0077.1.

- Carlson, T. N., and S. G. Benjamin, 1980: Radiative heating rates for Saharan dust. *J. Atmos. Sci.*, **37**, 193–213, doi:10.1175/1520-049(1980)037<0193:RHRFSD>2.0.CO;2.
- Carson-Marquis, B. N., J. Zhang, P. Xian, J. S. Reid, and J. Marquis, 2021: Improving WRF-Chem meteorological analyses and forecasts over polluted regions by incorporating NAAPS aerosol analyses. *J. Appl. Meteor. Climatol.*, **60**, 839–855, doi:10.1175/JAMC-D-20-0174.1.
- Chew, B. N., J. R. Campbell, J. S. Reid, D. M. Giles, E. J. Welton, V. Salinas, and S. C. Liew, 2011: Tropical cirrus cloud contamination in sun photometer data. *Atmos. Environ.*, **45**, 6724–6731, doi:10.1016/j.atmosenv.2011.08.017.
- Clothiaux, E. E., G. G. Mace, T. P. Ackerman, T. J. Kane, J. D. Spinhirne, and V. S. Scott, 1998: An automated algorithm for detection of hydrometeor returns in micropulse lidar data. *J. Atmos. Oceanic Technol.*, **15**, 1035–1042, doi:10.1175/1520-0426(1998)015<1035:AAAFDO>2.0.CO;2.
- Cullis, P., C. Sterling, E. Hall, A. Jordan, B. Johnson, and R. Schnell, 2017: Pop goes the balloon!: What happens when a weather balloon reaches 30,000 m asl? *Bull. Amer. Meteor. Soc.*, **98**, 216–217, doi:10.1175/BAMS-D-16-0094.1.
- Daley, R., 1991: *Atmospheric Data Analysis*. Cambridge University Press, 457 pp.
- Desroziers, G., L. Berre, B. Chapnik, and P. Poli, 2005: Diagnosis of observation, background and analysis-error statistics in observation space. *Quart. J. Roy. Meteor. Soc.*, **131**, 3385–3396, doi:10.1002/qj.05.108.
- Doicu, A., F. Schreier, and M. Hess, 2002: Iteratively regularized Gauss-Newton method for atmospheric remote sensing. *Computer Physics Communications*, **2**, 201–226, doi:10.1016/S0010-4655(02)0055-6.

- Dubovik, O., and Coauthors, 2014: GRASP: a versatile algorithm for characterizing the atmosphere. *SPIE: Newsroom*, doi:10.1117/2.1201408.005558.
- Eddy, A., 1967: The statistical objective analysis of scalar data fields. *J. Appl. Meteor. Climatol.*, **6**, 597–609, doi:10.1175/1520-0450(1967)006<0597:TSOAOS>2.0.CO;2.
- Ehrendorfer, M., 1997: Predicting the uncertainty of numerical weather forecasts: a review. *Meteorologische Zeitschrift*, **6** (4), 147–183, doi:10.1127/metz/6/1997/147.
- Espinosa, W. R., and Coauthors, 2019: Retrievals of aerosol size distribution, spherical fraction, and complex refractive index from airborne in situ angular light scattering and absorption measurements. *J. Geophys. Res. Atmos.*, **124**, 7997–8024, doi:10.1029/2018JD030009.
- Eyre, J., 1991: A fast radiative transfer model for satellite sounding systems. Technical memorandum, ECMWF, 30 pp. doi:10.21957/xsg8d92y3.
- Eyre, J. R., G. A. Kelly, A. P. McNally, E. Andersson, and A. Persson, 1993: Assimilation of TOVS radiance information through one-dimensional variational analysis. *Quart. J. Roy. Meteor. Soc.*, **119**, 1427–1463, doi:10.1002/qj.49711951411.
- Falkovich, A. H., E. Ganor, Z. Levin, P. Formenti, and Y. Rudich, 2001: Chemical and mineralogical analysis of individual mineral dust particles. *J. Geophys. Res. Atmos.*, **106**, 18 029–18 036, doi:10.1029/2000JD900430.
- Fernald, F. G., 1984: Analysis of atmospheric lidar observations. *Appl. Opt.*, **23**, 652–653, doi:10.1364/AO.23.000652.
- Francis, P. N., A. Jones, R. W. Saunders, K. P. Shine, A. Slingo, and Z. Sun, 1994: An observational and theoretical study of the radiative properties of cir-

- rus: Some results from ICE'89. *Quart. J. Roy. Meteor. Soc.*, **120**, 809–848, doi: 10.1002/qj.49712051804.
- Fu, Q., and K. N. Liou, 1992: On the correlated k -distribution method for radiative transfer in nonhomogeneous atmospheres. *J. Atmos. Sci.*, **49**, 2139–2156, doi: 10.1175/1520-0469(1992)049<2139:OTCDMF>2.0.CO;2.
- Fu, Q., and K. N. Liou, 1993: Parameterization of the radiative properties of cirrus clouds. *J. Atmos. Sci.*, **50**, 2008–2025, doi:10.1175/1520-0469(1993)050<2008:POTRPO>2.0.CO;2.
- Fu, Q., T. J. Thorsen, J. Su, J. M. Ge, and J. P. Huang, 2009: Test of Mie-based single-scattering properties of non-spherical dust aerosols in radiative flux calculations. *J. Quantitative Spectroscopy and Radiative Transfer*, **110**, 1640–1653, doi: 10.1016/j.jqsrt.2009.03.010.
- Gelaro, R., and Coauthors, 2017: The Modern-Era Retrospective Analysis for Research Applications, version 2 MERRA-2. *J. Climate*, **30**, 5419–5454, doi: 10.1175/JCLI-D-16-0758.1.
- Gilchrist, B., and G. P. Cressman, 1954: An experiment in objective analysis. *Tellus*, **6**, 309–318, doi:10.1111/j.2153-3490.1954.tb01126.x.
- Ginoux, P., M. Chin, I. Tegen, J. M. Prospero, B. Holben, O. Dubovik, and S. J. Lin, 2001: Sources and distributions of dust aerosols simulated with the GOCART model. *J. Geophys. Res. Atmos.*, **106**, 20 255–20 273, doi:10.1029/2000JD000053.
- Gray, W. M., 1975: Tropical cyclone genesis. Atmospheric science paper, Colorado State University, 121 pp.

- Greer, A. J., and Coauthors, 2018: All-sky satellite data assimilation at operational weather forecasting centers. *Quart. J. Roy. Meteor. Soc.*, **144**, 1191–1217, doi:10.1002/qj.3202.
- Grist, J. P., 2002: Easterly waves over Africa. Part I: The seasonal cycle and contrasts between wet and dry years. *Mon. Wea. Rev.*, **130**, 197–211, doi:10.1175/1520-0493(2002)130<0197:EWOAPI>2.0.CO;2.
- Gu, Y., K. N. Liou, S. C. Ou, and R. Fovell, 2011: Cirrus cloud simulations using WRF with improved radiation parameterization and increased vertical resolution. *J. Geophys. Res. Atmos.*, **116**, D06 119, doi:10.1029/2010JD014574.
- Hair, J. W., and Coauthors, 2008: Airborne high spectral resolution lidar for profiling aerosol optical properties. *Appl. Opt.*, **47** (36), 6734–6752, doi:10.1364/AO.47.006734.
- Havemann, S., 2020: NWPSAF 1D-Var top-level design version 1.2 NWPSAF-MO-DS-026. Top level design, Met-Office, 10 pp. <https://www.nwpsaf.eu/site/software/1d-var/documentation>.
- Haywood, J. M., B. T. Johnson, S. R. Osborne, J. Mulcahy, M. E. Brooks, M. A. J. Harrison, S. F. Milton, and H. E. Brindley, 2011a: Observations and modelling of the solar and terrestrial radiative effects of Saharan dust: a radiative closure case-study over oceans during the GERBILS campaign. *Quart. J. Roy. Meteorol. Soc.*, **137**, 1211–1226, doi:10.1002/qj.770.
- Haywood, J. M., and Coauthors, 2011b: Motivation, rationale and key results from the GERBILS Saharan dust measurement campaign. *Quart. J. Roy. Meteorol. Soc.*, **137**, 1106–1116, doi:10.1002/qj.797.

- Hess, M., P. Koepke, and I. Schult, 1998: Optical properties of aerosols and clouds: The software package OPAC. *Bull. Amer. Meteor. Soc.*, **79**, 831–844, doi:10.1175/1520-0477(1998)079<0831:OPOAAC>2.0.CO;2.
- Heymsfield, A., D. Winker, M. Avery, M. Vaughan, G. Diskin, M. Deng, V. Mitev, and R. Matthey, 2014: Relationships between ice water content and volume extinction coefficient from in situ observations for temperatures from 0° to -86°C: Implications for spaceborne lidar retrievals. *J. Appl. Meteor. Climatol.*, **53**, 479–505, doi:10.1175/JAMC-D-13-087.1.
- Hocking, J., P. J. Rayner, D. Rundle, R. W. Saunders, M. Matricardi, A. Geer, P. Brunel, and J. Vidot, 2013: Rttov v11 users guide. Nwp-saf report, Met. Office, 114 pp.
- Holben, B. N., and Coauthors, 1998: AERONET - A federated instrument network and data archive for aerosol characterization. *Rem. Sens. Environ.*, **66**, 1–16, doi:10.1016/S0034-4257(98)00031-5.
- Holz, R. E., and Coauthors, 2016: Resolving ice cloud optical thickness biases between CALIOP and MODIS using infrared retrievals. *Atmos. Chem. Phys.*, **16**, 5075–5090, doi:10.5194/acp-16.5075-2016.
- Honda, T., and Coauthors, 2018: Assimilating all-sky Himawari-8 satellite infrared radiances: A case of Typhoon Soudelor (2015). *Mon. Wea. Rev.*, **146**, 213–229, doi:10.1175/MWR-D-16-0357.1.
- Jacob, D. J., 1999: *Introduction to Atmospheric Chemistry*. Princeton University Press, 266 pp.

- Jin, Z., T. P. Charlock, and K. Rutledge, 2002: Analysis of broadband solar radiation and albedo over the ocean surface at COVE. *J. Atmos. Oceanic Tech.*, **19**, 1585–1601, doi:10.1175/1520-0426(2002)019<1585:AOBSRA>2.0.CO;2.
- Kaufman, Y. J., A. Smirnov, B. N. Holben, and O. Dubovik, 2001: Baseline maritime aerosol: Methodology to derive the optical thickness and scattering properties. *Geophys. Res. Lett.*, **28**, 3251–3254, doi:10.1029/2001GL013312.
- Koepke, P., J. Gasteiger, and M. Hess, 2015: Technical note: Optical properties of desert aerosol with non-spherical mineral particles: data incorporated to OPAC. *Atmos. Chem. Phys.*, **15**, 5947–5956, doi:10.5194/acp-15-5947-2015.
- Koepke, P., and M. Hess, 1988: Scattering functions of tropospheric aerosols: the effects of nonspherical particles. *Appl. Optics*, **27**, 22 422–2430, doi:10.1364/AO.27.002422.
- Koffi, B., and Coauthors, 2016: Evaluation of the aerosol vertical distribution in global aerosol models through comparison against CALIOP measurements: AeroCom phase II results. *J. Geophys. Res. Atmos.*, **121**, 7254–7283, doi:10.1002/2015JD024639.
- Kunze, S., 2021: Unraveling the effects of tropical cyclones on economic sectors worldwide: Direct and indirect impacts. *Environ. Resource Econ.*, **78**, 545–569, doi:10.1007/s10640-021-00541-5.
- Levenberg, K., 1944: A method for the solution of certain non-linear problems in least squares. *Quart. Appl. Math.*, **2**, 164–168, doi:10.1090/qam/10666.
- Lewis, J. M., 2005: Roots of ensemble forecasting. *Mon. Wea. Rev.*, **133**, 1865–1885, doi:10.1175/MWR2949.1.

- Liou, K. N., 2002: *An Introduction to Atmospheric Radiation, Second Edition*. Elsevier, 583 pp.
- Lolli, S., and Coauthors, 2017: Daytime top-of-the-atmosphere cirrus cloud radiative forcing properties at Singapore. *J. Appl. Meteorol. Climatol.*, **56**, 1249–1257, doi:10.1175/JAMC-D-16-0262.1.
- Lorenz, E. N., 1982: Atmospheric predictability experiments with a large numerical model. *Tellus*, **34**, 505–513, doi:10.3402/tellusa.v34i6.10836.
- Lynch, P., and Coauthors, 2016: An 11-year global gridded aerosol optical thickness reanalysis (v1.0) for atmospheric and climate sciences. *Geosci. Model Dev.*, **9**, 1489–1522, doi:10.5194/gmd-9-1489-2016.
- Mace, G. G., Q. Zhang, M. Vaughan, R. Marchand, G. Stephens, C. Trepte, and D. Winker, 2009: A description of hydrometeor layer occurrence statistics derived from the first year of merged Cloudsat and CALIPSO data. *J. Geophys. Res. - Atmos.*, **114**, D00A26, doi:10.1029/2007JD009755.
- Marquis, J. W., A. S. Bogdanoff, J. R. Campbell, J. A. Cummings, D. L. Westphal, N. J. Smith, and J. Zhang, 2017: Estimating infrared radiometric satellite sea surface temperature retrieval cold biases in the tropics due to unscreened optically thin cirrus clouds. *J. Atmos. Oceanic Technol.*, **34**, 355–373, doi:10.1175/JTECH-D-15-0226.1.
- Marquis, J. W., and Coauthors, 2021: Conceptualizing the impact of dust-contaminated infrared radiances on data assimilation for numerical weather prediction. *J. Atmos. Oceanic Technol.*, **38**, 209–221, doi:10.1175/JTECH-D-19-0125.1.
- McClatchey, R. A., R. W. Fenn, J. A. Selby, F. E. Volz, and J. S. Garing, 1972: Optical properties of the atmosphere. Environmen-

- tal research paper, Defense Technical Information Center, 108 pp.
<https://apps.dtic.mil/dtic/tr/fulltext/u2/753075.pdf>.
- McGill, M., D. Hlavka, W. Hart, V. S. Scott, J. Spinhirne, and B. Schmid, 2002: Cloud physics lidar: instrument description and initial measurement results. *Appl. Opt.*, **41** (18), 3725–3734, doi:10.1364/AO.41.003725.
- McNally, A. P., 2009: The direct assimilation of cloud-affected satellite infrared radiances in the ECMWF 4D-Var. *Quart. J. Roy. Meteor. Soc.*, **135**, 1214–1229, doi:10.1002/qj.426.
- Measures, R. M., 1984: *Laser Remote Sensing. Fundamentals and Applications*. John Wiley & Sons, 510 pp.
- Menzel, W. P., T. J. Schmit, P. Zhang, and J. Li, 2018: Satellite-based atmospheric infrared sounder development and applications. *Bull. Amer. Meteor. Soc.*, **99**, 583–603, doi:10.1175/BAMS-D-16-0293.1.
- Miloshevich, L. M., H. Vömel, A. Paukkunen, A. J. Heymsfield, and S. J. Oltmans, 2001: Characterization and correction of relative humidity measurements from Vaisala RS80-A radiosondes at cold temperatures. *J. Atmos. Oceanic Technol.*, **18**, 135–156, doi:10.1175/1520-0426(2001)018<0135:CACORH>2.0.CO;2.
- Molod, A., L. Takacs, M. Suarez, and J. Bacmeister, 2015: Development of the GEOS-5 atmospheric general circulation model: evolution from MERRA to MERRA2. *Geosci. Model Dev.*, **8**, 1339–1356, doi:10.5194/gmd-8-1339-2015.
- Müller, D., A. Ansmann, I. Mattis, M. Tesche, U. Wandinger, D. Althausen, and G. Pisani, 2007: Aerosol-type-dependent lidar ratios observed with Raman lidar. *J. Geophys. Res.*, **112**, D16 202, doi:10.1029/2006JD008292.

- Okamoto, K., 2013: Assimilation of overcast cloudy infrared radiances of the geostationary MTSAT-1R imager. *Quart. J. Roy. Meteor. Soc.*, **139**, 715–730, doi:10.1002/qj.1994.
- Oyola, M. I., and Coauthors, 2019: Quantifying the direct radiative effect of absorbing aerosols for numerical weather prediction: a case study. *Atmos. Chem. Phys.*, **19**, 205–218, doi:10.5194/acp-19-205-2019.
- Panofsky, R. A., 1949: Objective weather-map analysis. *J. Atmos. Sci.*, **6**, 386–392, doi:10.1175/1520-0469(1949)006<0386:OWMA>2.0.CO;2.
- Patterson, E. M., D. A. Gillette, and B. H. Stockton, 1977: Complex index of refraction between 300 and 700 nm for Saharan aerosols. *J. Geophys. Res.*, **82**, 3153–3160, doi:10.1029/JC082i021p03153.
- Pierangelo, C., A. Chédin, S. Heilliette, N. Jacquinet-Husson, and R. Armante, 2004: Dust altitude and infrared optical depth from AIRS. *Atmos. Chem. Phys.*, **4**, 1813–1822, doi:10.5194/acp-4-1813-2004.
- Platnick, S., and Coauthors, 2017: The MODIS cloud optical and microphysical products: Collection 6 updates and examples from Terra and Aqua. *IEEE Trans. Geosci. Remote Sens.*, **55**, 502–525, doi:10.1109/TGRS.2016.2610522.
- Quijano, A. L., I. N. Sokolik, and O. B. Toon, 2000: Radiative heating rates and direct radiative forcing by mineral dust in cloudy atmospheric conditions. *J. Geophys. Res. Atmos.*, **105**, 12 207–12 219, doi:10.1029/2000JD900047.
- Reid, J. S., and P. V. Hobbs, 1998: Physical and optical properties of young smoke from individual biomass fires in Brazil. *J. Geophys. Res. Atmos.*, **103**, 32 013–32 030, doi:10.1029/98JD00159.

- Rogers, R. R., and Coauthors, 2009: NASA LaRC airborne high spectral resolution lidar aerosol measurements during MILAGRO: observations and validation. *Atmos. Chem. Phys.*, **9**, 4811–4826, doi:10.5194/acp-9-4811-2009.
- Ruescas, A. B., M. Arbelo, J. A. Sobrino, and C. Mattar, 2011: Examining the effects of dust aerosols on satellite sea surface temperatures in the Mediterranean sea using the medspiration match database. *J. Atmos. Oceanic Technol.*, **28**, 684–697, doi:10.1175/2010JTECHA1450.1.
- Sassen, K., and B. S. Cho, 1992: Subvisual-thin cirrus lidar dataset for satellite verification and climatological research. *J. Appl. Meteorol.*, **31**, 1275–1285, doi:10.1175/1520-0450(1992)031<1275:STCLDF>2.0.CO;2.
- Saunders, R., and Coauthors, 2013: Rttov-11: Science and validation report. Nwp-saf report, Met. Office, 62 pp.
- Scott, N. A., and A. Chedin, 1981: A fast line-by-line method for atmospheric absorption computations: The Automated Atmospheric Absorption Atlas. *J. Appl. Meteor.*, **20**, 802–812, doi:10.1175/1520-0450(1981)020<0802:AFLBLM>2.0.CO;2.
- Siméoni, D., C. Singer, and G. Chalon, 1997: Infrared Atmospheric Sounding Interferometer. *Acta Astron.*, **40**, 113–118, doi:10.1016/S0094-5765(97)00098-2.
- Smirnov, A., and Coauthors, 2011: Maritime aerosol network as a component of AERONET - first results and comparison with global aerosol models and satellite retrievals. *Atmos. Meas. Tech.*, **4**, 583–597, doi:10.5194/amt-4-583-2011.
- Smith, F., 2017: Nwpsaf 1d-var product specification. Nwp-saf report, Met. Office, 24 pp.

- Song, Q., Z. Zhang, H. Yu, S. Kato, P. Yang, P. Colarco, L. A. Remer, and C. L. Ryder, 2018: Net radiative effects of dust in the tropical North Atlantic based on integrated satellite observations and in situ measurements. *Atmos. Chem. Phys.*, **18**, 11 303–11 322, doi:10.5194/acp-18-11303-2018.
- Stuhlmann, R., A. Rodriguez, S. Tjemkes, D. M. Aminou, H. Stark, and W. Schumann, 2009: MTG-IRS: Status, specifications and technical concept. *Advances in Imaging*, Optical Society of America, FMC1, doi:10.1364/FTS.2009/FMC1.
- Taylor, J. P., J. M. Edwards, M. D. Glew, P. Hignett, and A. Slingo, 1996: Studies with a flexible new radiation code. II: Comparisons with aircraft short-wave observations. *Quart. J. Roy. Meteorol. Soc.*, **112**, 839–861, doi:10.1002/qj.49712253204.
- Tegen, I., P. Hollrig, M. Chin, I. Fung, D. Jacob, and J. Penner, 1997: Contribution of different aerosol species to the global aerosol extinction optical thickness: Estimates from model results. *J. Geophys. Res. Atmos.*, **102**, 23 895–23 915, doi:10.1029/97JD01864.
- Tegen, I., and A. A. Lacis, 1996: Modeling of particle size distribution and its influence on the radiative properties of mineral dust aerosol. *J. Geophys. Res.*, **101**, 19 237–19 244, doi:10.1029/95JD03610.
- Theil, H., 1950a: A rank-invariant method of linear and polynomial regression analysis: I. *Ned. Akad. Wet. Proc.*, **53**, 386–392.
- Theil, H., 1950b: A rank-invariant method of linear and polynomial regression analysis: I. *Ned. Akad. Wet. Proc.*, **53**, 1397–1412.
- Theil, H., 1950c: A rank-invariant method of linear and polynomial regression analysis: II. *Ned. Akad. Wet. Proc.*, **53**, 521–525.

- Tobin, D. C., H. E. Revercomb, J. K. Taylor, R. O. Knuteson, D. H. DeSlover, and L. A. Borg, 2013: Cross-Track Infrared Sounder (CrIS) spectral radiance calibration and evaluations. *AIP Conf. Proc.*, **1531**, 724–727, doi:10.1063/1.4804872.
- Tompkins, A. M., C. Cardinali, J. J. Morecette, and M. Rodwell, 2005: Influence of aerosol climatology on forecasts of the African Easterly Jet. *Geophys. Res. Lett.*, **32**, L10 801, doi:10.1029/2004GL022189.
- Toon, O. B., and Coauthors, 2016: Planning, implementation, and scientific goals of the Studies of Emissions and Atmospheric Composition, Clouds and Climate Coupling by Regional Surveys (SEAC⁴RS) field mission. *J. Geophys. Res. Atmos.*, **121**, 4967–5009, doi:10.1002/2015JD024297.
- Toth, T. D., and Coauthors, 2013: Investigating enhanced Aqua MODIS aerosol optical depth retrievals over mid-to-high latitude Southern Oceans through inter-comparison with co-located CALIOP, MAN, and AERONET data sets. *J. Geophys. Res. Atmos.*, **118**, 4700–4714, doi:10.1002/jgrd.50311.
- Tzvi, G.-C., B. D. Schmidt, and L. W. Uccellini, 1986: Simulation experiments for testing the assimilation of geostationary satellite temperature retrievals into a numerical weather prediction model. *Mon. Wea. Rev.*, **114**, 1213–1230, doi:10.1175/1520-0493(1986)114<1213:SEFTTA>2.0.CO;2.
- Viana, M., X. Querol, A. Alastuey, E. Cuevas, and S. Rodríguez, 2002: Influence of African dust on the levels of atmospheric particulates in the Canary Islands air quality network. *Atmos. Env.*, **36**, 5861–5875, doi:10.1016/S1352-2310(02)00463-6.
- Vidot, J., A. J. Baran, and P. Brunel, 2015: A new ice cloud parameterization for infrared radiative transfer simulation of cloudy radiances: Evaluation and optimiza-

- tion with IIR observations and ice cloud profile retrieval products. *J. Geophys. Res. Atmos.*, **120**, 6937–6951, doi:10.1002/2015JD023462.
- Virts, K. S., J. M. Wallace, Q. Fu, and T. P. Ackerman, 2010: Tropical tropopause transition layer cirrus as represented by CALIPSO lidar observations. *J. Atmos. Sci.*, **67**, 3113–3129, doi:10.1175/2010JAS3412.1.
- Volz, F. E., 1973: Infrared optical constants of ammonium sulfate, sahara dust, volcanic pumice, and flyash. *Appl. Opt.*, **12**, 564–568, doi:10.1364/AO.12.000564.
- Voss, K. K., and A. T. Evan, 2020: A new satellite-based global climatology of dust aerosol optical depth. *J. Appl. Meteor. Climatol.*, **59**, 83–102, doi:10.1175/JAMC-D-19-0194.1.
- Wagner, F., and Coauthors, 2009: Properties of dust aerosol particles transported to Portugal from the Sahara desert. *Tellus B: Chem. Physical Meteorol.*, **61**, 297–306, doi:10.1111/j.16-0889.2008.00393.x.
- Wallace, J. M., and P. V. Hobbs, 2006: *Atmospheric Science: An Introductory Survey, Second Edition*. Elsevier, 583 pp.
- Wang, C., Z. Zeng, and M. Ying, 2020: Uncertainty in tropical cyclone intensity predictions due to uncertainty in initial conditions. *Adv. Atmos. Sci.*, **37**, 278–290, doi:10.1007/s00376-019-9126-6.
- Wehrli, C., July 1985: Extraterrestrial solar spectrum, publication no. 615. Phys. meteor. observ., World Radiation Center.
- Welton, E. J., J. R. Campbell, J. D. Spinhirne, and V. S. Scott, 2001: Global monitoring of clouds and aerosols using a network of micropulse lidar systems. *Proc. SPIE*, **4153**, 151–159, doi:10.1117/12.417040.

- Weston, P. P., W. Bell, and J. R. Eyre, 2014: Accounting for correlated error in the assimilation of high resolution sounders. *Quart. J. Roy. Meteor. Soc.*, **140**, 2420–2429, doi:10.1002/qj.2306.
- Winker, D. M., and Coauthors, 2010: The CALIPSO mission: A global 3D view of aerosols and clouds. *Bull. Amer. Meteor. Soc.*, **91**, 1211–1230, doi:10.1175/2010BAMS3009.1.
- Wiscombe, W. J., 1977: The Delta- M method: Rapid yet accurate radiative flux calculations for strongly asymmetric phase functions. *J. Atmos. Sci.*, **34**, 1408–1422, doi:10.1175/1520-0469(1977)034<1408:TDMRYA>2.0.CO;2.
- WMO, 2019: *Vision for the WMO Integrated Global Observing System in 2040*. World Meteorological Organization, 47 pp.
- Yang, J., Z. Zhang, C. Wei, F. Lu, and Q. Guo, 2017: Introducing the new generation of Chinese geostationary weather satellites, Fengyun-4. *Bull. Amer. Meteor. Soc.*, **98**, 1637–1658, doi:10.1175/BAMS-D-16-0065.1.
- Yang, P., L. Bi, B. A. Baum, K. Liou, G. W. Kattawar, M. I. Mishchenko, and B. Cole, 2013: Spectrally consistent scattering, absorption and polarization properties of atmospheric ice crystals at wavelengths from 0.2 to 100 μm . *J. Atmos. Sci.*, **70**, 330–347, doi:10.1175/JAS-D-12-039.1.
- Yorks, J. E., S. P. Palm, M. J. McGill, D. L. Hlavka, W. D. Hart, P. A. Selmer, and E. Nowottnick, 2016: CATS algorithm theoretical basis document: Level 1 and level 2 data products. Algorithm theoretical basis document, Science Systems and Applications, Inc., 60 pp.
- Zhang, J., J. S. Reid, M. Christensen, and A. Benedetti, 2016: An evaluation of the impact of aerosol particles on weather forecasts from a biomass burning aerosol

- event over the Midwestern United States: observational-based analysis of surface temperature. *Atmos. Chem. Phys.*, **16**, 6475–6494, doi:10.5194/acp-16-6475-2016.
- Zhang, J., J. S. Reid, D. L. Westphal, N. L. Baker, and E. J. Hyer, 2008: A system for operational aerosol optical depth data assimilation over global oceans. *J. Geophys. Res. Atmos.*, **113**, D10 208, doi:10.1029/2007JD009065.
- Zhao, Q., F. Zhang, T. Holt, C. H. Bishop, and Q. Xu, 2013: Development of a mesoscale ensemble data assimilation system at the naval research laboratory. *Weather and Forecasting*, **28**, 1322–1336, doi:10.1175/WAF-D-13-00015.1.